University of Alberta

Investigation of Positive Feedback Anti-Islanding Scheme for Inverter-Based Distributed Generation

by

Xiaoyu Wang 

A thesis submitted to the Faculty of Graduate Studies and Research in partial fulfillment of the requirements for the degree of **Doctor of Philosophy**

in

Power Engineering and Power Electronics

Department of Electrical and Computer Engineering

Edmonton, Alberta
Fall 2008

Your file Votre référence
ISBN: 978-0-494-46449-6
Our file Notre référence
ISBN: 978-0-494-46449-6

Abstract

Distributed generation has been greatly introduced into electrical power systems during the last several decades. Providing protection against islanding is probably one of the most challenging issues addressed in distributed generation applications. The positive feedback anti-islanding scheme for inverter-based distributed generators has gained wide acceptance. This scheme has a destabilizing effect on the supply system. Although a single inverter's destabilizing force is small, the collective impact of the destabilizing force produced by a large number of distributed generators may be significant. This impact may make the anti-islanding scheme less effective or may cause problems to the supply power system.

The objective of this thesis is to determine the impact of inverter-based distributed generators on power systems and the interactions among the distributed generators due to the positive feedback anti-islanding control. Four related topics are covered in the thesis. First, small-signal models representing the interconnected inverter-based distributed generation systems and the associated anti-islanding actions are established. These models provide the analytical tools for the work conducted in the other topics. The models' validity is evaluated by using electromagnetic transient simulation programs. Second, the nature and characteristics of a single inverter's impact on power systems are investigated. The relationship between the positive feedback anti-islanding control strength and the single distributed generator power transfer capability is quantified. Third, the nature and characteristics of the collective impact of multiple inverters and their anti-islanding activities on power systems are studied. The small-signal stability of the distributed generation system with multiple inverters and the interferences among the generators are analyzed. Last, the islanding

protection performance of the positive feedback anti-islanding scheme is evaluated in terms of the stability.

Acknowledgements

This dissertation could not have been written without Dr. Wilsun Xu and Dr. Venkata Dinavahi who not only served as my supervisors but also encouraged and challenged me throughout my academic program. I would like to express my sincere appreciation to them for their invaluable guidance. In addition, financial support for this dissertation was provided in part by Natural Resources Canada through the Technology and Innovation Program as part of the Climate Action Plan for Canada.

I would also like to thank Dr. Walmir Freitas for his continuous help and collaboration. His support helped me to get through the hardest time during the pursuit of my Ph.D. degree.

I take this opportunity to extend my appreciation to my committee members, Dr. Geza Joos, Dr. John Salmon, Dr. Amos Ben-Zvi, Dr. Yunwei Li and Dr. James Miller, for their time and effort. Their valuable comments and instructive suggestions helped me to improve the quality of this dissertation.

Special thanks are due to my colleagues working with the power lab at University of Alberta. Their friendship and assistance made my stay in this lab an enjoyable experience.

Finally, I would like to express my gratitude to my parents and sister for their love, patience and care. And I am deeply grateful to my girlfriend, Lei Lei, for her endless understanding and support.

Contents

List of Tables

List of Figures

List of Acronyms

AFD	Active Frequency Drift
CB	Circuit Breaker
CSI	Current Source Inverter
DAE	Differential Algebraic Equation
DG	Distributed Generation
DGs	Distributed Generators
DRs	Distributed Resources
EMTP	Electromagnetic Transients Program
GE	General Electric
GP	Grid Parallel
IGBT	Insulated Gate Bipolar Transistor
NDZ	Non-Detection Zone
OFR	Over Frequency Relay
OVR	Over Voltage Relay
PCC	Point of Common Coupling
PI	Proportional-Integral
PLL	Phase-Locked Loop
PV	Photovoltaic
PWM	Pulse Width Modulation
SA	Standalone
SFS	Sandia Frequency Shift
SMS	Slip-Mode Frequency Shift
SNL	Sandia National Laboratories
SVS	Sandia Voltage Shift

THD	Total Harmonic Distortion
UFR	Under Frequency Relay
UVR	Under Voltage Relay
VSI	Voltage Source Inverter
ZCD	Zero Crossing Detection

List of Symbols

$\mathbf{A}$	State Matrix of Descriptor System Small-Signal Models
A_k, B_k	Fourier Coefficients of Inverter Output Current Distorted by SFS
$\mathbf{B}$	Input Matrix of Descriptor System Small-Signal Models
$\mathbf{C}_0, \mathbf{S}_0$	Diagonal Matrices of dq-to-xy Transformation
C_L	*RLC* Load Capacitance
C_{norm}	Normalized Capacitance
C_{res}	Resonance Capacitance
$\mathbf{E}$	Singular Matrix of Single-DG Descriptor System Small-Signal Model
H	Motor Rotor Inertia Constant
$\mathbf{H}$	Singular Matrix of Multi-DG Descriptor System Small-Signal Model
I_{base}	Current Base Value in *Per Unit* System
I_{ref}	Magnitude of Current Reference of Inverter Current Regulator
K_f	Frequency Positive Feedback Gain
K_p	Voltage Positive Feedback Gain
K_v	Voltage Positive Feedback Gain
L	Distribution Line Inductance
L_L	*RLC* Load Inductance
L_s	Inverter Series Filter Inductance
P_{DG}	DG Output Active Power
P_L	Load Active Power
P_N	Network Active Power
P, Q	Inverter Output Power
P_{ref}, Q_{ref}	Inverter Power Regulator Power References
P^*_{ref}	Inverter Distorted Power Reference

Q_{DG}	DG Output Reactive Power
Q_f	*RLC* Load Quality Factor
Q_L	Load Reactive Power
Q_N	Network Reactive Power
R	Distribution Line Resistance
R_L	*RLC* Load Resistance
R_r	Motor Rotor Resistance
R_s	Motor Stator Resistance
S_{base}	Power Base Value in *Per Unit* System
T_e	Motor Electromagnetic Torque
$T_{i_{DG}}$	DG Output Current Period
T_l	Time Constant of Low Pass Filter
T_m	Motor Mechanical Torque
$T_{v_{DG}}$	DG Terminal Voltage Period
T_w	Time Constant of Washout Filter
V	Magnitude of Inverter Terminal Voltage
V_0	Rated Grid Voltage
V_{base}	Voltage Base Value in *Per Unit* System
X	Distribution Line Reactance
X_m	Motor Magnetizing Reactance
X_r	Motor Rotor Leakage Reactance
X_s	Motor Stator Leakage Reactance
Z	Distribution Line Impedance
Z_{base}	Impedance Base Value in *Per Unit* System
Z_L	Equivalent Impedance of *RLC* Load
cf	Frequency Positive Feedback Chopping Fraction
cf_0	Initial Chopping Fraction
e_a, e_b, e_c	Supply Power System Voltages
e_d, e_q	Supply Power System Voltages on dq-axis
f_0	Rated Grid Frequency (60Hz)
$f_{i_{DG}}$	DG Output Current Frequency

f_r	RLC Load Resonance Frequency
f_s	Island Steady-State Frequency
$f_{v_{DG}}$	DG Terminal Voltage Frequency
i_a, i_b, i_c	Three-Phase Inverter Output Currents
i_C	C_L Branch Current of RLC Load
i_d, i_q	Inverter Output Currents on dq-axis
i_{DG}	DG Output Current
i_{dref}, i_{qref}	Inverter Current Regulator Current References
i^*_{dref}, i^*_{qref}	Inverter Distorted Current References
i_L	L_L Branch Current of RLC Load
i_N	Network Current
i_R	R_L Branch Current of RLC Load
i_{rx}, i_{ry}	Motor Rotor Currents on xy-axis
i_{sx}, i_{sy}	Motor Stator Currents on xy-axis
i_α, i_β	Inverter Output Currents on $\alpha\beta$-axis
k_{ii}	Integration Gain of Inverter Current Regulator
k_{ip}	Integration Gain of Inverter Power Regulator
k_{iPLL}	Integration Gain of PLL Controller
k_{pi}	Proportional Gain of Inverter Current Regulator
k_{pp}	Proportional Gain of Inverter Power Regulator
k_{pPLL}	Proportional Gain of PLL Controller
p	Derivative Operator
s	Laplace Operator
t_z	Dead Time in SFS
u_d, u_q	Inverter Current Regulator Output Voltages
v_a, v_b, v_c	Three-Phase Inverter Terminal Voltages
v_d, v_q	Inverter Terminal Voltages on dq-axis
v_{DG}	DG Terminal Voltage
v_{sa}, v_{sb}, v_{sc}	Ideal Voltage Sources in Average Inverter Model
v_{sd}, v_{sq}	Ideal Inverter Voltage Sources on dq-axis
v_x, v_y	Motor Stator Voltages on xy-axis

v_α, v_β	Inverter Terminal Voltages on $\alpha\beta$-axis
Δ	Small-Signal Variables
$\Delta\mathbf{x}$	Small-Signal Variable Vector
ΔP	Active Power Imbalance
ΔQ	Reactive Power Imbalance
δ_0	Initial Phase Angle of Inverter Terminal Voltage
θ	Phase Angle of Inverter Terminal Voltage
θ_1, θ_f	Equivalent Phase Shift Angle Introduced by SFS
θ_{load}	Phase Angle of Parallel RLC Load
θ_{PLL}	Inverter Terminal Voltage Phase Angle Acquired by PLL
λ	System Eigenvalue
ϕ_s	Phase Angle Difference between v_{DG} and i_{DG}
ψ_{rx}, ψ_{ry}	Motor Rotor Fluxes on xy-axis
ψ_{sx}, ψ_{sy}	Motor Stator Fluxes on xy-axis
ω	Radian Frequency of Inverter Terminal Voltage
ω_0	Radian Frequency of Grid
ω_{ff}	PLL Feedforward Frequency
ω_{PLL}	Inverter Terminal Voltage Frequency Acquired by PLL
ω_r	Motor Rotor Speed
ω_s	Radian Frequency of Islanded DG System

Chapter 1

Introduction

Modern power distribution systems are designed and operated on the basis of two assumptions. One is that the system is a passive network with only one source at the substation. Another assumes that there is only one direction of power flow, from the substation to the loads, in the system. Over the years, voltage control strategies, protection schemes and reliability measures have been implemented in distribution systems based on such considerations. When a distributed generator is connected to such a system, the basic assumptions are no longer true. Power could flow to "downstream" as well as "upstream". The network becomes active and is charged by many sources. Therefore, the traditional operating principle of modern power distribution systems is altered by the incorporation of distributed generation (DG) units and consequently potential impact caused by DG could be made on the power distribution systems. This thesis investigates one of the challenging problems associated with the integration of DG into electric networks. In this chapter, some insight into grid interconnection of DG units and DG islanding formation is provided. The objectives of the thesis are discussed, and the thesis outline is given at the end of the chapter.

1.1 Grid Interconnection of DG Units

DG refers to the scheme of generating power by a large number of small generators (1kW to 20MW) connected at the power distribution system (120V to 44kV). Most distributed generators (DGs) use renewable resources such as wind, solar and small

hydro for power generation. DG is an effective solution to help defer the transmission and distribution infrastructure upgrades, reduce the distribution system losses and mitigate the greenhouse gas emissions.

As a radically different way to deliver electricity, DG is expected to result in fundamental changes to the current power system structure. Various studies have shown that DG can affect the operation and planning of distribution networks in a number of ways [1] - [3]:

- Installation of a large number of DGs in distribution systems will change the network voltage profile which usually decreases monotonously from substation to the end of feeders. The reverse power flow during periods of light load and maximum daylight may cause a significant voltage rise in the distribution lines, particularly at the ends. Conventional planning and operating methods may not work properly for this situation.

- The impact on power quality is a major issue related to interconnection of DG into the power systems. Transient voltage variations can be caused to distribution networks if there are relatively large current changes during connection and disconnection of DGs. The use of advanced power converters at the front end of many types of DG can increase system harmonic distortion level. Flicker, DC injection, voltage unbalance, electromagnetic compatibility and other power quality problems could also be introduced by DG.

- The aggregate contribution of many small DG units, or a few large DG units, can alter the short circuit levels enough to affect the fault detection in distribution systems and cause delay in operation of the protective devices. When multiple DGs are implemented in distribution systems, the short-circuit capacity of the distribution system may be increased and the fault current during a short-circuit may become more substantial. If the value of short-circuit current exceeds the rupturing capacity of the over-current circuit breakers installed at the local load end, they may become incapable of clearing faults at the customer premises.

- DGs are characterized by low inertias, high reactances, short time constants and poor inherent damping. These factors as well as the restricted reactive power output, close proximity of other generators and network loads are the reasons for the growing concern over the transient stability of distribution systems.

In response to the trend of DG applications, many utility companies in North America have established or are in the process of establishing guidelines governing the interconnection of DGs to the utility grid. The IEEE and other standard bodies are also making significant efforts on interconnection standards [3] - [9]. This is a positive step towards the acceptance of DG by the utility industry. However, the basic philosophy of these guidelines and standards is to request the DGs to adapt to the existing distribution system infrastructure and practice. Some of the requirements have rendered many DG opportunities economically unattractive.

1.2 Electric Island Formed by DG

An island is a condition in which a portion of the power system is energized solely by DGs through the associated points of common coupling (PCCs) while that portion of the system is electrically separated from the rest of the power system [4]. This condition is illustrated by Figure 1.1 where several DGs are connected to a distribution feeder of a typical distribution power system. When the feeder is disconnected from the main system by the breaker, for example, the small DGs will feed the downstream part of the disconnected feeder continuously, and, as a result, an island is formed. An island formed inadvertently is known as an unintentional island, whereas an intentional island is formed for reliability purposes. Unintentional islanding may cause a number of problems for DGs and the connected loads. Unintentional islanding in distributed energy generation should be prevented for the following reasons [10], [11]:

- Voltage and frequency in the island cannot be controlled by the utilities. Custom equipment could be damaged because of voltage or frequency excursions outside of the acceptable ranges.

- Unintentional islanding may create a hazard for power linemen or the public by

causing a line assumed to be disconnected from all energy sources to actually remain energized.

- Reclosing may cause a high transient current when the island is reconnected to the main system. This current will re-trip the line or damage the equipment within the island.
- Islanding may interfere with the manual or automatic restoration of normal service by the utilities.

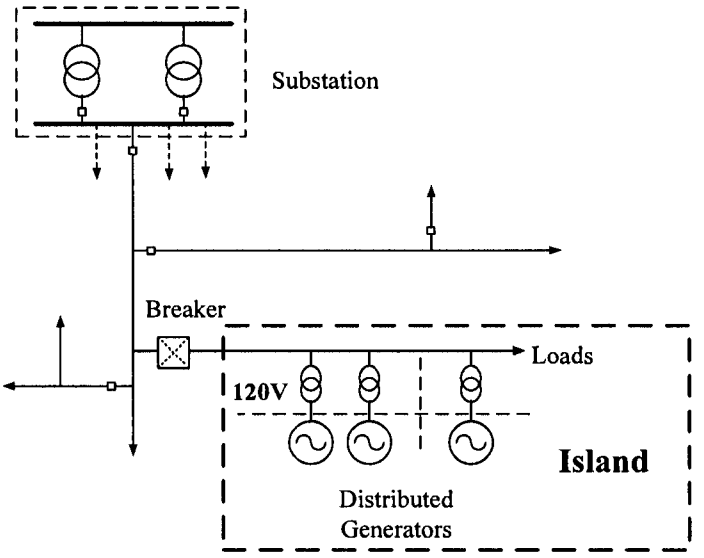

Figure 1.1: A typical distribution power system with DGs

For the above reasons, DGs are required to have anti-islanding capability, which refers to the capability of a distributed generator to detect if it is operating in an islanded system and to disconnect itself from the system in a timely fashion. The current industry practice is to trip all DGs immediately after the occurrence of islands. Doing so prevents equipment damage and eliminates safety hazards. This practice calls for the reliable and fast detection of islanding conditions. A successful anti-islanding scheme should work for any possible formations of islands and detect islanding conditions within the required time frame.

In order to satisfy the DG anti-islanding protection requirement, many anti-islanding techniques have been proposed, and a number of them have been implemented in actual DG projects [11]. When selecting an anti-islanding scheme, the characteristics of the DGs should be considered. Almost all DGs can be classified into two categories: rotational machine-based generators and inverter-based generators. The rotational machine-based DGs are usually connected to the primary feeder because of their relatively large sizes. The inverter-based generators are commonly connected to the secondary distribution system due to their relatively small sizes. Actually, the inverter is an interface between the system and the generator. The generator can be photovoltaic (PV) panels, fuel cells, micro-turbines, etc. Since the inverter interacts with the supply system, all inverter-based DGs have some common operating characteristics. This thesis will focus on these common characteristics and provide results of general applicability to all inverter-based DGs.

1.3 Objective and Scope

Over the past one or two decades, research on DG has been focused on the improvement of individual DG technologies and their interface with power systems. With the increased installation of DGs in power systems, it has become clear that there is a need to understand the collective impact of operating a large amount of DGs on power distribution systems. This work is of significance from two perspectives. First, it helps to understand the potential interactions among DGs so that timely technologies can be developed to address the problems. Second, the results will better prepare utility companies to embrace the widespread application of DG technologies.

One of the concerns associated with high penetration of DGs is the anti-islanding scheme resident in DGs. A majority of inverter-based DGs injects disturbances into the supply system to facilitate the detection of islanding conditions. While the injected disturbance is small from the perspective of a single inverter, the collective impact of the disturbances produced by a large amount of DGs could be significant. The impact may render the anti-islanding scheme less effective or may cause problems

to the supply power system. The objective of this thesis is to address this concern according to the following four topics:

- How to model inverter anti-islanding schemes so that their impact can be investigated for cases involving large amount of inverter DG installation?
- What are the nature and characteristics of interference among the DGs due to their resident anti-islanding activities?
- What are the nature and characteristics of the collective impact of the inverter anti-islanding activities on the power systems?
- How to verify the methodologies and conclusions established for the first three questions?

The scope of this thesis can be summarized as follows:

- To conduct a comprehensive literature survey in the area of inverter anti-islanding schemes. The survey covers the topics of (1) evaluating the widely accepted anti-islanding schemes and selecting one of them for detailed investigation by this thesis; (2) understanding the implementation, characteristics and modeling of the selected anti-islanding scheme; (3) reviewing the published work that addresses the nature and characteristics of the interference among the inverters due to the selected anti-islanding scheme, and the potential impact of the scheme on power systems.
- To establish adequate mathematical models to represent the inverter anti-islanding actions for large scale DG penetration studies. The validity of the developed models is evaluated using circuit level simulation programs such as PSCAD/EMTDC and Matlab/Simulink. The models form the foundation on which the DG impact is investigated and evaluated.
- To investigate the nature and characteristics of the impact produced by a single inverter and its resident anti-islanding scheme on power systems. The collective impact of multiple inverters and the associated anti-islanding scheme on power

systems and other inverters is also studied. The research determines the impact as affected by the numbers, locations and degree of penetration of the inverters.

- To assess the islanding detection performance of the selected anti-islanding scheme in multiple inverter applications. The interaction between the inverter interface controls and the anti-islanding scheme is discussed in terms of islanding detection.

1.4 Thesis Limitations

The limitations of this thesis are as follows:

- Only the constant power-controlled and constant current-controlled inverters are studied in this thesis. The DG units with the advanced inverter interface controls are not investigated. In addition, the interactions between the positive feedback anti-islanding control and the inverters' DC side controls (e.g., photovoltaic controller, fuel cell controller) are not considered.

- Strictly speaking, islanding is a large signal disturbance for DG systems. When the small-signal analysis method is used to judge the stability of the islanded DG system, an approximation is made based on the assumption that the power imbalance between the supply system and the DG system including the DG local load is small.

- The conclusions drawn in this thesis rely on the investigation of a representative frequency-based positive feedback anti-islanding method. The specific characteristics of other positive feedback anti-islanding methods are not studied in detail, and the various positive feedback anti-islanding methods are not compared.

- In the analysis of the multi-DG systems, the dynamic loads are not included in the distribution systems.

1.5 Thesis Outline

The research was conducted using analytical and simulation methods. The remainder of this thesis is organized as follows:

Because many anti-islanding schemes are available for inverter-based DGs, these schemes must be reviewed, and the most suitable one must be selected for study. In Chapter 2, a literature survey on inverter anti-islanding schemes is conducted, and the classification of the reviewed schemes is summarized. The positive feedback anti-islanding scheme is chosen for further research for the following two reasons. First, the scheme has received industry-wide acceptance. Second, the scheme has a potential negative impact on power systems and other inverter-based DGs. As the first step of the research, the principle of the positive feedback anti-islanding scheme and the published work related to it are reviewed and presented in this chapter.

Although the positive feedback anti-islanding scheme has been successfully applied to commercial inverters, theoretical analysis of the scheme's impact on power systems is still required. In order to address this concern, adequate analytical models for inverter-based DGs and the anti-islanding scheme are needed. The development of the small-signal models of both single DG and multi-DG systems with the positive feedback anti-islanding control is shown in Chapter 3. The accuracy of the analytical models is verified by using the electromagnetic transient simulations in Matlab/Simulink and PSCAD/EMTDC.

Once the analytical models of the DG systems are set up, the relationship between the positive feedback anti-islanding control and the DG system small-signal stability can be quantified by using the modal analysis approach. This method is used to investigate the impact of the positive feedback anti-islanding scheme on the stability of single DG systems. The analysis results are presented in Chapter 4. In this chapter, an index called the DG power transfer capability versus the positive feedback gain (P-K) curve is proposed to facilitate the parametric analysis of the key factors affecting

the DG system stability. This index is also used to compare the effects of different inverter interface controls on the performance of the positive feedback anti-islanding scheme, and to provide guidance for the conflict requirement between the DG stability and the DG anti-islanding performance.

In multi-DG systems, multiple inverters are installed in power distribution systems. The positive feedback anti-islanding controls of the inverters not only aggregately affect the stability of the distribution systems but also interact to limit the stability of the individual DG unit. An investigation of the impact and interaction is conducted in Chapter 5 by using the methodology used in Chapter 4. In addition, the transient characteristics of the positive feedback anti-islanding scheme are studied in multi-DG systems.

The traditional methods used to evaluate the anti-islanding protection performance of the positive feedback scheme are based on the steady-state assumption, but these methods do not consider the dynamic information for the forming of the island. In Chapter 6, the modal analysis method and electromagnetic transient simulations are utilized to analyze the non-detection zone (NDZ) and islanding-detection time of the positive feedback anti-islanding scheme. The results show that the islanded DG system loses its stability when the quality factor of the RLC load is below the critical value.

Chapter 7 summarizes the main contributions and conclusions of the thesis. Some possible directions for future research are pointed out.

Chapter 2

DG Anti-Islanding Protection

An island is formed when a part of the distribution system becomes electrically isolated from the remainder of the power system, yet continues to be energized by DGs. Failure to trip islanded generators could compromise personal safety and result in equipment damage. The ability to detect and trip the DGs connected to an electric island depends on the anti-islanding capability of the DGs. Therefore, a thorough understanding of DG anti-islanding protection in power systems is necessary. This chapter reviews the various anti-islanding schemes. The classification of the reviewed schemes is summarized, and the specifics of the positive feedback anti-islanding scheme are discussed.

2.1 Selection of Anti-Islanding Scheme

Anti-islanding requirements have been evolving globally for many years and still vary considerably from country to country [11]. Many anti-islanding schemes have been developed to satisfy these requirements discussed in Chapter 1. Based on an extensive literature survey, four types of anti-islanding methods have been identified as follows:

- Passive local detection methods,
- Active local detection methods,
- Utility level methods, and,

- Communication-based methods.

The theory of the operation of the passive methods is illustrated by Figure 2.1 where an inverter-based distributed generator is connected to the system bus through a power distribution line. In this situation, the generator and the power system together supply a local load. The load is typically represented by a parallel *RLC* load [4]. The output power of the generator is $P_{DG} + jQ_{DG}$, and the power flow to the local load is $P_L + jQ_L$; the difference power $P_N + jQ_N$ between $P_{DG} + jQ_{DG}$ and $P_L + jQ_L$ is provided (or consumed) by the distribution power system. The island, which includes the inverter and the local load, will be formed when the circuit breaker (CB) on the distribution line is open. If the difference power $P_N + jQ_N$ is considerable before the islanding, the voltage and frequency of the islanded system will experience an obvious change at this time. An islanding condition is detected if the indices from the voltage and frequency signals exceed certain thresholds. Frequency-based and voltage-based anti-islanding relays are representative examples of such schemes. The relays trip a distributed generator if the frequency or voltage measured at the DG terminal drifts outside the pre-established safe operation boundaries. Unfortunately, these relays are not one hundred percent reliable due to their inherent limitations. If the active/reactive power imbalance between the generator and the load is small, the islanded system will require some time to exhibit a detectable frequency or voltage change. As a result, the relays will not be able to provide anti-islanding protection in a timely manner. The corresponding system operating conditions are called the non-detection zones (NDZs) of the relays.

The active methods use the ability of the distributed generator to adjust its current, voltage, or frequency to perturb the load circuit and then monitor the response to detect a change indicating that the distribution network, with its stable voltage and frequency, and low impedance, has been disconnected. The active methods can be further divided into two types. The first type just injects disturbances into the grid and does not have feedback control for the perturbation. Impedance measurement, frequency/phase and voltage shift techniques belong to this type. In contrast, the

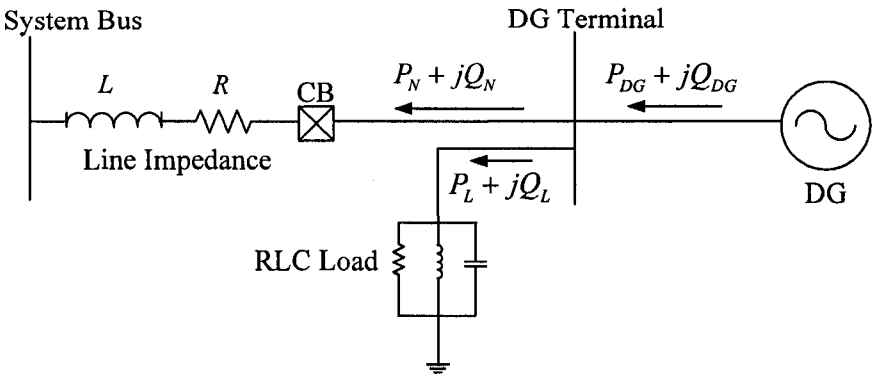

Figure 2.1: Single-line diagram of a DG system

other type of active method not only injects disturbance but also provides a positive feedback path for this injection. This type of anti-islanding method can be also identified as a positive feedback anti-islanding scheme.

The utility level methods and the communications-based methods are generally implemented at the utility side. Various forms of telecommunication are important requirements for their implementation. Based on this classification, all anti-islanding schemes identified by this thesis are summarized in Table 2.1.

Selecting a particular anti-islanding scheme for further research involving two main considerations. The first consideration is the popularity or industry acceptance of the scheme. For this thesis to produce results useful to industry, the schemes that have been or will be widely adopted by industry must be investigated. The literature review shows that although many anti-islanding schemes have been proposed, only a limited few have received industry-wide acceptance. The most commonly used schemes are the following:

- Passive methods: frequency and voltage based relays.
- Active methods: positive (frequency and/or voltage) feedback, impedance monitoring.

Table 2.1: Classification of Anti-Islanding Schemes

Categories	Name or Description	References
Local Detection Methods (Passive)	Under/Over Frequency Relay	[11]
	Under/Over Voltage Relay	[11]
	Voltage Phase Jump Detection	[11] - [15]
	Detection of Harmonics	[11] [13] [15] [16]
	Two-Step Passive Detection	[17] [18]
	Logic Rule-Based Detection	[19]
	Power Variation Detection	[20] - [22]
	$\|\partial f\|/\|\partial P\|$Detection	[23]
	Rate of Change of Frequency	[24] - [28]
Local Detection Methods (Active)	Impedance Measurement	[11] [13] [15] [29] - [33]
	Slip-Mode Frequency Shift	[11] [14] [15] [34] [35]
	Active Frequency Drift (AFD)	[11] [15] [34] [36] - [40]
	Sandia Frequency Shift (AFD with Positive Feedback)	[11] [15] [39] - [44]
	Sandia Voltage Shift	[11] [15] [41] [43] [44]
	GE Anti-Islanding Method	[45]
	Frequency Jump (Zebra)	[11] [46]
	ENS or MSD (A Device Using Multiple Methods)	[11] [47]
	Automatic Phase-shift Method	[48]
	Correlation Method	[49]
	Phase Shift Modulation	[50]
	Reactive Power Perturbation Method	[51] [52] [53]
	Ballard's Anti-Islanding Technique	[54]
	Reactive Error Export Detection	[55]
	Fault Level Monitoring	[56]
Utility Level Methods	Reactance Insertion	[11] [15] [57] - [59]
Communication-Based Methods	Power Line Signalling Scheme	[11] [60] [61]
	Signal Produced by Disconnect	[11]
	Supervisory Control and Data Acquisition	[11]
	Transfer Trip	[62] - [67]
	Cooperative Protection	[68]

- Communication-based methods: transfer trip.

The second consideration is that a scheme to be investigated must have the potential to affect power systems or other DGs in the system. For this reason, the passive methods do not need to be investigated since they do not have an impact on power systems. The same conclusion also applies to the transfer strip scheme since it relies mainly on telecommunication systems. These considerations leave the active methods as the focus of this investigation.

The active methods inject disturbances into the supply power system. Thus, they have the potential to affect power systems and other DGs depending on the strength of the disturbance injected. In fact, many papers have identified the intrusive nature of the active methods as one of the negative aspects. However, there is not any systematic investigation on the subject in the literature. Based on the above considerations, this thesis proposes to select the positive feedback scheme as the target anti-islanding method for research.

The positive feedback anti-islanding concept was first proposed in the early 1990's. Since then, various methods have been proposed and implemented based on the concept, such as Sandia frequency shift (SFS), Sandia voltage shift (SVS) and GE anti-islanding (GE AI) methods. These methods will be discussed and modeled in detail in the next chapter. Based on our survey, the positive feedback-based methods, especially the SFS and SVS methods, have gained wide industry acceptance among all the anti-islanding methods. Many inverters in the market are equipped with one of the variations of the Sandia scheme.

The positive feedback scheme has several potential negative impacts on power systems and other inverter-based DGs. First, the scheme always attempts to destabilize an inverter. When a system has multiple inverters, the collective destabilizing force could be too significant to be ignored. The consequence could be a reduced stability level of the distributed generation system or a reduced inverter

power output level if a certain stability level is to be maintained. Second, the positive feedback is produced by introducing a small distortion into the inverter output waveform. This distortion is a form of harmonic disturbance injection. When a system has multiple inverters, checking to determine when the distortion will become significant is worthwhile. Third, whether the distortion signals produced by different inverters will interact among themselves is unclear. If interactions occur, the effectiveness of the anti-islanding scheme could be compromised.

2.2 Positive Feedback Anti-Islanding Scheme

SFS and SVS are positive feedback concept-based active anti-islanding methods proposed by Sandia National Laboratories (SNL). Extensive testing has been conducted on these methods, and the effectiveness in detecting the islanding of DG systems has been broadly accepted by industry. According to the SNL grid-tied inverter testing, the combination of SFS and SVS is sufficient to prevent islanding conditions [44]. This section reviews the theory of operation, the modeling and the characteristics of SFS and SVS.

2.2.1 Principle of SFS and SVS

The SFS anti-islanding method utilizes positive feedback for frequency control of the inverter. In the islanding mode, this acceleration technology makes the frequency of the distributed generator continue to move when it reaches the resonant frequency of the *RLC* load shown in Figure 2.1. This result causes the island frequency to move beyond the limit of over/under frequency relay (UFR/OFR) even though the resonant frequency is close to the grid frequency. The theory of the operation of SFS is illustrated in Figure 2.2 where the voltage v_{DG} is the DG terminal or the PCC voltage in Figure 2.1 and is assumed to be sinusoidal; the current i_{DG} is the DG output current.

Without SFS, i_{DG} will have the same frequency and phase angle as v_{DG} because of the requirement of the unity power factor control [4]. When the SFS method

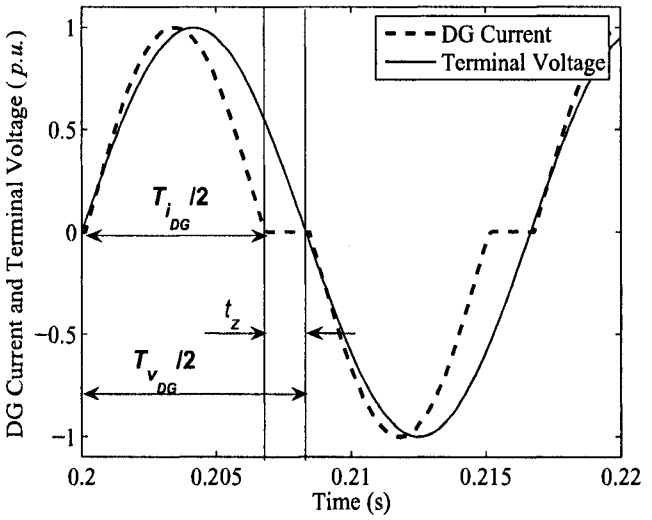

Figure 2.2: v_{DG} and i_{DG} waveforms for SFS

is considered, the frequency of v_{DG} is measured by using the zero crossing detection (ZCD) circuit, and the waveform of i_{DG} is slightly distorted according to the detected frequency. The frequency of i_{DG} ($f_{i_{DG}}$) is set to be slightly higher than the frequency of v_{DG} ($f_{v_{DG}}$) if the resonant frequency is higher than the grid frequency ($60Hz$). On the contrary, $f_{i_{DG}}$ is lower than $f_{v_{DG}}$ if the resonant frequency is lower than $60Hz$. $T_{v_{DG}}$ is the period of v_{DG}, $T_{i_{DG}}$ is the period of the sinusoidal portion of i_{DG}, and t_z is a dead or zero time [40]. The ratio of t_z to half of $T_{v_{DG}}$ is defined as the *chopping fraction* (cf). cf is not a constant for each cycle of i_{DG}. It is calculated by using Equation (2.1):

$$cf_k = cf_{k-1} + K_f \times (\Delta f_k) \tag{2.1}$$

where cf_{k-1} is the chopping fraction of the previous cycle, and K_f is the accelerating gain of the measured frequency error $\Delta f_k = f_k - f_0$ [11], [39]. f_0 is the grid frequency (60Hz), and f_k is the frequency of the DG terminal voltage at the kth cycle. Equation (2.1) can be rewritten in the following form:

$$cf_k = cf_0 + K_f \times \sum_{n=0}^{k} (f_n - f_0) \tag{2.2}$$

where cf_0 is the initial chopping fraction setting. The chopping fraction calculated by using Equation (2.1) or (2.2) is also called the *cumulative* cf because it includes the accumulative result of the bias of cf away from cf_0. Another form of chopping fraction called the *non-cumulative* cf is shown in Equation (2.3):

$$cf_k = cf_0 + K_f \times (f_k - f_0) \tag{2.3}$$

The *non-cumulative* cf reduces the total harmonic distortion(THD) of i_{DG} [39].

When a DG unit is connected to the grid, the frequency error of v_{DG} will be tiny, and the stability of the grid will forbid the drift of cf. If the grid is disconnected, the frequency of v_{DG} will increase or decrease toward the resonant frequency of the DG load. The gain K_f will amplify this frequency error. Consequently, the chopping fraction of i_{DG} will accelerate, so that the frequency of i_{DG} is changed in the same direction. Then the RLC load will drive the frequency of v_{DG} further away from the original value because the grid will not act to control v_{DG} any longer. Thus, a positive feedback is formed. Figure 2.3 illustrates the process of the positive feedback.

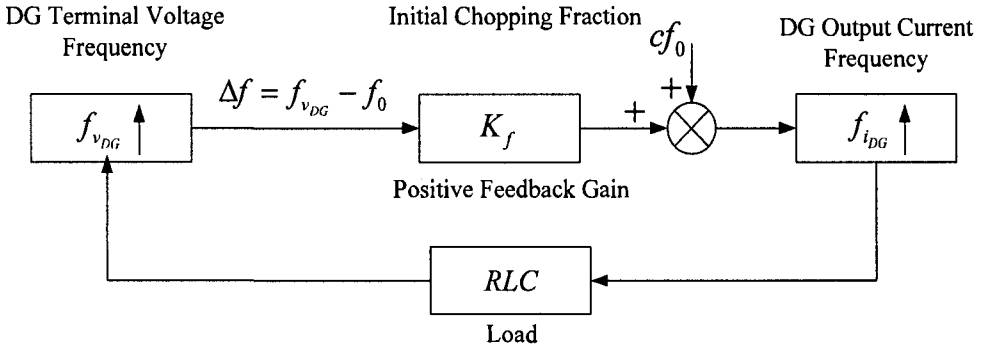

Figure 2.3: Schematic diagram of SFS

By using the positive feedback control, the frequency deviation of v_{DG} will continue to increase until it reaches the threshold of the UFR/OFR. Then the relays will act and trip the DG.

The principle of SVS is similar to that of SFS. SVS applies the positive feedback to the magnitude of v_{DG}. In this method, if the magnitude of v_{DG} increases or decreases, the inverter will reduce or raise the magnitude of i_{DG} correspondingly. The positive feedback relationship between v_{DG} and i_{DG} is shown in Figure 2.4.

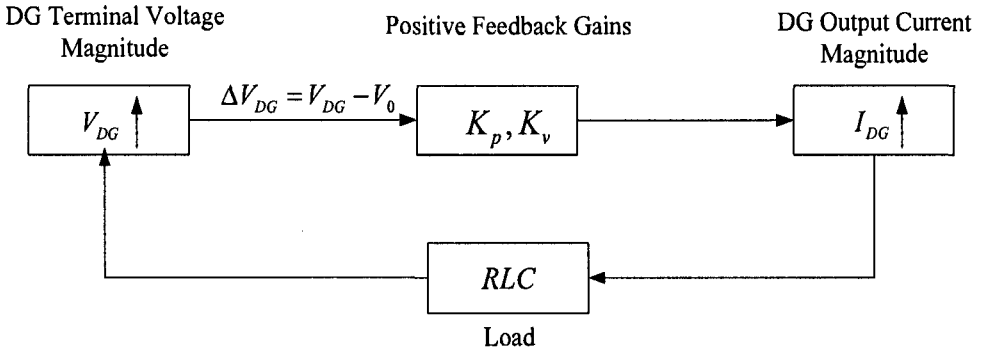

Figure 2.4: Schematic diagram of SVS

In Figure 2.4, V_{DG} is the RMS value of v_{DG}, I_{DG} is the RMS value of i_{DG}, ΔV_{DG} is the measured magnitude error of v_{DG}, K_p and K_v are the accelerating gains for the positive feedback loop. The voltage shift caused by SVS is small when the utility is connected for the regulation of the grid. If the utility is disconnected, the control of I_{DG} by K_p and K_v will drive V_{DG} over the limit of the under/over voltage relay (UVR/OVR). The mathematical description of this control is shown in Equation (2.4):

$$I_{DG} = \frac{P_{DG} + (P_{DG} \times K_p + K_v) \times (V_{DG} - V_0)}{V_{DG}} \tag{2.4}$$

where V_0 is the rated grid voltage, and P is the active power output of the DG system. This equation is suitable when the power factor of the inverter is unity. If this power

factor is not unity, Equation (2.4) can be rewritten as

$$I_{DG} = \frac{\sqrt{[P_{DG} + (P_{DG} \times K_p + K_v) \times (V_{DG} - V_0)]^2 + Q_{DG}^2}}{V_{DG}} \tag{2.5}$$

where Q_{DG} is the inverter reactive power output.

SVS is implemented by controlling the magnitude of the inverter output current, and SFS is realized by controlling the frequency of the inverter output current. The combination of these two methods makes anti-islanding detection more effective than using either SVS or SFS on its own.

2.2.2 Modeling of SFS and SVS

To investigate the anti-islanding impact of inverter-based DGs, adequate models to represent the SFS and SVS actions must be established. In this section, the SFS and SVS models for single- and three-phase inverters are reviewed.

Sandia's active islanding algorithms are developed for single-phase inverter units. A circuit diagram of the single-phase Voltage Source Inverter (VSI) is shown in Figure 2.5. The anti-islanding scheme is implemented in the inverter controller.

The block diagram interpretation model of the combination of SFS and SVS is presented in [41]. However, this model is not accurate. In the model, the inverter current phase angle error caused by SFS should not be integrated after the main grid is lost, because the SFS control mechanism does not change before and after the islanding.

More and more new DG units are using three-phase inverters as a grid interface, and the technology for three-phase inverter is gaining more and more practical value. As a result, three-phase inverter anti-islanding schemes are needed. GE researchers extended SFS/SVS to three-phase inverters by applying the chopping fraction to all three phases. However, these researchers found the method undesirable and

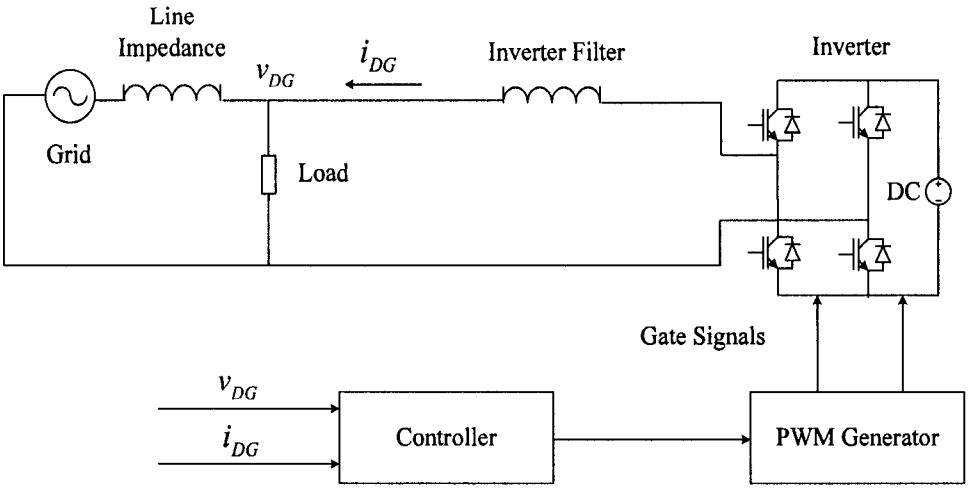

Figure 2.5: Circuit diagram of single-phase inverter unit

unpractical for some cases. For a three-phase, four-wire system, the chopping fraction could apply to each phase since each phase is independent. However, for a three-phase, three-wire system, applying the chopping fraction is more difficult since the three phases are not independent. If the SFS/SVS scheme is applied to two phases, the unsymmetrical distortion will further degrade the waveform quality. Therefore, a simple extension of SFS to a three-phase system is not a good solution. Alternatively, GE proposed a family of new anti-islanding schemes for three-phase inverters based on SFS/SVS [45].

2.3 Issues Concerned for Positive Feedback Anti-Islanding Scheme

The positive feedback anti-islanding scheme provides effective protection for inverter-based DGs against islanding, but will also introduce problems into power systems. Issues such as anti-islanding performance for multiple inverters, stability impact, and power quality pollution have been recognized. The following related aspects were addressed in this thesis.

2.3.1 Anti-Islanding Performance

NDZ, used as a performance index to evaluate different anti-islanding schemes, is defined as the condition in which the anti-islanding schemes cannot detect islanding and will not be able to provide anti-islanding protection in a timely manner. The expression methods for NDZ can be classified into two categories. One is expressed in the power imbalance space and the other is represented in the load parameter space.

The effectiveness of passive islanding detection schemes is usually assessed by using the NDZ represented in the power imbalance space. It is illustrated in Figure 2.6 where the power P_N and Q_N in Figure 2.1 are denoted as ΔP and ΔQ. It is assumed that the DG unit is installed with UVR/OVR and UFR/OFR. These relays will trip the generator if they detect that the DG terminal voltage and frequency are beyond the preset limits. When the DG unit is connected to the grid, this unit is operated in a steady state in which the DG terminal voltage and frequency are decided by the grid. Once the grid is disconnected from the DG for some reason an islanded system including the generator and the DG local load is formed. The islanded system will then go to another steady state in which the new DG terminal voltage and frequency are determined only by the DG system and its load. If the power imbalance $\Delta P+j\Delta Q$ is small before islanding, the changes of the DG terminal voltage and frequency will not be detectable. As a result, the relays will fail to trip the generator. However, if $\Delta P + j\Delta Q$ is increased to some value which makes the DG terminal voltage and frequency reach the relays' thresholds after islanding, the DG unit will be shut down. The possible combinations of ΔP and ΔQ which will not cause DG trip form the NDZ area plotted in Figure 2.6. Various passive anti-islanding methods will result in different NDZs in the power imbalance space. The smaller the NDZ is, the more efficient the method is.

- **NDZs of SFS and SVS**

Although the performance of passive anti-islanding methods can be easily evaluated in the power imbalance space, doing so for some active methods because of their theory of operation is inconvenient. In addition, for the parallel *RLC* load case, the

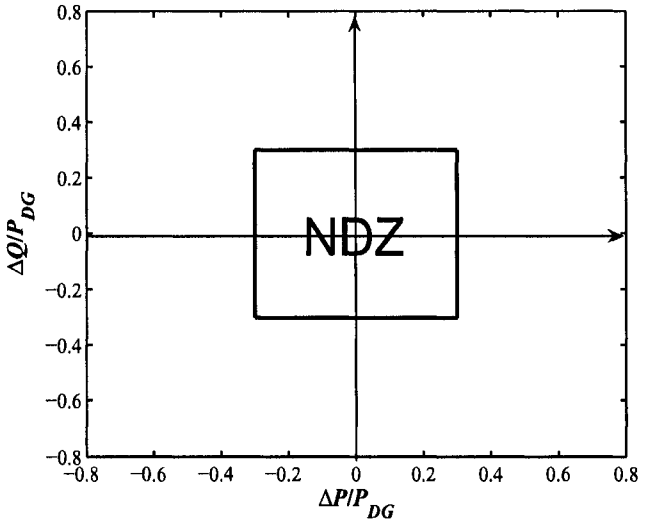

Figure 2.6: NDZ defined in the power imbalance space

mapping between the power imbalance space and the load parameters is not one-to-one, so that many combinations of R, L and C are mapped to one point in the ΔP versus ΔQ plane. Some of these combinations will cause non-detection of islanding, while others will not. This problem will result in misleading conclusions about the effectiveness of the test anti-islanding methods [69]. In order to overcome the above shortcomings, the NDZ represented in the load parameter space is proposed for use in the anti-islanding test of the parallel RLC load.

One load parameter space is defined by the load "nominalised capacitance" C_{norm} versus the load inductance L_L [39], which is also known as the "phase criteria". The load "nominalised capacitance" C_{norm} is defined as the ratio of the load capacitance to the capacitance (C_{res}) that resonates with the load inductance at the grid frequency:

$$C_{norm} = C_L/C_{res} = C_L\omega_0^2 L_L \tag{2.6}$$

where ω_0 is the radian frequency of the grid. In this load parameter space, the horizontal axis is defined in terms of L_L, and the vertical axis is defined in terms of

C_{norm}. The load resistance R_L is predefined to get the NDZ for different C_L and L_L values. As a result, for the evaluated anti-islanding method, each R_L has a related NDZ.

The NDZ of SFS was analyzed by using phase criteria in [39]. The analysis result indicated that the SFS method had an extremely narrow NDZ encompassing fewer RLC loads than the NDZs of the other methods such as the active frequency drift (AFD) method, the slide-mode frequency shift (SMS) method, and the OFR/UFR method. Thus, the phase criteria predicted that the SFS method was the most effective of the investigated islanding-prevention methods.

However, phase criteria have a drawback [37]. The positive impact of the reactive power introduced by active anti-islanding schemes becomes overestimated. In practice, for an islanding test procedure, this definition of the NDZ implies that the reactive-power portion originating from SFS is not compensated by the testing load. The reactive-power mismatch ΔQ is not adjusted to zero, implying that the tests do not represent a worst-case scenario. Therefore, the reactive power originating from SFS might be misinterpreted: a higher chopping fraction would lead to a decrease in the size of the NDZ. This decrease results in an incorrect NDZ when the load is precisely matched with a large parallel capacitance.

Another load parameter space is defined by the load quality factor Q_f versus the load resonant frequency f_r [70]. For parallel RLC loads, the quality factor is

$$Q_f = R_L\sqrt{C_L/L_L} \tag{2.7}$$

The frequency f_r has the definition

$$f_r = \frac{1}{2\pi\sqrt{L_L C_L}} \tag{2.8}$$

In this load parameter space, the different NDZs for the different R_L values do not need to be plotted because the quality factor Q_f already reflects the resistive element of the load. Positive feedback anti-islanding methods will disturb the DG output current, voltage or frequency to improve the islanding-detection performance. The derivation of NDZs in the load parameter space is based on the assumption that when the islanding occurs, the disturbance of the positive feedback methods will not cause the instability of the islanded system, which will eventually go to a new steady state. In this steady state, the following equation is satisfied for the SFS method:

$$\theta_{load} = \arctan(R_L(\frac{1}{\omega_s L_L} - \omega_s C_L)) = \phi_s \tag{2.9}$$

where θ_{load} is the phase angle of the RLC load at the new steady-state frequency ω_s, and the angle ϕ_s is the angle difference between the DG terminal voltage and current. If ω_s lies within the OFR/UFR trip limits, the RLC load is inside the NDZ. The analysis of the active methods' NDZs presented in [70] also demonstrated the effectiveness of SFS in the Q_f versus f_r space.

Generally speaking, the current methods for anti-islanding performance evaluation of the positive feedback methods are based on the assumption that the islanded DG system will be stable after islanding occurs, but under certain conditions, the islanded DG system could lose its stability because of strong positive feedback or high load power. The NDZ analysis in the power imbalance space or load parameter space cannot explain this kind of islanding phenomenon as this analysis does not provide dynamic information about the performance of the islanding-detection methods.

- **Interaction among Inverters**

The SFS and SVS methods have been tested and applied in different countries and found to be able to detect islanding effectively for a single grid-interconnected inverter. However, as the number and size of inverter units increases, the potential interaction among the inverters due to the anti-islanding actions could affect the

effectiveness of the methods or lead to unexpected problems.

In order to test the potential interaction caused by SFS/SVS among inverters, SNL designed and conducted a series of multi-inverter experiments [44]. The experimental circuit is shown in Figure 2.7. Three commercialized inverters were connected in parallel, and various loads including R, RL, RLC, RC, motor and motor with capacitive VAR compensation were configured for the tests. A distribution transformer was used for the connection of the utility grid and the inverters.

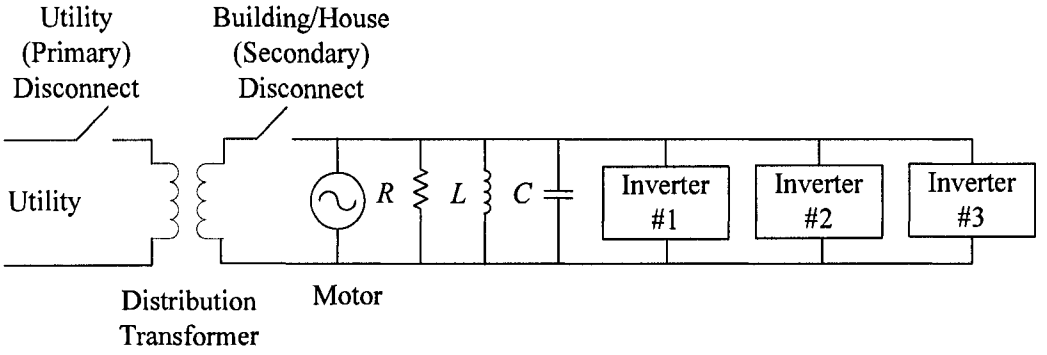

Figure 2.7: Diagram of SNL multi-inverter test circuit configuration

Two groups of tests were conducted based on the above circuit and different kinds of loads. In the first group, the inverters were equipped with only SFS, and in the second group, the inverters were equipped with the combination scheme of SFS and SVS. The results showed that in almost all the tests, the inverters disconnected themselves within the 2 seconds required by IEEE Std. 929-2000 [5] when the utility grid is lost. However, the islanding lasted for a long time when the inverters provided power to a parallel RLC load with the quality factor of 11 in the first group. These tests were designed to identify problems with islanding, and the problems identified tended to be more *worst case* than *typical case*. Thus, although too high of a value for Q_f is unrealistic (the maximum Q_f value is 2.5 on an actual distribution feeder [43]), the experiment results showed that multiple inverters could compromise the effectiveness of SFS.

As well, [71] points out that SFS and SVS may be subject to self-interference if an aggregate of units is attempting to push in one direction while a nearly equal aggregate of units is pushing in the other. Incorporating a small random offset in the rate at which each unit attempts to push should reduce this possibility.

In summary, the current understanding of the interactions among inverters due to anti-islanding controls is based mainly on experimentation. Limited theoretical analysis can be found in the literature.

2.3.2 Stability Impact

In practical power distribution systems, the grid is not an infinite source with zero impedance. As a result, the voltage at the DG terminal is not an ideal voltage source. Conceptually, if the positive feedback of the anti-islanding scheme is strong enough, the inverter can destabilize the local system, including the inverter and the load.

The positive feedback scheme seeks to destabilize DGs if perturbations or disturbances from power systems such as large load switching are present, at this time, the voltage at the PCC point will generally exhibit a short transient. The magnitude and settling time of this transient will depend primarily on the size of the change in the load, and on the impedance of the grid. Also, the positive feedback gain will make a great contribution to the degree of the transient. Reference [39] investigated the potential impact of SFS on the system transient response by using simulations. The simulation results showed that SFS did not have a significant effect on the system transient response. The effect was smaller for the higher-impedance transformers because the higher impedance served to damp more effectively the oscillations introduced by the SFS-equipped inverter. Unfortunately, [39] did not provide theoretical justifications for the study results, so whether this conclusion is applied to other scenarios is unclear. Actually, the transient response problem of the positive feedback scheme would grow more severe as the penetration level of the inverters into the network increases [11].

Reference [72] concluded that in initial studies of the WSCC system (the western North American grid, comprising all of the continental U.S. and Canada west of the Rockies), the destabilization of SFS was not identified, and that the inherent stabilization effect of the generation located close to the load might counteract any destabilization caused by the active anti-islanding function of SFS. However, in [73] it was found that the positive feedback anti-islanding scheme based on decreasing DG power output in response to declining frequency had an adverse effect on the recovery of the bulk system from large disturbances.

The stability problem associated with the positive feedback anti-islanding scheme was also discussed in [45]. Herein, GE's anti-islanding scheme for three-phase inverters was discussed. A case study found that the anti-islanding control destabilized the investigated power system, with growing oscillations of voltage and frequency. GE's anti-islanding scheme is also based on the positive feedback concept. As a result, this anti-islanding scheme will have a substantial impact on the power systems with DG.

In the literature, the stability issue related to the positive feedback anti-islanding scheme has been noted, but no thorough research has been done to quantify how the positive feedback anti-islanding control affects the stability of the DG and the interconnected power systems.

2.4 Summary

Inverter-based DGs are one of the most common DG technologies in power distribution systems. These DGs are small in size and can appear in large quantities. Many DG-to-DG and DG-to-system interaction issues associated with inverter-based DGs are unique and have not been investigated. This thesis proposed investigating the impact of multiple inverter-based DGs on power systems and the interactions among the inverters, with the inverter resident anti-islanding schemes as the main focus.

A survey on DG anti-islanding protection is presented in this chapter. According to the survey results, the published DG islanding detection methods are classified into four categories: passive local methods, active local methods, utility level methods and communication-based methods. Based on the review of various inverter-based anti-islanding schemes, the positive feedback anti-islanding scheme is selected to study the impact of inverter resident anti-islanding schemes on power systems and other inverters.

The positive feedback anti-islanding scheme is one of the active local methods which facilitate DG islanding detection by injecting disturbances into the interconnected grid. This scheme can be divided into the frequency-based positive feedback method (SFS) and the voltage-based positive feedback method (SVS). Computer models of SFS and SVS for a single-phase inverter have been developed, and the performance of the anti-islanding methods has been verified through theoretical analysis and experimental tests. However, little work has been done on the interactions among inverters and the impact of multiple inverters on power systems due to positive feedback anti-islanding controls. The limited experimental results show the effectiveness of the positive feedback anti-islanding scheme will be compromised when a number of inverters are connected to the utility grid in parallel. The initial research work conducted by NREL indicates that SFS/SVS has a potential stability impact on power distribution systems with high penetration and multiple inverters. Motivated by the review results on the addressed concerns, this thesis developed an analytical method to provide the theoretical foundations for the investigation of these problems.

Chapter 3

Modeling of Inverter-Based DG Systems

The first step to address the concern of the impact of the inverter-based DG and the associate positive feedback anti-islanding scheme is to establish adequate models to represent the inverter and anti-islanding actions at the level of interconnected systems. This chapter describes the modeling of the grid-connected inverters and the positive feedback anti-islanding control. The developed models can be used as analytical tools for both DG system stability analysis and anti-islanding scheme design.

3.1 Modeling of Grid-Connected Inverters

VSI and Current Source Inverter (CSI) are the two types of inverter usually used in the inverter-based DG applications. With the development of DG technologies VSI has gained the popularity against CSI as it is more easily controlled to satisfy the requirements of the DG interconnection. For example, the characteristic of the VSI output current control is more suitable for the designing of active anti-islanding methods [23], [48], [51]. In this thesis VSI is used as the DG interface with the grid and the research is mainly focused on this type of inverter.

The topology of a typical three-phase grid-connected VSI is shown in Figure 3.1 where the switching function inverter model is used. However, the average inverter model is more suitable for the analytical analysis [45]. Figure 3.2 shows the average model of a three-phase VSI. In the average inverter model the pulse-width modulated

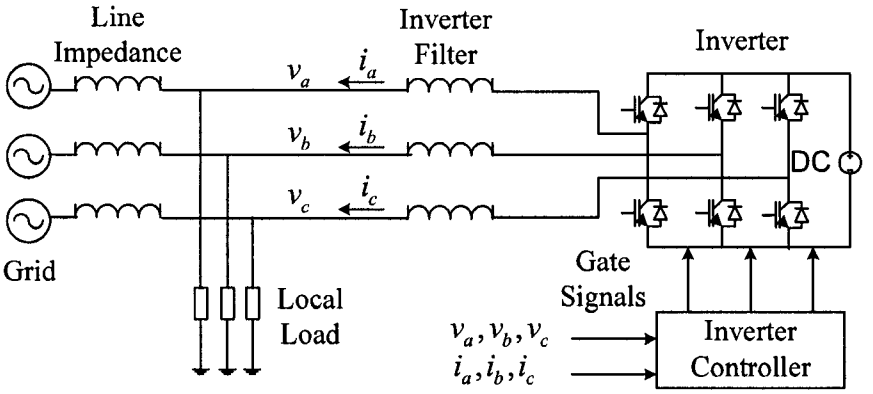

Figure 3.1: Three-phase grid-connected VSI

(PWM) pattern generator, the DC source and the switching power electronics devices, such as insulated gate bipolar transistors (IGBTs), are replaced by ideal voltage sources (v_{sa}, v_{sb}, v_{sc}) which are controlled by the inverter controller block in Figure 3.2. The inductance of the inverter series filter is represented by L_s. The sum of the inverter terminal voltages (v_a, v_b, v_c) and the voltage drop across the filter inductor generates the voltages v_{sa}, v_{sb}, v_{sc}.

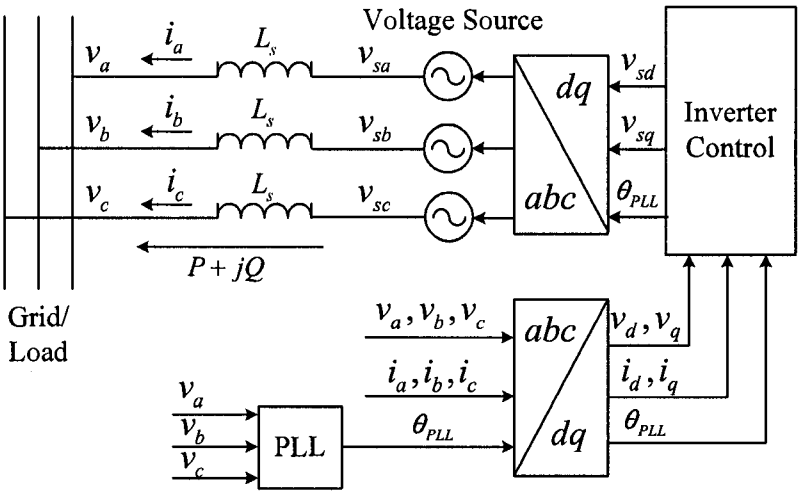

Figure 3.2: Three-phase average VSI model

The three-phase inverter terminal voltages can be assumed as:

$$\begin{aligned} v_a &= V\cos(\omega t + \delta_0) \\ v_b &= V\cos(\omega t - \frac{2}{3}\pi + \delta_0) \\ v_c &= V\cos(\omega t + \frac{2}{3}\pi + \delta_0) \end{aligned} \tag{3.1}$$

where the voltage magnitude is V and the voltage frequency is ω. The initial phase angle δ_0 is a constant decided by the steady-state operation point of the power system. The inverter terminal voltages and the output currents (i_a, i_b, i_c) are first transformed to the synchronous dq frame and then sent to the inverter control block. The transformation between abc and dq is shown as follows:

$$\begin{bmatrix} v_d \\ v_q \end{bmatrix} = \frac{2}{3}\begin{bmatrix} \cos\theta & \cos(\theta - \frac{2}{3}\pi) & \cos(\theta + \frac{2}{3}\pi) \\ -\sin\theta & -\sin(\theta - \frac{2}{3}\pi) & -\sin(\theta + \frac{2}{3}\pi) \end{bmatrix}\begin{bmatrix} v_a \\ v_b \\ v_c \end{bmatrix} \tag{3.2}$$

$$\begin{bmatrix} v_a \\ v_b \\ v_c \end{bmatrix} = \begin{bmatrix} \cos\theta & -\sin\theta \\ \cos(\theta - \frac{2}{3}\pi) & -\sin(\theta - \frac{2}{3}\pi) \\ \cos(\theta + \frac{2}{3}\pi) & -\sin(\theta + \frac{2}{3}\pi) \end{bmatrix}\begin{bmatrix} v_d \\ v_q \end{bmatrix} \tag{3.3}$$

The relationship between abc frame and dq frame is also illustrated in Figure 3.3.

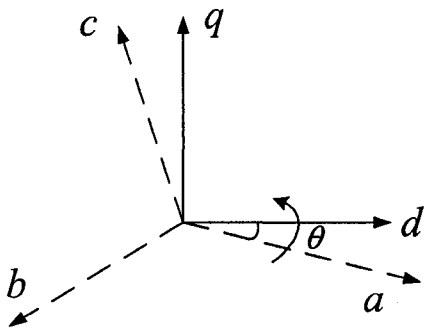

Figure 3.3: abc frame and dq frame

The angle θ used in the transformation is the inverter terminal voltage angle $\omega t+\delta_0$. It can be acquired by a three-phase PLL which also acquires the inverter terminal voltage frequency ω. The measured phase angle and frequency are denoted as θ_{PLL} and ω_{PLL}, respectively. The inverter control block includes the current regulator (current controller) and the power regulator (power controller). Figure 3.3 shows block diagram of the current and power controls. The proportional-integral (PI) controllers are used and two decoupling components ($i_d\omega_{PLL}L_s$ and $i_q\omega_{PLL}L_s$) are included in the current control as described in [74]. When the power regulator is presented in the inverter controller the inverter outputs the constant powers which are equal to the inverter input reference powers. This kind of control is the well known constant power control. On the contrary, the constant current control is realized if the power regulator is removed in Figure 3.2 and the inputs of the inverter control are the constant reference currents.

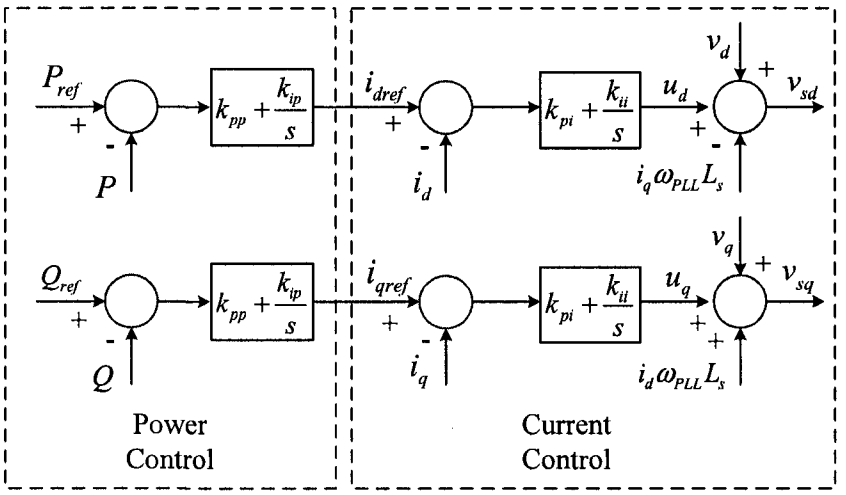

Figure 3.4: Diagram block of VSI current controller and power controller

In Figure 3.4, the Laplace operator is denoted by s and the PI controllers have the gains of k_{pp}, k_{ip}, k_{pi} and k_{ii}. By using the *abc-dq* transformation the inverter current control can be described in time domain by:

$$v_{sd} = (k_{pi} + \frac{k_{ii}}{s})(i_{dref} - i_d) - \omega_{PLL} L_s i_q + v_d \tag{3.4}$$

$$v_{sq} = (k_{pi} + \frac{k_{ii}}{s})(i_{qref} - i_q) - \omega_{PLL} L_s i_d + v_q \tag{3.5}$$

The output voltages of the controlled voltage sources are v_{sd} and v_{sq}. The filter circuit equations in Figure 3.2 are written as follows:

$$v_{sd} = L_s p i_d - \omega_{PLL} L_s i_q + v_d \tag{3.6}$$

$$v_{sq} = L_s p i_q - \omega_{PLL} L_s i_d + v_q \tag{3.7}$$

where p is the derivative operator. Equations (3.4) - (3.7) can be rewritten in the following form:

$$u_d = (k_{pi} + \frac{k_{ii}}{s})(i_{dref} - i_d) \tag{3.8}$$

$$u_q = (k_{pi} + \frac{k_{ii}}{s})(i_{qref} - i_q) \tag{3.9}$$

$$u_d = L_s p i_d \tag{3.10}$$

$$u_q = L_s p i_q \tag{3.11}$$

where the outputs of the current control PI controllers are u_d and u_q. The current reference settings are i_{dref} and i_{qref} which can be defined as constants or controlled by the power control. The equations for the power controller are as follows:

$$i_{dref} = (k_{pp} + \frac{k_{ip}}{s})(P_{ref} - P) \tag{3.12}$$

$$i_{qref} = (k_{pp} + \frac{k_{ip}}{s})(Q_{ref} - Q) \tag{3.13}$$

where the power control input settings are P_{ref} and Q_{ref}. The active power and the reactive power measured from the inverter terminal are P and Q which can be calculated by:

$$P = v_d i_d + v_q i_q \tag{3.14}$$

$$Q = v_d i_q - v_q i_d \tag{3.15}$$

The above inverter controller equations are expressed in per-unit system. The three-phase per-unit system adopted in this thesis is as follows:

$$I_{base} = \frac{2}{3}\frac{S_{base}}{V_{base}}, Z_{base} = \frac{V_{base}}{I_{base}} \tag{3.16}$$

where V_{base} is the peak value of the system rated voltage and S_{base} is the three-phase system base power.

Another important part of the inverter model is the PLL, which provides the angle and the frequency information of the inverter terminal voltage to the *abc-dq* and *dq-abc* transformations and the frequency-based anti-islanding controllers. The operation theory of a three-phase PLL is shown in Figure 3.5 [75].

The inverter terminal voltage angle θ shown in Equation (3.1) can be expressed by Equation (3.17) if it is assumed that the change of the voltage frequency is reflected by the change of the voltage phase angle.

$$\theta = \omega_0 t + \delta \tag{3.17}$$

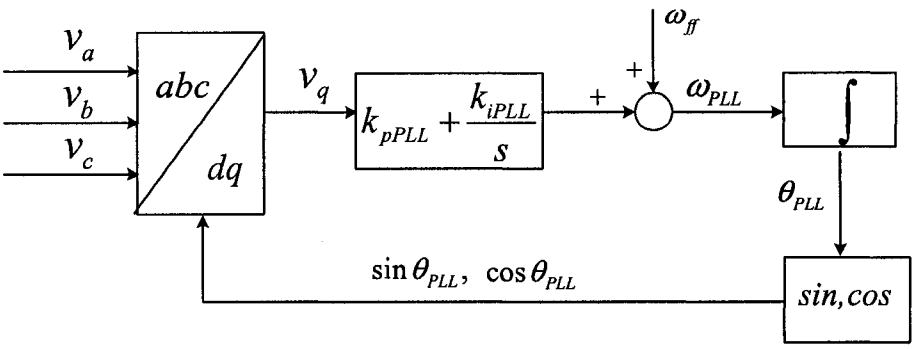

Figure 3.5: Three-phase PLL model

where the angle δ is an unknown variable and the derivative of δ is the voltage frequency change:

$$p\delta = \omega - \omega_0 \tag{3.18}$$

The measured inverter terminal voltage angle from PLL is θ_{PLL}. It is a signal tracking the real voltage angle θ. During the steady-state period they are equal to each other. However, there is a difference between them during the transient-state period. In the measurement, the q axis voltage v_q is obtained by using the *abc-dq* transformation at first. This is because the voltage v_q represents the error signal between the angle θ_{PLL} and the angle θ. It is not difficult to get Equation (3.19) when the inverter terminal voltages are transformed to the dq voltages and the angle used in the transformation is θ_{PLL}.

$$v_q = V\sin(\theta - \theta_{PLL}) = V\sin(\delta - \delta_{PLL}) \tag{3.19}$$

where the angle δ_{PLL} is the measured voltage phase angle and it is defined as:

$$\delta_{PLL} = \theta_{PLL} - \omega_0 t \tag{3.20}$$

The error signal is then processed by a PI controller to get the frequency bias. This frequency bias is added to the feedforward frequency ω_{ff}, which is equal to ω_0 in this case, to get the tracked voltage frequency ω_{PLL}. The angle used in the *abc-dq* transformation is acquired by the integral of this frequency. The PLL model can be expressed by the following equations:

$$\omega_{PLL} = (k_{p_{PLL}} + \frac{k_{i_{PLL}}}{s})V_q + \omega_0 \tag{3.21}$$

$$p\delta_{PLL} = \omega_{PLL} - \omega_0 \tag{3.22}$$

where the gains of the PI controller are $k_{p_{PLL}}$ and $k_{i_{PLL}}$.

The modeling process of single-phase grid-connected inverters is shown in Appendix A.

3.2 Modeling of Positive Feedback Anti-Islanding Scheme

The positive feedback anti-islanding control is integrated into inverter controller to realize its function. There is no additional hardware cost for this kind of anti-islanding scheme. According to the feature of the feedback signal, the positive anti-islanding scheme can be grouped as the frequency-based or the voltage-based method. Sometimes the two methods are combined together to accelerate the islanding detection. The mathematical models of the positive feedback anti-islanding scheme suitable for analytical studies are presented in this section.

3.2.1 Sandia Frequency and Voltage Methods

As shown in Figure 2.2, when studying the SFS method i_{DG} has a zero cross-over time in every half cycle. The Fourier series of the inverter output current can be expressed in Equation (3.23)

$$i_{DG}(t) = \sum_{k=1}^{\infty}(A_k \cos(k\omega t) + B_k \sin(k\omega t)) \tag{3.23}$$

where the Fourier coefficients A_k and B_k are obtained from the following equation:

$$A_k = \frac{1}{T_{i_{DG}}} \int_0^{T_{i_{DG}}} i_{DG}(t) \cos(k\omega t) dt \tag{3.24}$$

$$B_k = \frac{1}{T_{i_{DG}}} \int_0^{T_{i_{DG}}} i_{DG}(t) \sin(k\omega t) dt \tag{3.25}$$

A_k and B_k will not be zero for i_{DG} is neither odd nor even. The fundamental component of i_{DG} is shown in Equation (3.26):

$$i_{DG1}(t) = A_1 \cos(\omega t) + B_1 \sin(\omega t) = I_1 \sin(\omega t + \theta_1) \tag{3.26}$$

It has a phase shift θ_1 with respect to the i_{DG} waveform. Based on Equations (2.1) and (3.24) - (3.26), θ_1 is calculated as follows:

$$\theta_1 = \frac{1}{2}\omega t_z = \frac{\pi}{2} cf \tag{3.27}$$

Usually, the high order Fourier coefficients of i_{DG} are small and can be neglected. Then v_{DG} is a function only of i_{DG1}, the fundamental component of i_{DG}. As a result, the frequency error between v_{DG} and i_{DG} is mapped to this equivalent phase angle change θ_1. The waveforms of i_{DG}, i_{DG1} and v_{DG} are shown in Figure 3.6.

From the above analysis, the assumption that i_{DG1} is used to replace i_{DG} can be made to simplify the analysis of SFS in some applications, such as power flow calculations, voltage stability investigations, short circuit current estimations and so on. Thus, the SFS voltage and the equivalent inverter current shown in Figure 3.6 can be expressed by:

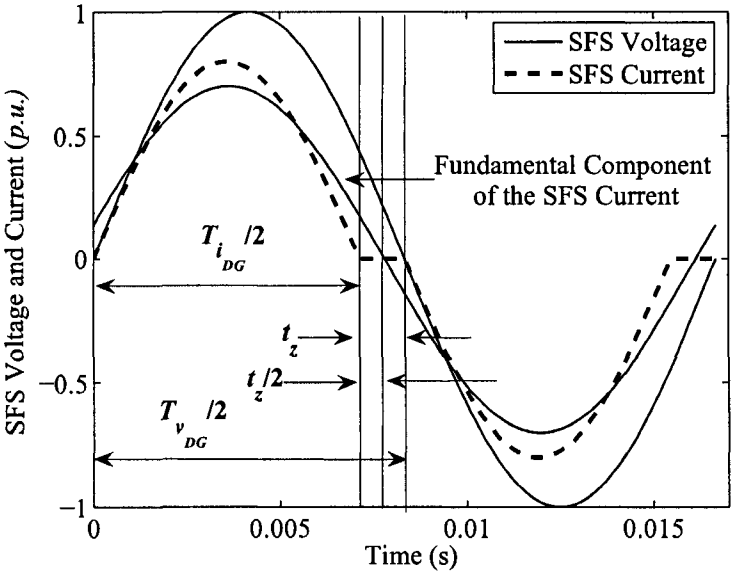

Figure 3.6: SFS voltage and current waveforms

$$v_{DG} = V \sin(\omega t) \tag{3.28}$$

$$i_{DG} = I \sin(\omega t + \theta_f) \tag{3.29}$$

where θ_f is θ_1 in Equation (3.27).

Based on the above assumption the diagram block of the SFS model is displayed in Figure 3.7.

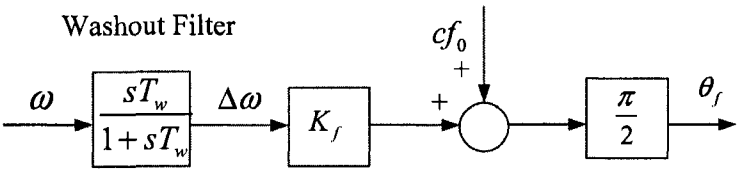

Figure 3.7: Diagram block of the SFS model

In a practical implementation, a washout filter shown in Figure 3.7 is used to get the inverter voltage frequency deviation $\Delta\omega$ [41], [43]. The time constant of the filter is T_w. In single-phase systems the SFS block output θ_f is added to the phase angle of the inverter output current, which can be seen from [41]. However, the SFS model in [41] is not accurate enough for islanding situations, because the phase angle deviation caused by SFS should not be integrated after the power system is lost as the SFS control mechanism does not change before and after the islanding is formed. The variation of the inverter voltage frequency is caused by power imbalance in the islanded system, not by SFS itself. Thus, the model in Figure 3.7 applies for both the grid parallel (GP) mode and the standalone (SA) mode. The mathematical description of the SFS model with *non-cumulative cf* is as follows:

$$\theta_f = \frac{\pi}{2}(cf_0 + K_f \frac{sT_w}{1+sT_w}\omega) \tag{3.30}$$

where the frequency ω is obtained by PLL.

Based on the above analysis, the SFS model was extended to three-phase inverter systems in this thesis, which is shown in Figure 3.8 for constant current-controlled inverter and Figure 3.9 for constant power-controlled inverter.

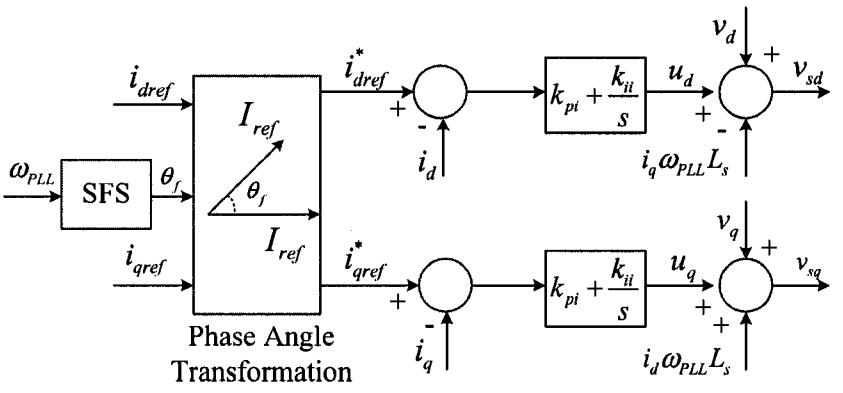

Figure 3.8: SFS extension to constant current-controlled three-phase inverter systems

In the three-phase extension, the inverter voltage frequency measured from PLL

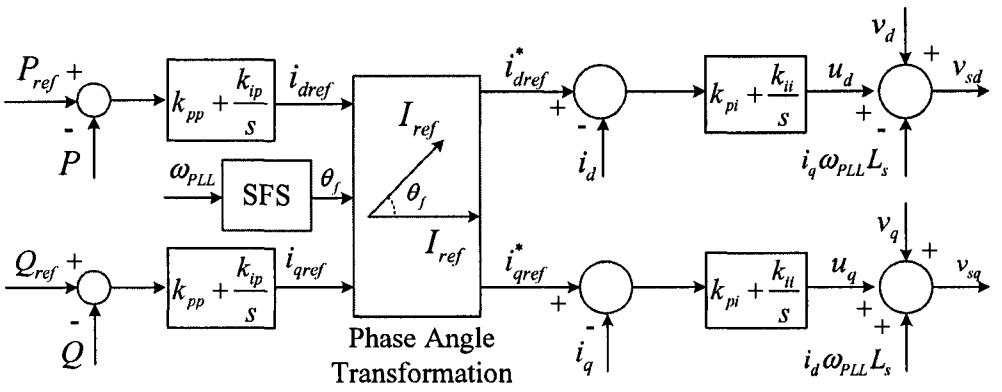

Figure 3.9: SFS extension to constant power-controlled three-phase inverter systems

ω_{PLL} is sent into the SFS block to get the phase angle θ_f. Then the inverter dq reference currents i^*_{dref} and i^*_{qref} are transformed to the currents i_{dref} and i_{qref} through the phase angle transform block. The reference current amplitude is I_{ref}. The transformation is defined as follows:

$$\begin{bmatrix} i^*_{dref} \\ i^*_{qref} \end{bmatrix} = \begin{bmatrix} \cos\theta_f & -\sin\theta_f \\ \sin\theta_f & \cos\theta_f \end{bmatrix} \begin{bmatrix} i_{dref} \\ i_{qref} \end{bmatrix} \tag{3.31}$$

The currents i^*_{dref} and i^*_{qref} are then used as the new current references for the inverter current control. Thus, the phase angle of the reference current is added by the angle θ_f while its amplitude is unchanged. The currents i_{dref} and i_{qref} in Figure 3.8 can be controlled by the inverter power control which is shown in Figure 3.9.

SVS applies the positive feedback to the magnitude of DG terminal voltage. The SVS model is shown in Figure 3.10. In the model, the magnitude of the DG terminal voltage is V which is calculated as follows:

$$V = \sqrt{v_d^2 + v_q^2} \tag{3.32}$$

The DG terminal voltage is passed through a washout filter to get the voltage deviation ΔV. The voltage error signal is modulated and transferred to the DG

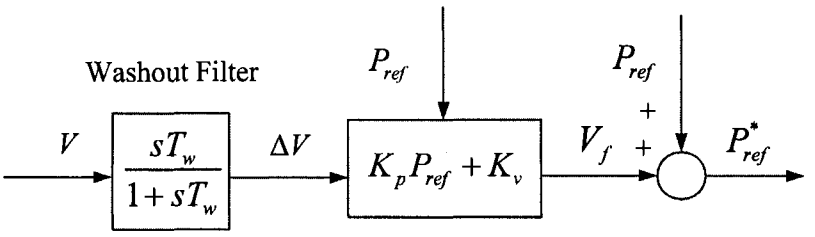

Figure 3.10: Diagram block of the SVS model

power reference shift. The shifted power reference is then sent to the power controller to form the positive feedback path. The positive feedback gains are K_v and K_p. The mechanism of SVS is actually to perturb the output power to change the voltage. It can also be easily extended to three-phase DG systems which is shown in Figure 3.11. The mathematical expression of SVS is shown as follows:

$$V_f = (K_pP_{ref} + K_v)\frac{sT_w}{1+sT_w}V \tag{3.33}$$

$$P^*_{ref} = P_{ref} + V_f \tag{3.34}$$

where P^*_{ref} is the new active power reference set in the inverter control.

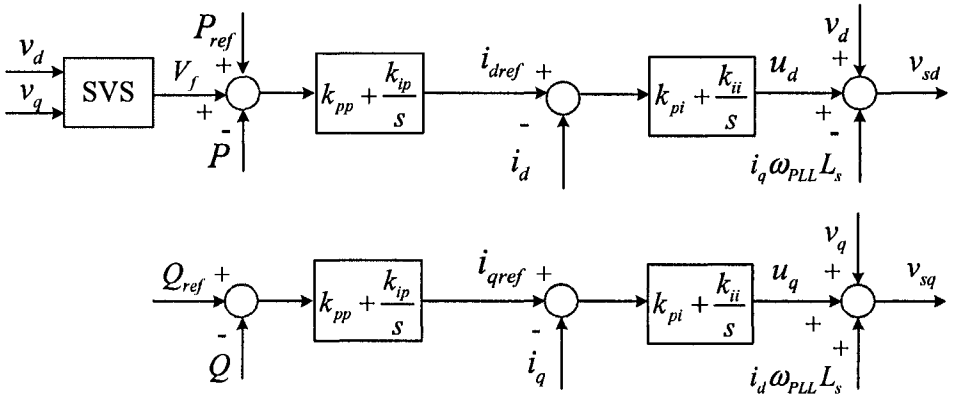

Figure 3.11: SVS extension to constant power-controlled three-phase inverter systems

3.2.2 GE Frequency and Voltage Methods

GE's positive feedback anti-islanding methods are mainly proposed in three-phase case. There are several types of GE Frequency Scheme (GEFS) and GE Voltage Scheme (GEVS) [45]. A representative GEFS is selected to present. Figure 3.12 displays the control mechanism of the selected GEFS. It is based on the constant power control. In Figure 3.12, the frequency measured from the network is passed through a low pass filter and a high pass filter to get the frequency variation of the DG-connected power system. The frequency error signal is amplified by a gain and introduced to the current reference path of the inverter controller. The time constants of the low pass and washout filter are T_l and T_w, respectively. The positive feedback gain is K_f. The explanation of the positive feedback mechanism of this method can be seen from [45]. Based on the above control loop, the following additional anti-islanding control equations are added to the analytical inverter model of the DG system.

$$\theta_f = K_f(\frac{1}{1+sT_l})(\frac{sT_w}{1+sT_w})\omega \tag{3.35}$$

$$u_d = (k_{pi} + \frac{k_{ii}}{s})(i_{dref} + \theta_f - i_d) \tag{3.36}$$

A representative GEVS scheme is shown in Figure 3.13. The only difference between GEVS and GEFS is that GEVS uses the voltage signal v_d as the input of the positive feedback path.

3.3 Small-Signal Model of Single DG System

With the available inverter and positive feedback anti-islanding control models, the analytical models of the inverter-based DG systems can be obtained correspondingly. This section presents the developed small-signal stability model of the three-phase DG system shown in Figure 2.1. The SFS control extended to three-phase system is selected as the representative control in the model to investigate the impact of the

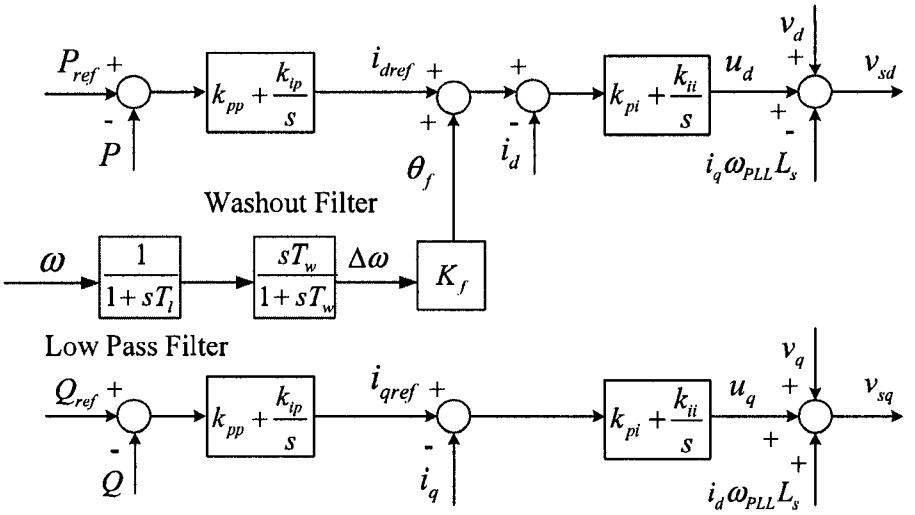

Figure 3.12: Diagram block of GEFS model

positive feedback anti-islanding scheme on the DG system stability. The study of the other positive feedback anti-islanding controls can be easily realized based on the developed DG system model.

3.3.1 Single DG System with Parallel *RLC* Load

Figure 3.14 shows a three-phase, grid-connected, inverter-based DG system with parallel *RLC* load. In this figure, an inverter-based distributed generator is connected to a distribution power system which is usually thought as weak power system and has relatively large R/X ratio. R and L are the resistance and the inductance of the distribution line respectively. CB is the circuit breaker between the DG system and the main grid. The output power of the generator is $P + jQ$ and the power flow on the *RLC* load is $P_L + jQ_L$. The difference power $(P_N + jQ_N)$ between $P + jQ$ and $P_L + jQ_L$ is provided (or consumed) by the distribution system. Its positive direction is defined as from the DG side to the network side. The DG output currents are i_a, i_b, i_c and the three-phase parallel *RLC* load has the branch currents i_{Ra}, i_{Rb}, i_{Rc} (R_L branch), i_{La}, i_{Lb}, i_{Lc} (L_L branch), and i_{Ca}, i_{Cb}, i_{Cc} (C_L branch). i_{Na}, i_{Nb}, i_{Nc} are the currents flowed on the distribution line. v_a, v_b, v_c are the terminal voltages of the

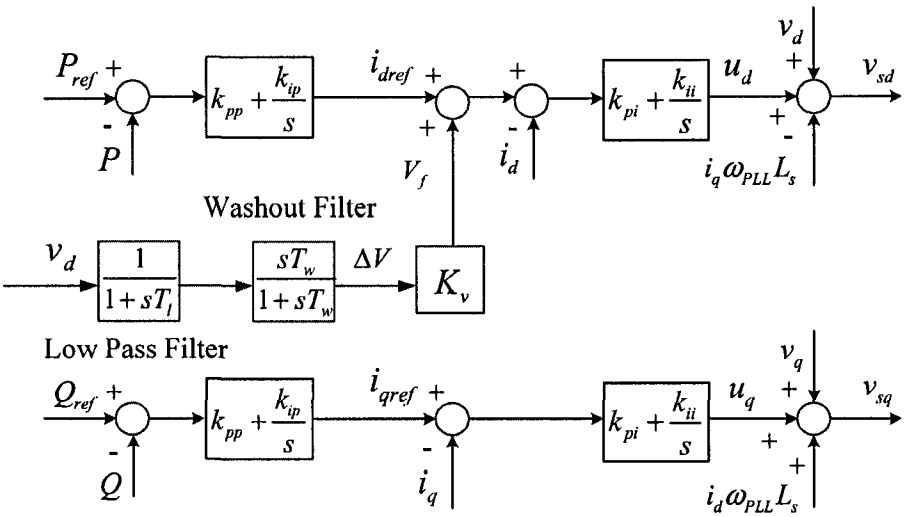

Figure 3.13: Diagram block of GEVS model

DG system and e_a, e_b, e_c are the voltage sources of the supply power system.

The network and the RLC load can be expressed by the following equations:

$$\begin{aligned} v_a &= Ri_{Na} + Lpi_{Na} + e_a \\ v_b &= Ri_{Nb} + Lpi_{Nb} + e_b \\ v_c &= Ri_{Nc} + Lpi_{Nc} + e_c \end{aligned} \tag{3.37}$$

$$\begin{aligned} i_a &= i_{Ra} + i_{La} + i_{Ca} + i_{Na} \\ i_b &= i_{Rb} + i_{Lb} + i_{Cb} + i_{Nb} \\ i_c &= i_{Rc} + i_{Lc} + i_{Cc} + i_{Nc} \end{aligned} \tag{3.38}$$

$$\begin{aligned} i_{Ra} &= \frac{v_a}{R_L} \\ i_{Rb} &= \frac{v_b}{R_L} \\ i_{Rc} &= \frac{v_c}{R_L} \end{aligned} \tag{3.39}$$

$$\begin{aligned} v_a &= L_L pi_{La} \\ v_b &= L_L pi_{Lb} \\ v_c &= L_L pi_{Lc} \end{aligned} \tag{3.40}$$

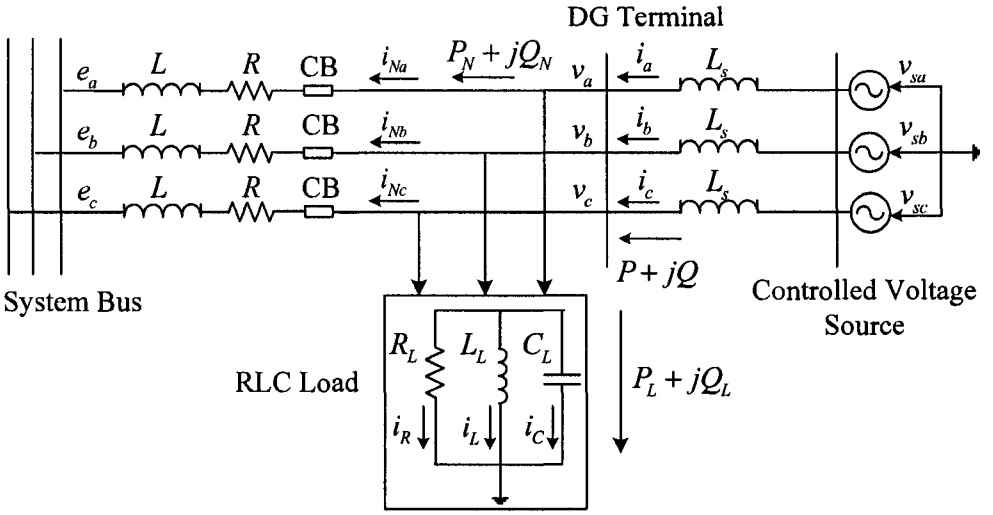

Figure 3.14: Schematic diagram of single DG system with *RLC* load

$$\begin{aligned} i_{Ca} &= C_L p v_a \\ i_{Cb} &= C_L p v_b \\ i_{Cc} &= C_L p v_c \end{aligned} \tag{3.41}$$

These equations can be represented in the dq frame which is shown in Figure 3.3. The transformed equations are as follows:

$$\begin{aligned} v_d &= R i_{Nd} + L p i_{Nd} - \omega_{PLL} L i_{Nq} + e_d \\ v_q &= R i_{Nq} + L p i_{Nq} + \omega_{PLL} L i_{Nd} + e_q \end{aligned} \tag{3.42}$$

$$\begin{aligned} i_d &= i_{Rd} + i_{Ld} + i_{Cd} + i_{Nd} \\ i_q &= i_{Rq} + i_{Lq} + i_{Cq} + i_{Nq} \end{aligned} \tag{3.43}$$

$$\begin{aligned} i_{Rd} &= \frac{v_d}{R_L} \\ i_{Rq} &= \frac{v_q}{R_L} \end{aligned} \tag{3.44}$$

$$\begin{aligned} v_d &= L_L p i_{Ld} - \omega_{PLL} L_L i_{Lq} \\ v_q &= L_L p i_{Lq} + \omega_{PLL} L_L i_{Ld} \end{aligned} \tag{3.45}$$

$$\begin{aligned} i_{Cd} &= C_L p v_d - \omega_{PLL} C_L v_q \\ i_{Cq} &= C_L p v_q + \omega_{PLL} C_L v_d \end{aligned} \tag{3.46}$$

In the above equations, the angle used for *abc-dq* transformation is the DG terminal voltage θ_{PLL} acquired from PLL. It has the form of:

$$\theta_{PLL} = \omega_{PLL} t + \delta_0 \tag{3.47}$$

Equation (3.47) can be also written as:

$$\theta_{PLL} = \omega_0 t + \delta_{PLL} \tag{3.48}$$

with the relationship:

$$\delta_{PLL} = (\omega_{PLL} - \omega_0) t + \delta_0 \tag{3.49}$$

By this means, if the supply power system voltages are assumed to be:

$$\begin{aligned} e_a &= E\cos(\omega_0 t) \\ e_b &= E\cos(\omega_0 t - \frac{2}{3}\pi) \\ e_c &= E\cos(\omega_0 t + \frac{2}{3}\pi) \end{aligned} \tag{3.50}$$

where the voltage magnitude E is set as 1 in the per unit system, then they have the following *dq* form equations:

$$\begin{aligned} e_d &= E\cos(\delta_{PLL}) \\ e_q &= -E\sin(\delta_{PLL}) \end{aligned} \tag{3.51}$$

The diagram of e_d, e_q in dq frame is shown in Figure 3.15. It can also be seen that the DG terminal voltage v_d is equal to V and v_q is zero during the steady state as mentioned in the PLL modeling part.

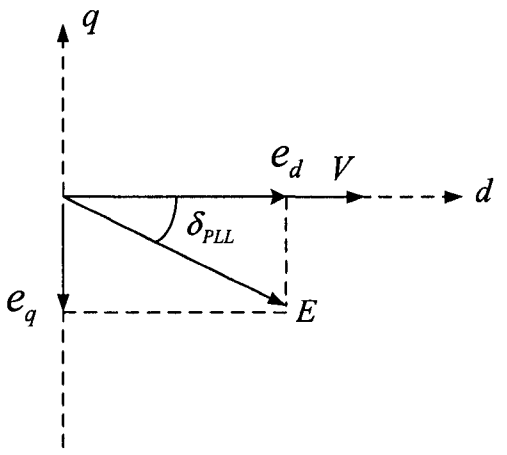

Figure 3.15: Diagram of e_d, e_q in dq frame

Altogether, the small-signal model of single DG system can be acquired by linearizing the modeling equations of three-phase inverter, SFS control, network and DG load. The model is shown in Appendix B.

3.3.2 Single DG System with Motor Load

A small-signal model of the single DG system with motor load was also developed in this thesis. The model provides a theoretical tool for the investigation of the interaction between the positive feedback anti-islanding control and the dynamics of the motor load. The schematic diagram of single DG system with induction motor load is displayed in Figure 3.16.

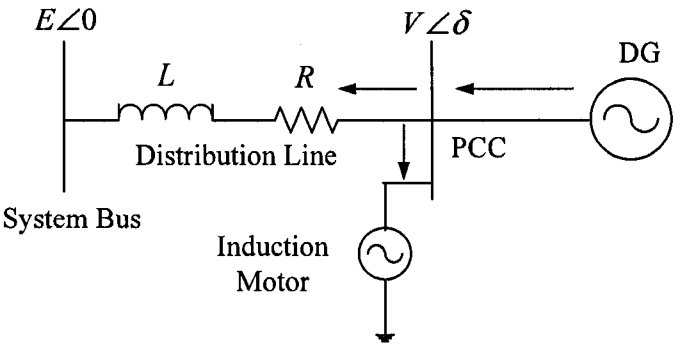

Figure 3.16: Schematic diagram of single DG system with motor load

In this model, the inverter modeling part including the SFS control is the same with that in the single DG system with *RLC* load. The modeling equations for this part are expressed in the rotating dq frame with the transform angle θ_{PLL} which is get from PLL. However, the motor load and network equations will be expressed in the synchronous xy frame with the transform angle $\omega_0 t$ to facilitate the generalization of the model. Figure 3.17 shows the relationship between the two frames.

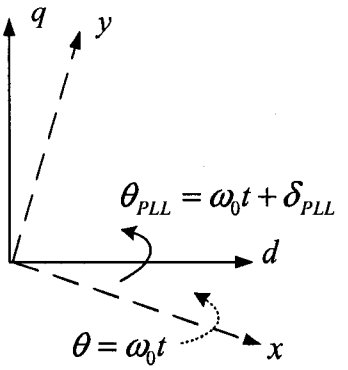

Figure 3.17: dq frame and xy frame

The motor and network equations are as follows:

- Motor Equations [76]

1. Stator Voltage Equations

$$\begin{aligned} v_x &= \frac{p\psi_{sx}}{\omega_0} - \psi_{sy} + R_s i_{sx} \\ v_y &= \frac{p\psi_{sy}}{\omega_0} + \psi_{sx} + R_s i_{sy} \end{aligned} \tag{3.52}$$

2. Rotor Voltage Equations

$$\begin{aligned} 0 &= \frac{p\psi_{rx}}{\omega_0} - \frac{\omega_0 - \omega_r}{\omega_0}\psi_{ry} + R_r i_{rx} \\ 0 &= \frac{p\psi_{ry}}{\omega_0} + \frac{\omega_0 - \omega_r}{\omega_0}\psi_{rx} + R_r i_{ry} \end{aligned} \tag{3.53}$$

3. Stator Flux Equations

$$\begin{aligned} \psi_{sx} &= (X_m + X_s) i_{sx} + X_m i_{rx} \\ \psi_{sy} &= (X_m + X_s) i_{sy} + X_m i_{ry} \end{aligned} \tag{3.54}$$

4. Rotor Flux Equations

$$\begin{aligned} \psi_{rx} &= (X_m + X_r) i_{rx} + X_m i_{sx} \\ \psi_{ry} &= (X_m + X_r) i_{ry} + X_m i_{sy} \end{aligned} \tag{3.55}$$

5. Torque Equations

$$T_e = \psi_{sx} i_{sy} - \psi_{sy} i_{sx} \tag{3.56}$$

$$\frac{p\omega_r}{\omega_0} = \frac{1}{2H}(T_e - T_m) \tag{3.57}$$

where the rotor of the motor are short-circuited and all the variables are on the stator side. v_x and v_y are the PCC voltage (motor stator voltage) or the DG terminal voltage components in the xy frame. The variables ψ_{sx}, ψ_{sy}, ψ_{rx} and ψ_{ry} are the components of the stator and rotor fluxes and i_{sx}, i_{sy}, i_{rx} and i_{ry} are the components of the stator and rotor currents. X_s and X_r are the stator and rotor leakage reactance, respectively. X_m is the magnetizing reactance. R_s is the stator resistance and R_r is the rotor resistance. ω_r is the rotor radian frequency. T_e is the electromagnetic transient torque of the motor and H is the inertia constant. The mechanical torque T_m is determined by the input load.

- xy and dq connection equations are given as:

$$\begin{bmatrix} v_d \\ v_q \end{bmatrix} = \begin{bmatrix} \cos\delta_{PLL} & \sin\delta_{PLL} \\ -\sin\delta_{PLL} & \cos\delta_{PLL} \end{bmatrix} \begin{bmatrix} v_x \\ v_y \end{bmatrix} \tag{3.58}$$

$$\begin{bmatrix} i_x \\ i_y \end{bmatrix} = \begin{bmatrix} \cos\delta_{PLL} & -\sin\delta_{PLL} \\ \sin\delta_{PLL} & \cos\delta_{PLL} \end{bmatrix} \begin{bmatrix} i_d \\ i_q \end{bmatrix} \tag{3.59}$$

- Network equations are given as:

$$\begin{aligned} v_x &= Ri_{Nx} + Lpi_{Nx} - \omega_0 Li_{Ny} + E \\ v_y &= Ri_{Ny} + Lpi_{Ny} + \omega_0 Li_{Nx} \end{aligned} \tag{3.60}$$

$$\begin{aligned} i_x &= i_{Nx} + i_{sx} \\ i_y &= i_{Ny} + i_{sy} \end{aligned} \tag{3.61}$$

where i_{Nx} and i_{Ny} are the components of the current flowing through the distribution line.

The linearized equations of the system model are shown in Appendix C.

3.3.3 Model Validation

The developed single DG system small-signal model with different types of load was verified in the time domain by comparing the dynamic responses for a power reference step obtained from the electromagnetic transient models, set up in Matlab/Simulink and PSCAD/EMTDC.

- Model Validation of the Single DG System with Parallel *RLC* Load

Figure 3.18 shows the small-signal model verification result for the single DG system with *RLC* load. An electromagnetic transient model of the same single DG system was developed in Matlab/Simulink as the reference. The average inverter model is used in the transient model at first. The parameter settings in both the small-signal model and the transient model are the same and they are listed in Table E.1 of Appendix E. The inverter is constant power-controlled. The active power reference of the inverter P_{ref} is stepped from 0.1 $p.u.$to 0.11 $p.u.$at the time constant 0.1s. From the figure one can see the corresponding variable responses of the two models due to this small disturbance match very well. Different system parameters and input references were tested. The comparison results, which are not shown here, also indicate the same phenomenon, demonstrating the accuracy of the developed small-signal model.

The washout filter in the SFS control is removed in the simulations as it will cause a long time for the systems to get to the steady state. The effect of the filter is replaced by the ideal frequency error $\Delta\omega = \omega - \omega_0$ in both of the models. From the modal analysis of the DG system small-signal model, it is known that the washout filter introduces a stable pole into the DG system and has little impact on the DG system stability. The neglect of the washout filter part in model verification will reduce the simulation time without changing the main characteristics of the DG system.

A further model verification is shown in Figure 3.19 where the DG system with the average inverter model (Simulink Average Model) is compared with the DG system with the switching inverter model (Simulink Switching Model) in Matlab/Simulink.

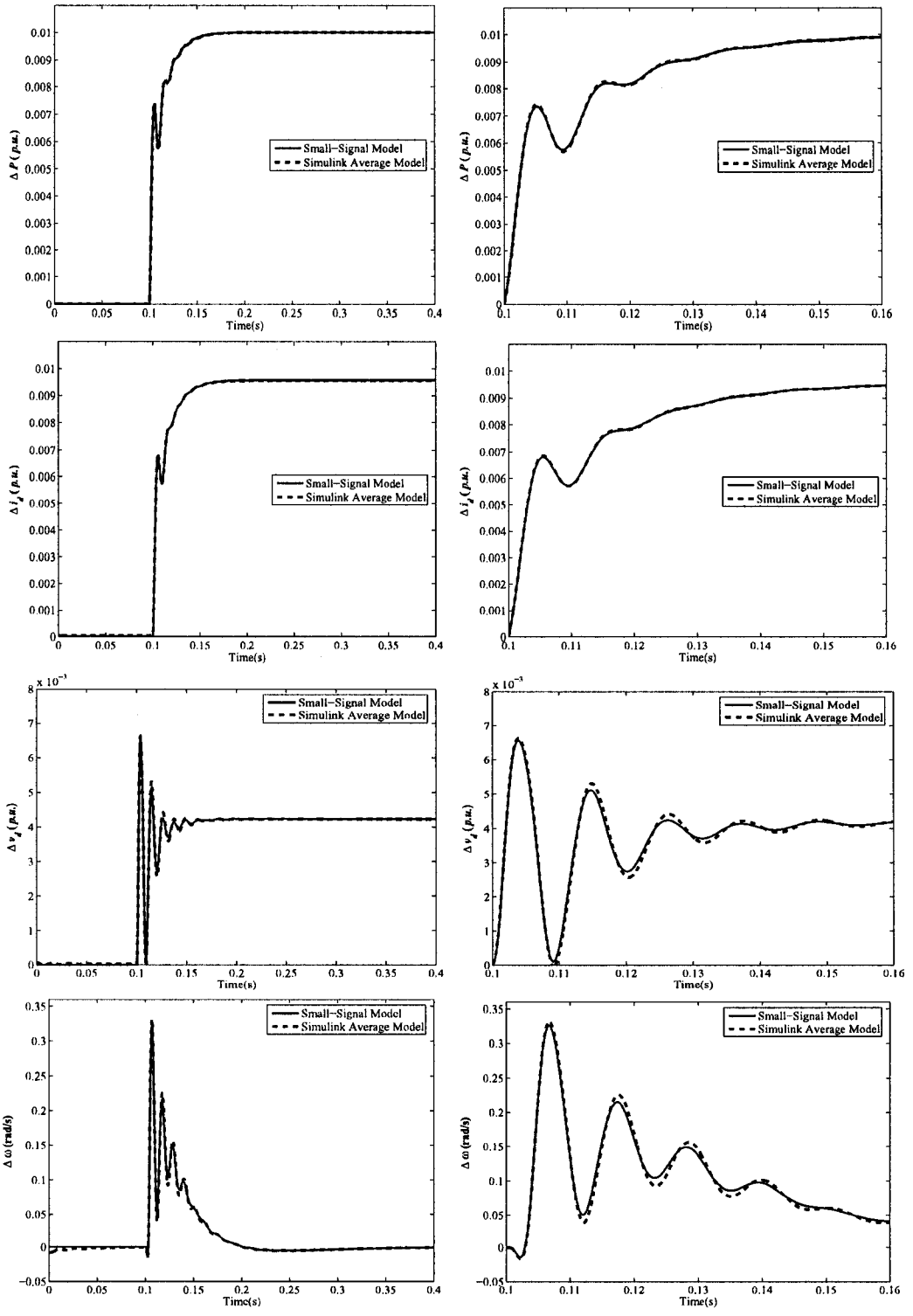

Figure 3.18: Small-signal model validation of the single DG system with *RLC* load - Simulink inverter average model (left: variable responses, right: dislocation of the variable responses)

The Simulink Switching Model includes the details of the PWM generator, IGBTs and DC source. Due to the switching noises, it is not convenient to compare the small-signal DG system model with the Simulink Switching Model directly. As a substitute, the Simulink Average model which has been shown representing the small-signal model during the small disturbance is used. A large disturbance is set in this model validation. In Figure 3.19, P_{ref} is stepped from 0.2 $p.u.$ to 0.3 $p.u.$ at 0.1s. The RLC load parameters are changed to $R_L = 1.08\Omega$, $L_L = 4.4mH$ and $C_L = 1.6mF$, correspondingly. In the simulations, the DC voltage of the inverter is $600V$ and the inverter switching frequency is $12.96kHz$. The comparison results show that the Simulink Average Model and the Simulink Switching Model are very close in steady state and transient state. This conclusion provides solid support for the use of the developed small-signal DG system model in later analysis.

The small-signal model of the single DG system with RLC load was also verified by the electromagnetic transient models setup in PSCAD/EMTDC. Figure 3.20 shows the comparison result between the small-signal model and the transient model with the average inverter model (PSCAD Average Model). Figure 3.21 shows the comparison result between the PSCAD Average Model and the transient model with the switching inverter model (PSCAD Switching Model). The system data and parameter settings for Figure 3.20 are the same with those for Figure 3.18. Similar, the data and parameters for Figure 3.21 and Figure 3.19 are identical.

- Model Validation of the Single DG System with Motor Load

Figure 3.22 displays the model validation result for the single DG system with induction motor load. In the figure, the small-signal model is compared with the electromagnetic transient model built in Matlab/Simulink. The average inverter model is used in the transient model. The system data are listed in Table E.2 of Appendix E. The small difference between the two models implies the correctness of the small-signal model which provides the foundation for the analytical analysis of interactions between positive feedback anti-islanding methods and dynamic loads.

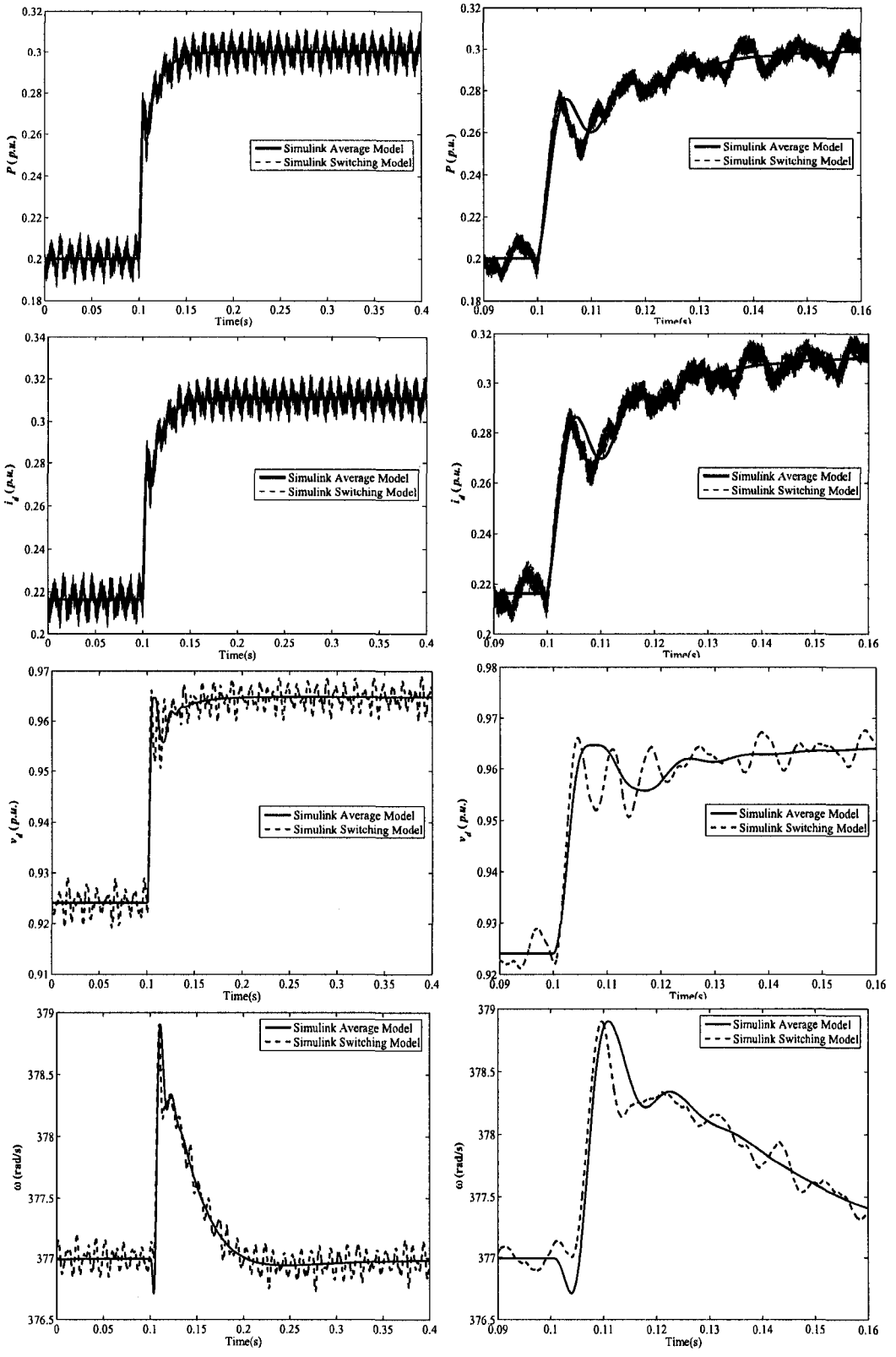

Figure 3.19: Small-signal model validation of the single DG system with *RLC* load - Simulink inverter switching model (left: variable responses, right: dislocation of the variable responses)

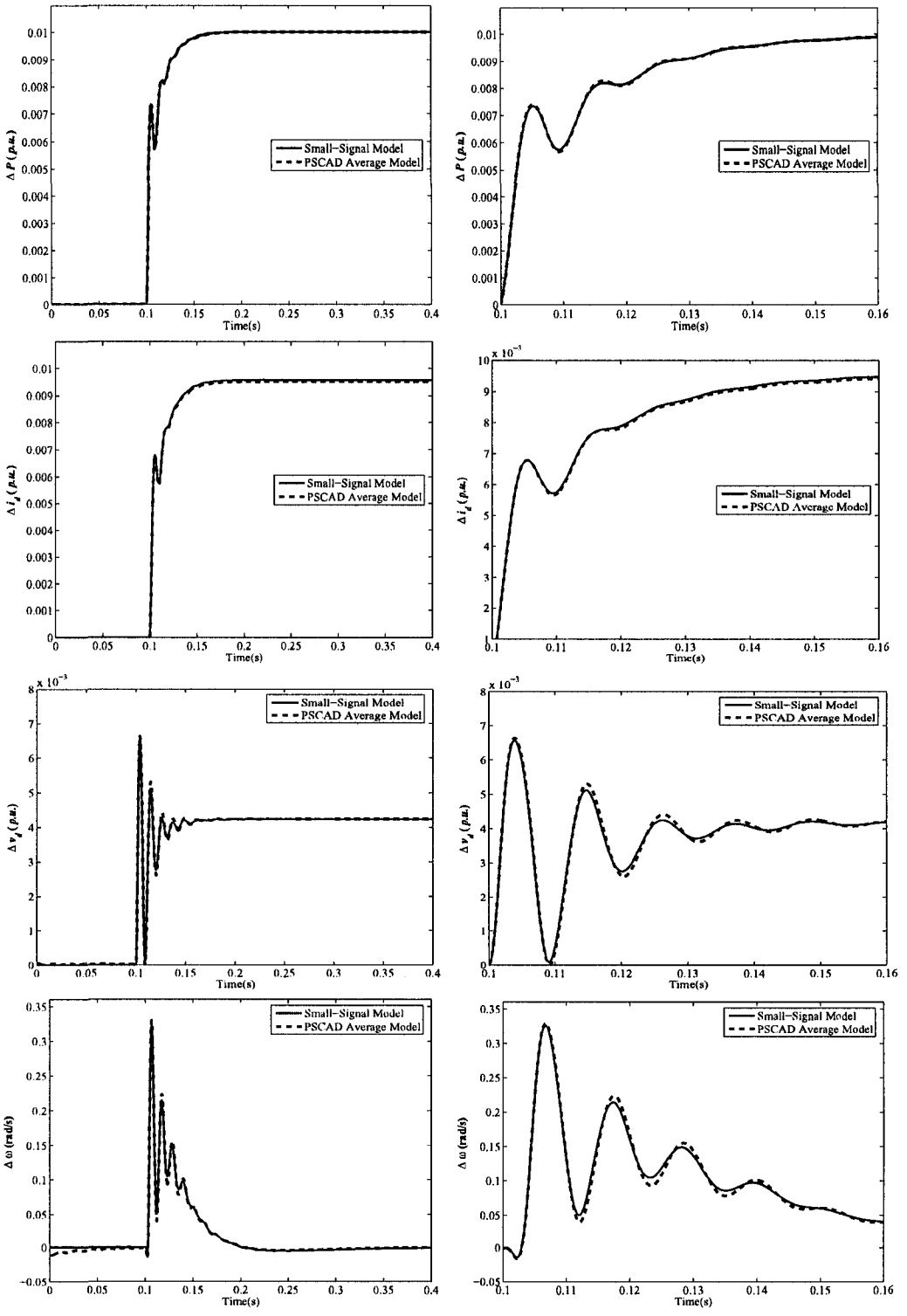

Figure 3.20: Small-signal model validation of the single DG system with *RLC* load - PSCAD inverter average model (left: variable responses, right: dislocation of the variable responses)

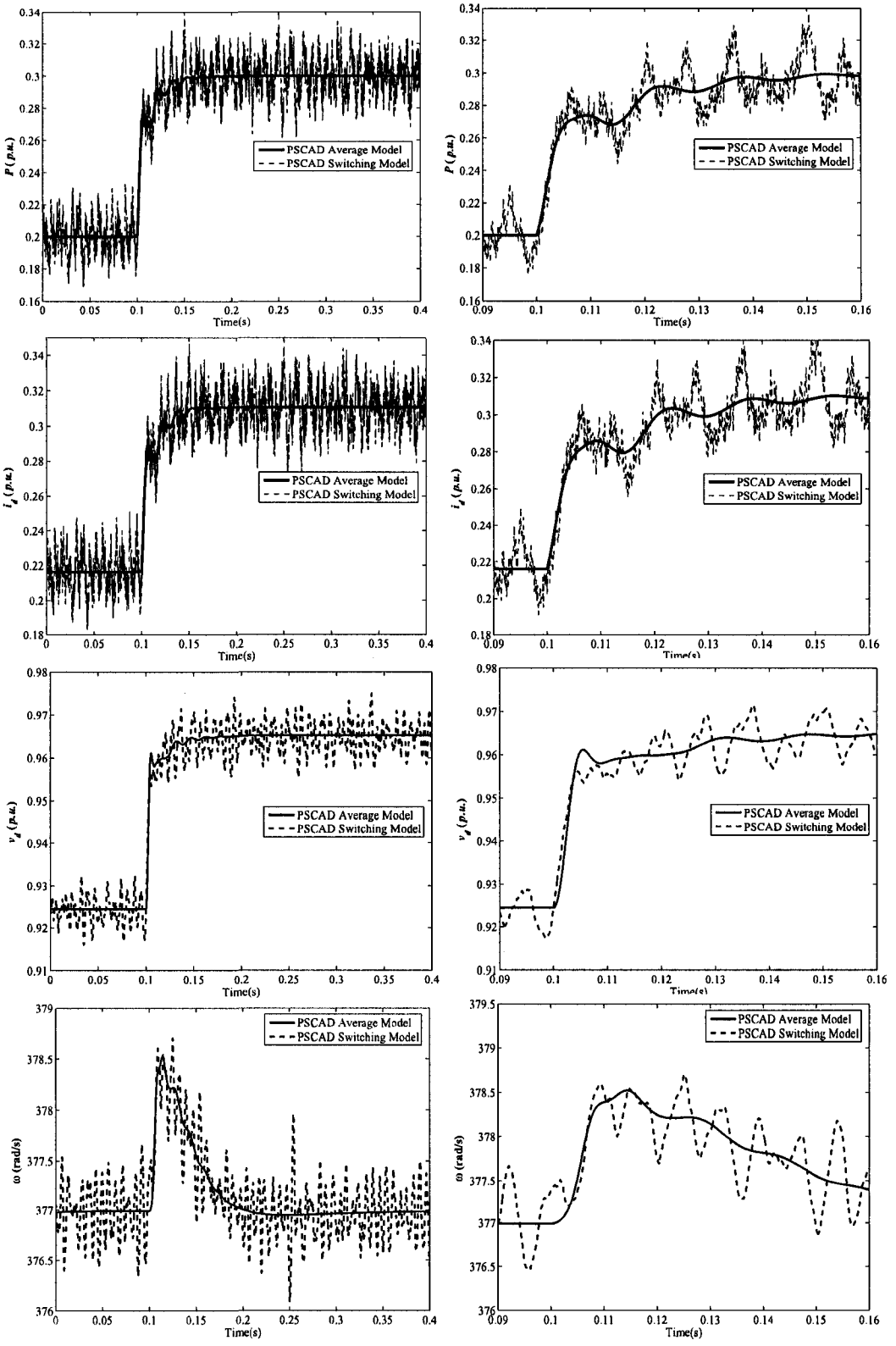

Figure 3.21: Small-signal model validation of the single DG system with *RLC* load - PSCAD inverter switching model (left: variable responses, right: dislocation of the variable responses)

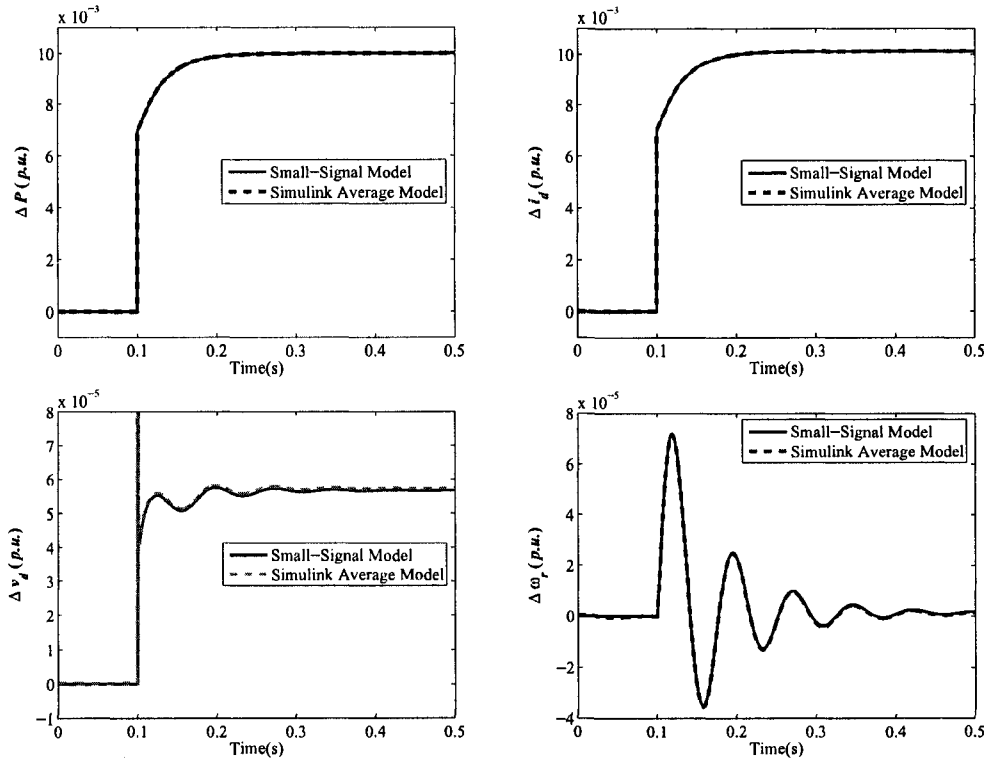

Figure 3.22: Small-signal model validation of the single DG system with motor load - Simulink inverter average model

3.4 Small-Signal Model of DG System with Multiple Inverters

Based on the small-signal model of single DG system, the analytical model of DG system with multiple inverters was developed to the study the impact of multiple inverter-based DGs on power distribution systems.

3.4.1 Model Development

The model structure of the multi-DG system is shown in Figure 3.23, where n is the number of DGs and m is the number of loads. The model structure is composed of the DG block, the network and loads block and the interface block. In the DG block each inverter-based distributed generator model is expressed in its own dq reference frame [76] where the DG terminal voltage phase angle is set as zero. The developed

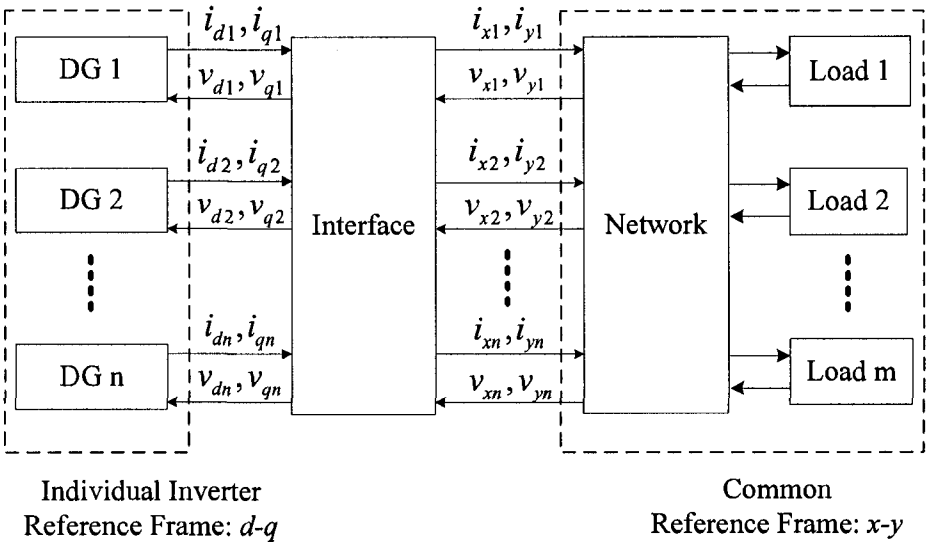

Figure 3.23: Structure of the multiple DG units system model

small-signal is shown in Appendix D.

3.4.2 Model Validation

Studies were conducted to validate and justified the developed small-signal model of multi-DG system. In order to carry out these studies, the Canadian urban benchmark distribution system proposed in [77] was utilized for analysis purposes of the modeling of multiple DG units. The schematic diagram of the test system is shown in Figure 3.24. The data of the feeder and the distribution transformers can be seen from Table E.3 in Appendix E. The utility source is at the $120kV$ level and the $12.5kV$ substation is connected to the grid through a circuit breaker (CB1) and a substation transformer with the capacity of $10MVA$. A $2.75MVar$ capacitor bank is located at the substation. Four inverter-based DGs (three-phase 208V) are evenly distributed along the feeder. They are connected to the feeder through the down-step transformers ($2MVA$) and the DG terminals are from Node **6** to Node **9** in sequence. The constant impedance load with the power factor 0.95 is represented as the local load of each generator. The inverters are constant power-controlled and all of them are equipped with the SFS anti-islanding control. The analytical model is verified from the following perspectives.

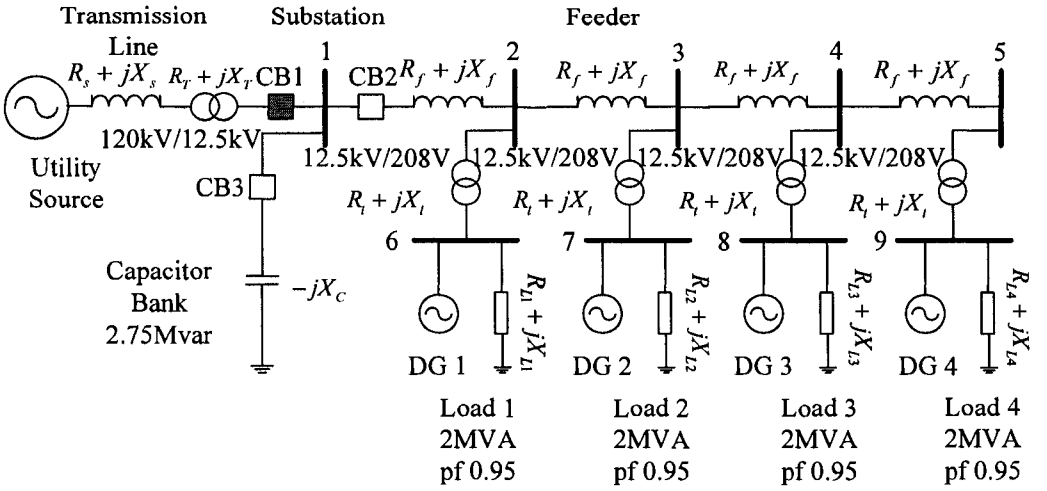

Figure 3.24: Schematic diagram of the test distribution system feeder with multiple inverter-based DG units

- Dynamic Response for a Reference Step

Figure 3.25 presents the dynamic behavior of the active power injected by $DG1$ when its reference power P_{ref1} is stepped from $0.1p.u.$ to $0.11p.u.$ at $t = 0.75s$.The local loads of the DGs are all with the capacity of $2MVA$ and the power factor of 0.95. The $DG1$ reactive power Q_{ref1} is kept as zero. The active power and the reactive power references for the other DGs are $0.1p.u$ and $0p.u.$, respectively. The verification result shows that the output power response of the developed small-signal model is very close to the result from the electromagnetic transients simulation in Matlab/Simulink. Different system parameters and input references were tested for all the DGs. The comparison results, which are not shown here, also indicate the same phenomenon.

- Stability Limit

In this section, the small-disturbance stability limit obtained by using the modal analysis and the small-signal model is compared with the stability limit obtained by using the electromagnetic transients-typed model. The system parameters are shown in Table E.3. The real power reference vector $\mathbf{P}_{ref} = [P_{ref1}, P_{ref2}, P_{ref3}, P_{ref4}]^T$ is gradually increased from $[0.2, 0.2, 0.2, 0.2]^T p.u.$ to $[0.45, 0.45, 0.45, 0.45]^T p.u.$ to

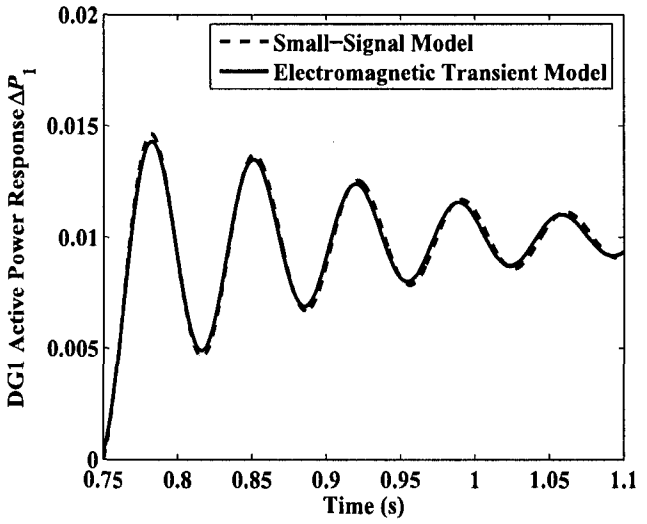

Figure 3.25: Model verification: DG1 active power response for a reference step - time domain response

observe the root loci of the small-signal model. The step of the change is the same for each DG unit. The reactive power reference vector $\mathbf{Q}_{ref} = [Q_{ref1}, Q_{ref2}, Q_{ref3}, Q_{ref4}]^T$ is set as zero.

Figure 3.26 displays the root loci of the multi-DG system when the vector $\mathbf{P}_{ref}$ is varied. One can see that a pair of conjugate eigenvalues moves from the left half-plane to the right half-plane when $\mathbf{P}_{ref}$ is increased. It is known that the DG system will lose its small-signal stability once there are eigenvalues with positive real parts. As a result, at this point there is a value of $\mathbf{P}_{ref}$ related to the system stability limit. The eigenvalue analysis of the developed small-signal model indicates that the stability limit of the DG system $\mathbf{P}_{ref}$ is equal to $[0.45, 0.45, 0.45, 0.45]^T p.u.$. Figure 3.26 also shows the stability limit obtained by the time domain model. The vector $\mathbf{P}_{ref}$ is stepped from $[0.2, 0.2, 0.2, 0.2]^T p.u.$ to $[0.4, 0.4, 0.4, 0.4]^T p.u$ at $t = 1.5s$. After this instant, the $DG1$ output power P_1 begins to oscillate and after a decaying time, the DG reaches a new steady-state operating point. The power reference $\mathbf{P}_{ref}$ is then stepped from $[0.4, 0.4, 0.4, 0.4]^T p.u.$ to $[0.45, 0.45, 0.45, 0.45]^T p.u.$ at $t = 5s$ and the DG system begins to oscillate at this power level and becomes unstable, which meets

the limit obtained by modal analysis.

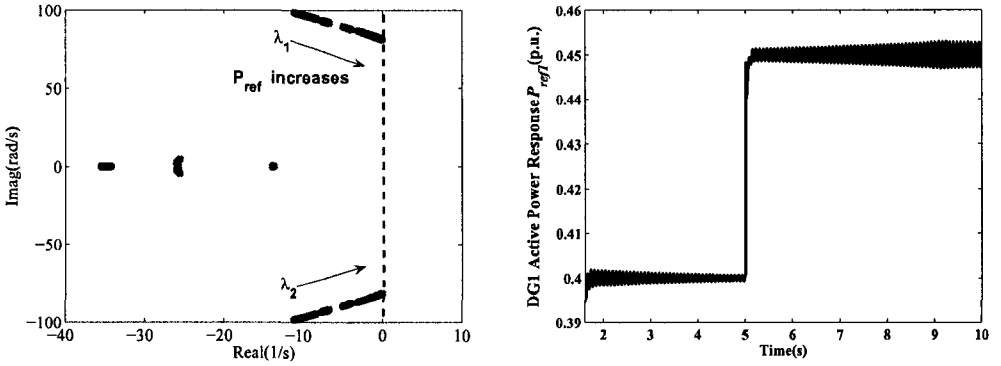

(a) Root loci of the multi-DG system (b) DG1 active power response - stability limit

Figure 3.26: Multi-DG system model verification

- Impact of Network Dynamics

When analyzing the stability and dynamic of inverter-based DG systems, it has been claimed that the dynamics of the network should be included in the analytical studies [78] as inverters do not have a large inertia constant like rotational generators and, consequently, the dynamics of inverter-based DGs are comparative to those of the network. In the multi-DG system small-signal model developed here, the dynamics of the network is neglected. This reduces the complexity of the system model. However, the accuracy of the simplified model must be verified. In order to validate the assumption that omitting the network dynamics will not cause significant error in the small-signal stability analysis, two more models are developed and analyzed. One is the electromagnetic transient model of the multi-DG system set up in Matlab/Simulink. And, the other is the detailed system small-signal model, which uses the derivative equations to express the network inductor and capacitor components.

Figure 3.27 shows the dynamic responses of the three models for an active power reference step at the site of DG1. Small-signal model I represents the simplified analytical model, which does not include the network dynamic, and small-signal model

II is the detailed model, which includes the network dynamic. The system parameters are as shown in Table E.3. It is seen that the curves of the three models match very well. This demonstrates the correctness of the detailed small-signal model and proves the simplified small-signal model is accurate enough for the multi-DG system stability studies.

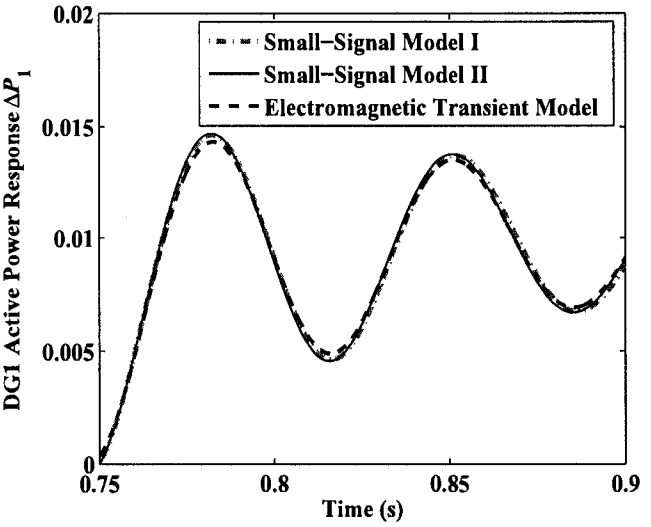

Figure 3.27: Impact of network dynamics on the multi-DG system

A further comparison can be seen from Figure 3.28 and Figure 3.29. Figure 3.28(a) shows root loci of the detailed small-signal model eigenvalues. Figure 3.28(b) shows a zoom of the eigenvalues dislocation in the rectangle of Figure 3.28(a). Figure 3.29 displays the root loci of the simplified small-signal model eigenvalues. It is not difficult to see that Figure 3.28(b) and Figure 3.29 have almost the same critical eigenvalues. That is to say, the eigenvalues in the ellipses of Figure 3.28(a) are introduced by the network dynamics. These eigenvalues are far way from the origin or have very high frequencies in the left hand plane. They will not have a great impact on the DG stability within the concerned frequency range. Thus, it is reasonable to neglect them.

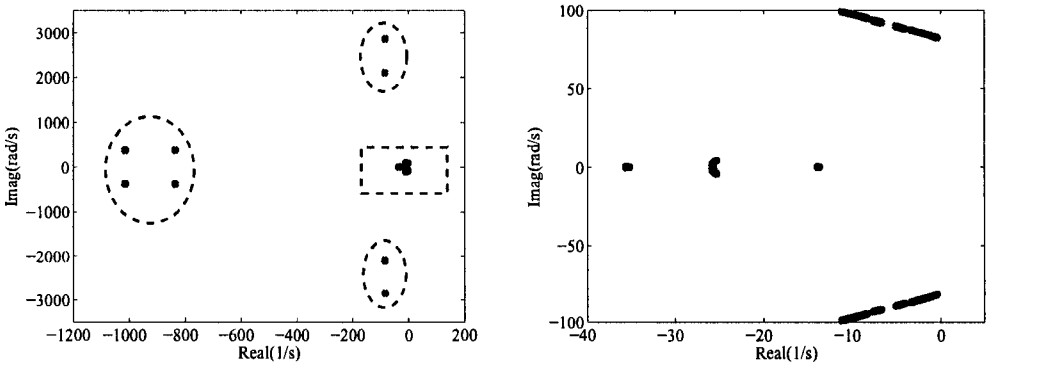

(a) All of the system eigenvalues

(b) Dislocation of the eigenvalues encircled in the rectangle

Figure 3.28: Root loci of the detailed multi-DG system small-signal model

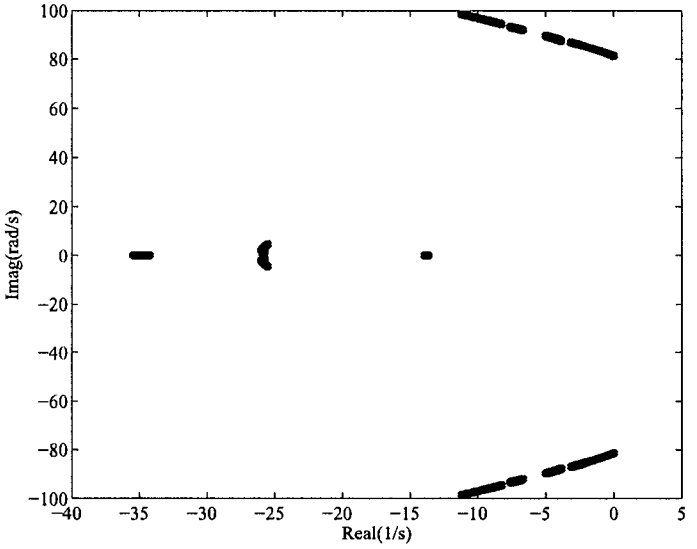

Figure 3.29: Root loci of the simplified multi-DG system small-signal model

3.5 Summary

This chapter presents the modeling of the grid-connected inverters and positive feedback anti-islanding controls. The small-signal models of single DG and multi-DG systems are developed. The SFS method is selected as the representative anti-islanding scheme for the analysis and it is extended from single-phase systems to three-phase systems. An extensive comparison between the small-signal model responses and the simulation results of the electromagnetic transient-type models shows that the small-signal models predicted the performance of the electromagnetic transient-type models with good accuracy.

The impact of the network dynamics on the accuracy of the DG system small-signal model is also investigated by the simulations and the modal analysis. It is found that the dynamics of the network inductor and capacitor components can be neglected in the small-signal stability analysis of the multiple inverter-based DG system in power distribution systems.

The modeling work in this chapter provides powerful tools for stability analysis of the impact of positive feedback anti-islanding controls on DG systems with static and dynamic loads. Also, the interactions between the inverter interface controls and the anti-islanding controls can be studied based on the small-signal models. In addition, the NDZ of the positive feedback anti-islanding scheme can be explored from the stability perspective. This work is discussed in the following chapters.

Chapter 4

Impact of Positive Feedback Anti-Islanding Scheme on Single DG System

With the inverter and anti-islanding scheme models presented in the previous chapter it is feasible to study the impact of inverter-based grid-connected DG on the supply power system analytically. This chapter focuses on the impact of the positive feedback anti-islanding scheme on the small-signal stability of a single DG system. SFS is selected as the representative positive feedback anti-islanding method in the studies. The key factors that can affect the DG system stability are discussed.

4.1 DG Power Transfer Capability

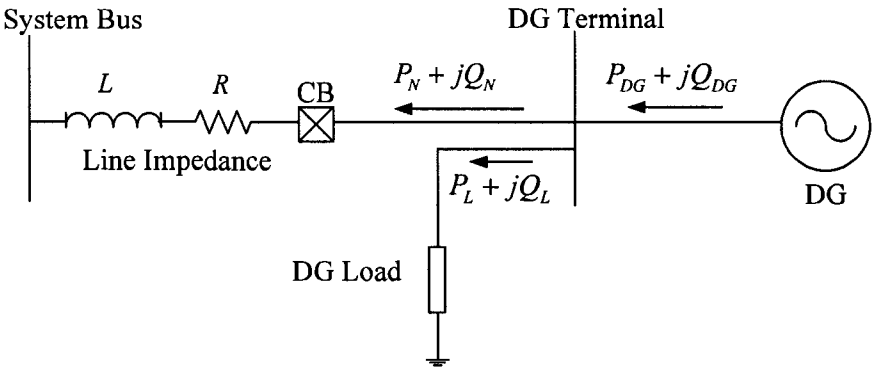

Figure 4.1: Single-line diagram of single DG system

The concept of the DG power transfer capability is first introduced in this section before the investigation of the impact of the positive feedback anti-islanding scheme is conducted. In Figure 2.1 a single DG system is illustrated to explain the phenomenon of DG islanding. The figure is reproduced here as Figure 4.1 for a better understanding of this section. For the system, if the DG output power P_{DG} is higher than the local load level P_L, the extra power generated by the DG will be delivered to the power system. It is well known that this extra power P_N has a limit because of the restriction of the power transfer limit by the line. When the limit is reached, the voltage of the DG terminal will collapse. This is the basis of the $P-V$ curve at the DG terminal. Similarly, if the load consumes more power than the DG produces, the deficit of power will be supplied by the grid. The network has also a maximum power transfer limit from the grid to the load. Consequently, there is also a $P-V$ curve that can be drawn for this case. Figure 4.2 combines the $P-V$ curves of the two previous possibilities into one. The positive direction of the power flow is defined as from the DG side to the power system side. Negative power means that the power system transfers power to the DG side or the load.

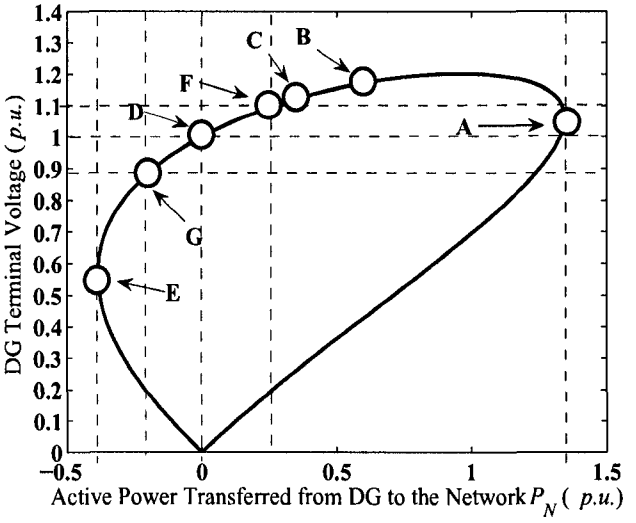

Figure 4.2: $P-V$ curve of the DG terminal (Q_N=0)

The value of P_N at point **A** is the active power transfer limit from the DG to

the power system and point **E** is related to the active power transfer limit from the network to the DG side. These limits were calculated considering the DG as an ideal voltage source and using the system steady-state power flow equations which do not include the effect of the DG control and anti-islanding scheme. In the calculations, the DG output reactive power Q_{DG} was set as zero due to the usual requirement of unity power factor operation. As a result, the reactive power consumed by the load was supplied by the network. If the load is the parallel RLC load it is resonant at the system base frequency ($f_0 = 60Hz$), which is the worst case for the anti-islanding detection [5], the reactive power Q_N and Q_L are zero. In this situation, the real power P_L does not affect the calculation results since the real power P_N is assumed constant and the change of the load active power will be balanced by the DG power output.

The previous analysis was conducted without taking into consideration the DG controllers and the anti-islanding schemes. However, if a typical inverter controller is considered, for the case of positive P_N, the maximum active power that the DG can transfer to the system without becoming unstable is represented by point **B** in Figure 4.2. In this case, the power transfer limit from the DG to the network is much smaller than the limit at point **A**. In addition, if a typical positive feedback-based anti-islanding scheme is considered, the maximum power transfer is represented by point **C**. For this situation, the variation of the positive feedback gain may adversely affect the DG power transfer limit. Thus, the impact of positive feedback anti-islanding scheme on the DG system steady-state stability can be reflected by the maximum power transfer limit. This limit can be used as a stability index to measure the DG system stability margin. In this thesis, the maximum power that can be delivered from the DG to the network is defined as the DG power transfer limit P_{max}. The section of the $P-V$ curve between point **F** and point **G** is the practical DG operation region which is limited by the DG terminal voltage range defined in [4].

On the other hand, if the DG load absorbs (inductive load) or supplies (capacitive load) reactive power, the DG terminal $P-V$ curve will shrink or expand. Figure 4.3 shows three $P-V$ curves for different Q_N settings. When the value of Q_N is negative,

the load is inductive and when the value of Q_N is positive, the load is capacitive.

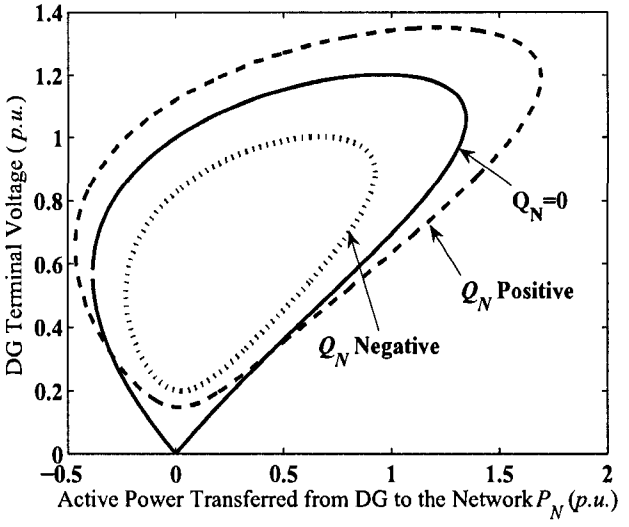

Figure 4.3: $P - V$ curve of the DG terminal for different Q_N

For the case of P_N negative, the destabilizing effect of the inverter anti-islanding control on the DG system could be diluted by the network due to the increase of the network power contribution to the load. However, the network contribution is not unlimited and the distribution line confines it to point **E** (in Figure 4.2) where the power transfer limit is defined as P_{min}.

4.2 Analysis of Single DG System with Parallel RLC Load

Based on the proposed DG system small-signal stability index - DG power transfer capability, the relationship between the DG system stability and the positive feedback anti-islanding control can be determined quantitatively.

4.2.1 Key Factors Affecting the DG System Small-Signal Stability

A sensitivity analysis was conducted to understand parametric influences of the SFS method on the dynamic performance of the DG system with constant-power

controlled inverter. The study is based on the eigenvalue analysis of the single DG system small-signal model. Four factors were investigated in this section, which are the positive feedback gain, the initial chopping fraction, the load power level and the distribution line impedance. In addition, the maximum power transfer limit versus positive feedback gain curve ($P - K$ curve) is proposed as a tool to investigate and understand the system stability in the presence of inverter-based generator equipped with positive feedback anti-islanding scheme. The system parameters for the base case are presented in Table E.1 of Appendix E.

- Positive Feedback Gain

First, the positive feedback gain of SFS is varied while the other parameters are kept constant to observe the change of the system stability. The *RLC* load does not consume or supply reactive power in this analysis. It was mentioned in previous section that the DG power transfer limit to the network is selected as the stability index. This stability index can be determined by using modal analysis as follows.

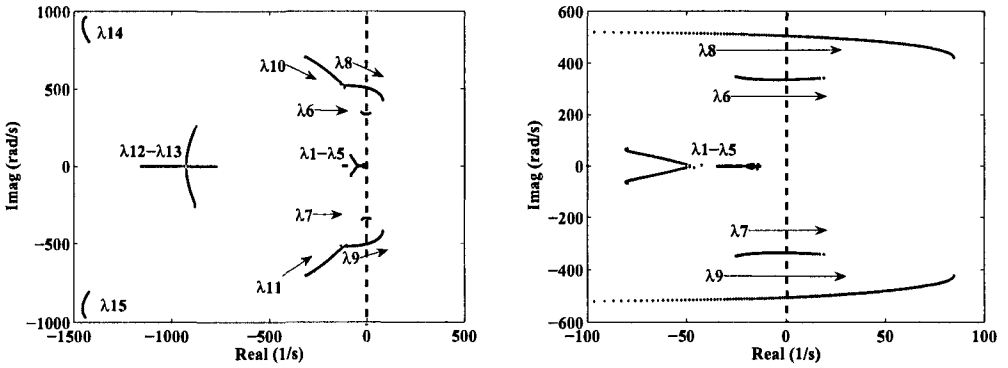

(a) Root loci of all the eigenvalues (b) Dislocation of the critical eigenvalues

Figure 4.4: Root loci of the single DG system eigenvalues

Figure 4.4(a) shows the root loci of the system eigenvalues when K_f is 0.0032 and P_N is gradually varied from $-0.385p.u.$ to $1.345p.u.$. Figure 4.4(b) reveals that two pairs of conjugate eigenvalues (λ_6, λ_7 and λ_8, λ_9) move from the left half-plane to the right half-plane when P_N is increased. The dominant eigenvalues λ_8 and

λ_9 cross the imaginary axis when P_N is increased to 0.153 *p.u.*, which is the DG power transfer limit for K_f=0.0032. Accordingly, for each positive feedback gain, a DG power transfer limit can be obtained by the eigenvalue analysis. By using this approach, Figure 4.5 is plotted to show how the limit changes with the tuning of K_f. In Figure 4.5, K_f is varied from 0 to 0.03, and a $P-K$ curve (i.e., the DG power transfer limit versus the positive feedback gain curve) is drawn. The $P-K$ curve shows that when the positive feedback gain is low, the DG can transfer more power to the grid. However, this limit is reduced when K_f increases. In addition, this limit is negative for high K_f values, which means that some part of the power consumed by the load must be provided by the network if the positive feedback is relatively strong. In this case, the power contribution to the load from the DG must be decreased. Figure 4.5 also shows that P_{min} will be reached when K_f is raised further and over some value. In this situation, the DG system cannot be stable at any operating point.

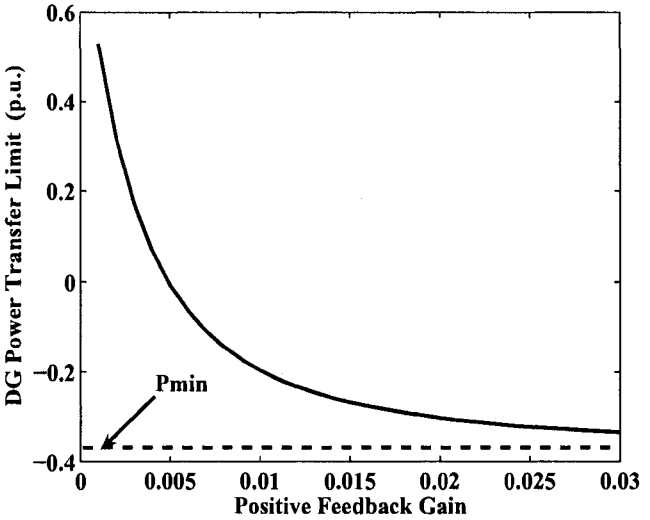

Figure 4.5: $P-K$ curve of the DG power transfer characteristic

In summary, the positive feedback gain has a negative impact on the DG system stability. The higher the positive feedback gain, the lower the power transfer limit.

- Initial Chopping Fraction

In the case of constant current-controlled inverters, a nonzero cf_0 will make the steady-state frequency of the islanding system different from the power system base frequency even when the RLC load is resonant at ω_0 [40]. In addition, a large cf_0 enables the SFS method to be more effective for anti-islanding detection. However, for constant power control inverters, the simulation results show that such effect of cf_0 is counteracted by the power controllers. In addition, the eigenvalue analysis results indicate that the DG system stability is not sensitive to cf_0. Figure 4.6 shows four $P - K$ curves for different cf_0. All other system parameters are the same as those used to obtain Figure 4.5. It can be seen that there is no observable differences among the four curves. Thus, the variation of cf_0 has almost no impact on the $P - K$ curve.

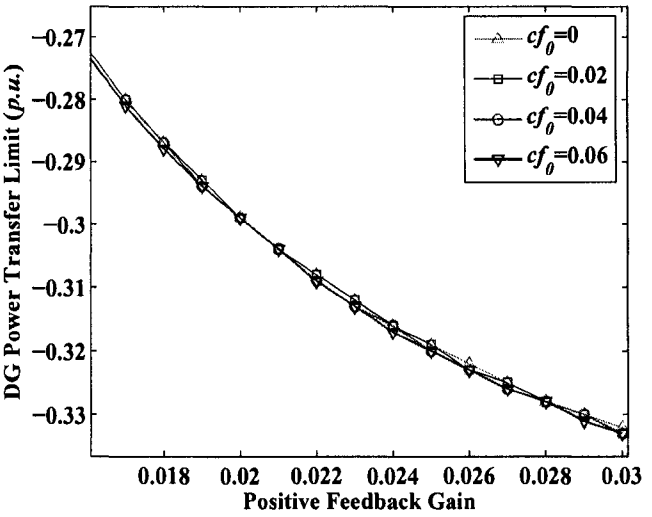

Figure 4.6: $P - K$ curves for different cf_0

- Load Level

The effect of the local load power level on the DG system stability is studied in this section. First, the resistance of the parallel RLC load is changed to represent the variation of the active power consumed by the local load. The load inductance and the capacitance are set equal to the values presented in Table E.1 and they are

kept constant. Thus, the load reactive power demand is zero. Figure 4.7 displays four $P-K$ curves for different R_L values. These curves show that the larger the R_L is (i.e., the lower the load power level), the higher the P_{max} is for same K_f setting. This result means that when the R_L value is increased, the DG can transfer more power to the network since the requirement from the load is decreased. In addition, if the power delivered from the DG to the network is the same, a stronger positive feedback can be used for a lower load since the same power transfer limit is obtained.

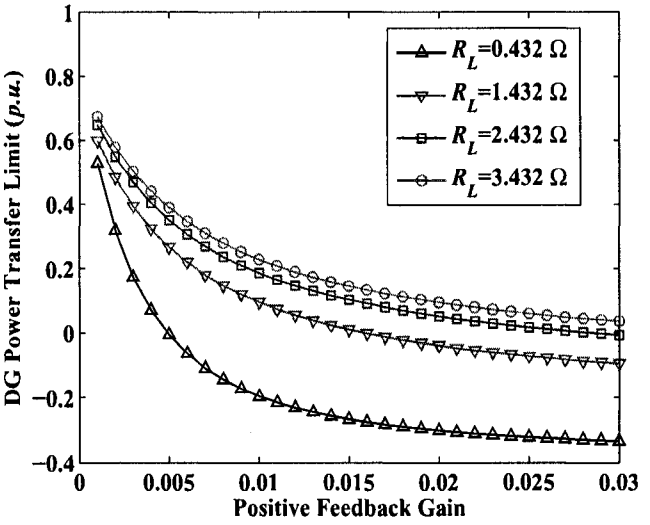

Figure 4.7: $P-K$ curves for different R_L

However, the phenomenon is different if it is analyzed from the inverter-based generator perspective. In Figure 4.8, the maximum DG output power versus positive feedback gain curves are plotted for different R_L values. This figure reveals that when R_L is larger, the maximum inverter output power will be lower, although the DG power transfer limit to the network will be higher. This result occurs because the active power flow among the DG, the load and the network has the relationship expressed by:

$$P_{DG} = P_N + V_{DG}^2/R_L \tag{4.1}$$

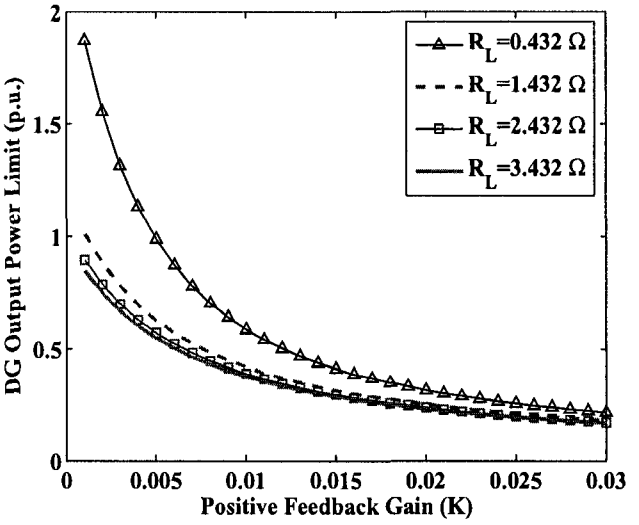

Figure 4.8: Maximum DG output power for different R_L

If R_L is smaller, the active power consumed by the load will be relatively higher when the system stability limit is reached. Thus, the DG must supply more power to satisfy this requirement. As a result, the DG output power limit is higher for the smaller R_L case. The sensitivity of the $P - K$ curve to changes in the RLC load inductance and the capacitance is shown in Figure 4.9. The RLC load is represented in the quality factor (Q_f) - resonant frequency (f_c) space [70]. The resistance of the load R_L is kept as 0.432Ω. L_L and C_L are changed so that f_c is held at 60Hz, and Q_f is varied from 0.18 to 0.58. The comparison results show that when the resistance is the same, a RLC load with a higher quality factor will lead to a larger stability margin for the DG system with the positive feedback anti-islanding control.

- Distribution Line Impedance

The distribution system line impedance is also an important factor in the stability analysis, since this impedance reflects the short-circuit level at the interconnection point. If the power system is weak or the line impedance is relatively large, the power stability limit is low. In addition, a strong positive feedback anti-islanding control

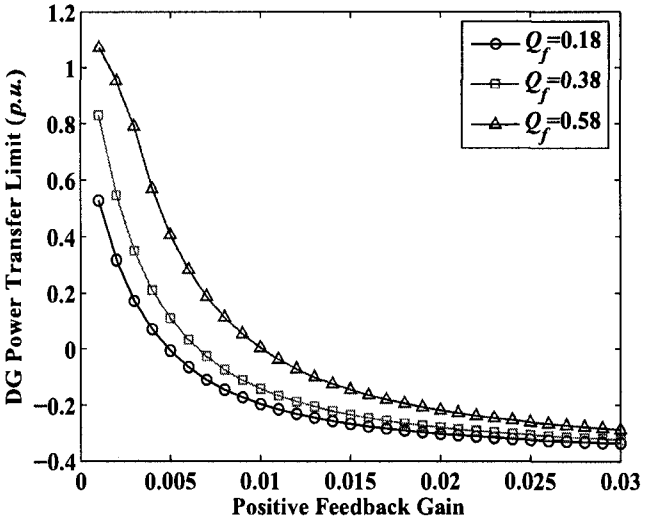

Figure 4.9: $P - K$ curves for different Q_f

will boost this trend even more.

The sensitivity analysis of the impact of the distribution line on the DG system stability is investigated by changing the line impedances as shown in Table 4.1. Z is the magnitude of the impedance, and the X/R ratio is kept constant in 0.5 for all the cases. The other parameter settings are the same as those presented in Table E.1. Figure 4.10 shows the $P - K$ curves for different distribution line impedances. This figure reveals that when the line impedance is larger, the DG power transfer limit is reduced. This observation accords with the conclusion that a weak power system, which presents a high line impedance and, consequently, a low short-circuit level, has a small stability margin. Therefore, the DG system is prone to be destabilized by the strong positive feedback anti-islanding control if it is connected to a weak power system.

Another situation is studied by considering line impedance variations. In this case, Z is kept constant at 0.2Ω, and the X/R ratio is changed. The different R and X values are listed in Table 4.2. Figure 4.11 displays the results, revealing that a larger X/R leads to a small stability margin. In this case, since Z magnitude is kept

Table 4.1: Distribution Line Impedance Parameters ($X/R = 0.5$)

$Z(\Omega)$	$R(\Omega)$	$X(\Omega)$
0.08	0.0716	0.0358
0.1	0.0894	0.0447
0.15	0.1342	0.0671
0.2	0.1789	0.0894

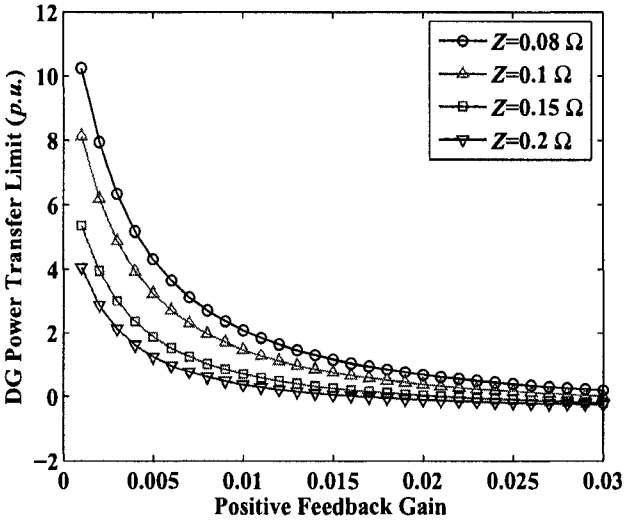

Figure 4.10: $P-K$ curves for different distribution line impedances (X/R is constant)

constant, X/R is augmented by increasing the X value and reducing the R value proportionally. Therefore, the reactive power consumed by the line increases, leading to a reduction in the steady-state stability margin.

Table 4.2: Distribution Line Impedance Parameters ($Z = 0.2\Omega$)

X/R	$R(\Omega)$	$X(\Omega)$
5	0.0392	0.1961
2	0.0894	0.1789
1	0.1414	0.1414
0.5	0.1789	0.0894

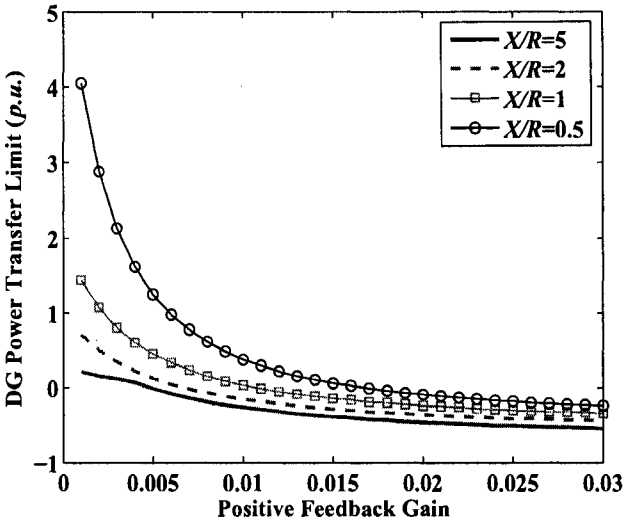

Figure 4.11: $P - K$ curves for different distribution line impedances (Z is constant)

4.2.2 Conflict between DG Power Transfer and Islanding Detection Capability

Based on the $P - K$ curve, the impact of the SFS method on the stability of the DG system can be explicitly quantified. From the sensitivity analysis results, it was verified that the positive feedback gain cannot be too large, or it will make the DG system unstable. However, it is well recognized that the gain also cannot be too small, or it will result in a large NDZ for the anti-islanding detection method [70], [79].

Figure 4.12 shows the dynamic behavior of the DG terminal voltage frequency for two different positive feedback gain settings. The results were obtained from electromagnetic transient simulations by using the model set up in Matlab/Simulink. The RLC load for the two cases has the resonant frequency of $60.2Hz$ and the quality factor of 1.8. The load resistance is 4.32Ω, and the inverter output active power reference is $0.1p.u.$. The anti-islanding control is enabled at $0.2s$, and the circuit breaker in Figure 4.1 is opened at $0.6s$, causing an islanding situation. Figure 4.12 indicates that when the gain K_f is small (0.01), the frequency of the DG system goes to another stable state after the islanding occurrence. In this case, the under or

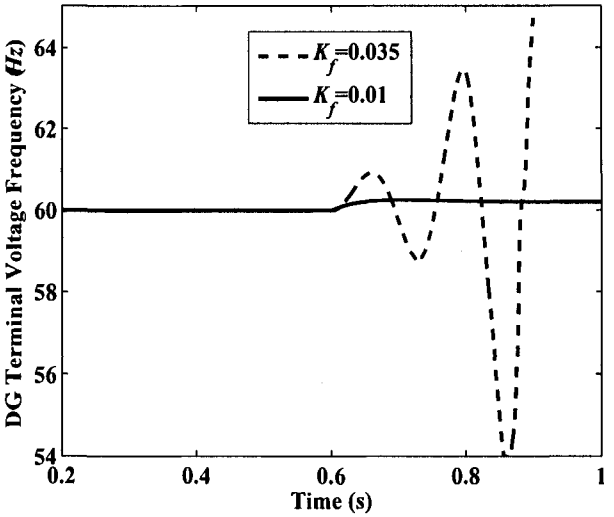

Figure 4.12: Frequency variations of the islanded DG system

the over frequency relay cannot detect the islanding situation because the new stable frequency is within the typical non-detection range of the relay ($59.3Hz - 60.5Hz$ as recommended by [5]. On the other hand, for the large K_f (0.035), the islanded DG system is destabilized by the strong positive feedback and the system frequency moves outside the frequency relay limits in a short time, permitting the relay to detect the islanding situation quickly.

The improvement of the anti-islanding method efficiency by increasing the gain K_f, however, is at the expense of the DG system stability margin reduction. At the high K_f setting, the DG system loses its stability if the load or the network condition is changed even without an islanding occurrence. Figure 4.13 shows the dynamic behavior of the frequency of the grid-connected DG system. The difference between this case and the large K case in Figure 4.12 is that the resistance of the *RLC* load in this case is 5.32Ω, and no islanding is simulated. The DG system frequency begins to oscillate when the DG is connected to the network, and the anti-islanding control is enabled at $0.2s$. Obviously, $K_f = 0.035$ is not suitable for this case.

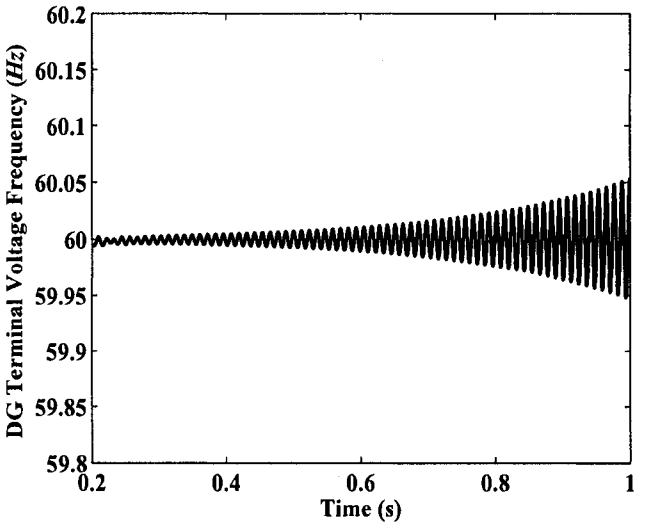

Figure 4.13: Frequency behavior of the grid-connected DG system

The analytical model of the DG system provides a tool for the anti-islanding control design as a trade-off between the islanding detection capability and the stability limit. Based on the analytical model, a reasonable system stability margin and anti-islanding detection performance can be achieved by tuning the positive feedback parameters taking into consideration the actual network and load conditions, the different types of inverter controls (constant power control, constant current control), and the detection time requirement. To carry out this procedure, the thesis proposed the usage of the DG power transfer limit versus islanding detection time ($P-t$) curve. The idea is to obtain the power transfer limit versus positive feedback gain ($P-K$) curve for the system to be designed. The results show that the higher the feedback gain is, the lower the power limit is. Therefore, the islanding detection time versus positive feedback gain ($t-K$) curve can be obtained to the same system by repeated electromagnetic transient simulations. According to the operation theory of the anti-islanding scheme, the higher the positive feedback is, the faster the islanding detection time is. The $P-t$ curve is obtained by combing the $P-K$ curve and the $t-K$ curve with the positive feedback K_f as the intermediate variable. Figure 4.14 shows a $P-t$ curve for the anti-islanding control parameter design. The system parameters are those presented

in Table E.1. The resistance of the parallel RLC load is 4.32Ω. In addition, the DG output power is $0.1p.u.$. As a result, P_N is zero in Figure 4.1. This level of $P_N$is the worst condition for islanding detection. The resonant frequency of the load is $60.7Hz$, and the quality factor is 1.8. The gain K_f varied from 0.001 to 0.03.

The $P-t$ curve in Figure 4.14 reveals that the higher the islanding detection time requirement is, the higher the DG power transfer limit is. A well-designed DG system should have a high power transfer limit and fast islanding detection. Based on this type of curve, a DG owner can determine the DG power transfer limit or the DG system stability margin based on the islanding detection time requirement adopted by the utility.

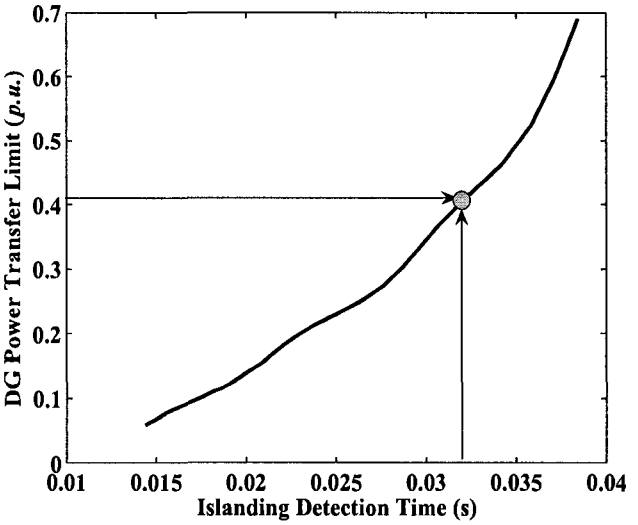

Figure 4.14: $P-t$ curve for the anti-islanding control parameter design

4.2.3 Interaction between Inverter Interface Controls and Anti-Islanding Control

In inverter-based DG applications, different inverter interface control strategies may have distinctive impact on the DG operation when it is operated in grid parallel mode [80] - [81]. The impact will be more complex if the positive feedback anti-

islanding methods are embedded in DG. Positive feedback anti-islanding control is resident in the inverter and it will inevitably interact with the main inverter interface controls such as the constant power control and the constant current control. This section investigated the characteristics of such interactions from the stability perspective since the positive feedback anti-islanding control is a destabilizing force which has a negative impact on the stability of an interconnected DG system. The modal analysis of the test DG system is employed to study the different effects of the positive feedback control on the DG system small-signal stability when it works together with the constant power controller and the constant current controller.

Figure 4.15 displays the root loci of the constant power-controlled and the constant current-controlled DG systems when the positive feedback gain is changed in each system. The system parameters of the two systems are the same and they are shown in Table E.1. The output power reference ($P_{ref} + jQ_{ref}$) of the constant power-controlled inverter and the output current reference ($i_{dref} + ji_{qref}$) of the constant current-controlled inverter are all set as $0.1p.u.$. The chopping fraction cf_0 is zero for both systems. By this means, the two inverters output the same power as the DG terminal voltages will all be $1.0p.u.$ at the steady state when R_L is $4.32\Omega(10p.u.)$ and no reactive power is consumed by the LC load. The quality factor and the resonant frequency of the load are 1.8 and 60Hz, respectively. For this scenario, there is no power exchange between the network and the DG system. The RLC load is only supplied by the DG even the DG system is connected to the network at the PCC point.

From the structures of the constant power-controlled DG system and the constant current-controlled DG system shown in Figure 3.8 and Figure 3.9, one can see the constant power-controlled inverter has two more outer loop PI controllers than the constant current-controlled inverter. This means the small-signal model of the constant power-controlled DG system will have two more eigenvalues. From the modal analysis of the two DG systems, these two additional eigenvalues will affect the overall stability performance of the DG system. The root loci in Figure 4.15 show

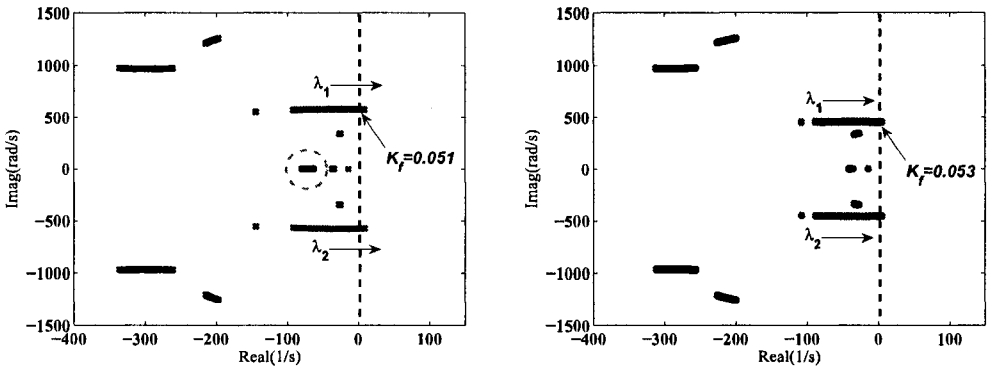

(a) Constant power-controlled DG system (b) Constant current-controlled DG system

Figure 4.15: Root loci of the inverter-based DG systems

that the constant power-controlled DG system loses its small-signal stability when K_f is increased to 0.051 while the corresponding instability point of the constant current-controlled DG system occurs when K_f is 0.053. The eigenvalues encapsulated in the circle in the left part of the figure are the extra eigenvalues due to the power controller.

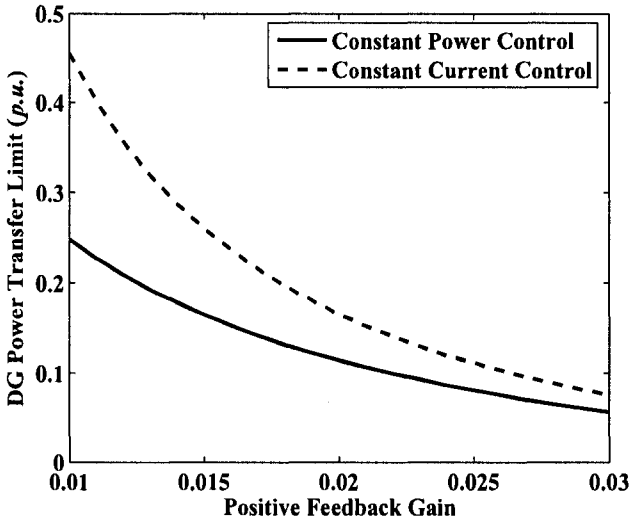

Figure 4.16: $P - K$ curves of the DG system with different interface controls(R_L=4.32Ω (10$p.u.$))

The phenomenon observed from Figure 4.15 indicates that the SFS control is prone

to destabilize the constant power-controlled DG system in this situation. Figure 4.16 displays the $P - K$ curves for the two DG systems. For this scenario, the DG output reactive power is zero since the inverter is usually required to be operated with unity power factor. For the constant current-controlled DG system, the DG output current limit is related to K_f directly and the P-K curve is acquired by converting the current limit to the corresponding power limit through the steady-state power flow calculations. This facilitates the comparison of the performance of the two inverter interface controllers.

It is noticed in Figure 4.16 that the constant power-controlled DG has a lower power transfer limit than the constant current-controlled DG, which means the former DG can transfer more power to the grid in this case. This conclusion accords with that from Figure 4.15.

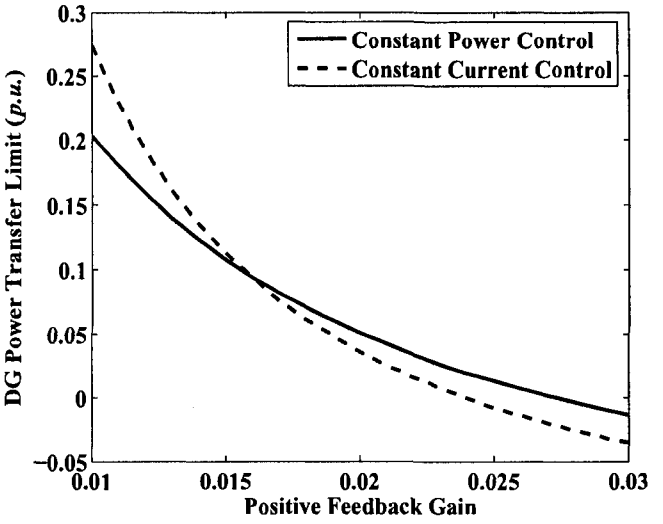

Figure 4.17: $P - K$ curves of the DG system with different interface controls(R_L=2.16Ω (5$p.u.$))

A different scenario is shown in Figure 4.17 where the resistance of the RLC load is 2.16Ω(5$p.u.$), which represents a relatively higher load level. The quality factor and the resonant frequency are not changed, which means the values of L_L and C_L will

change with the value of R_L. The other parameters of the DG system are the same with those in the previous scenario. It can be seen that when the positive feedback is weak the constant current-controlled DG still has a higher power transfer capability. However, the conclusion is reversed when K_f is increased. The constant power-controlled DG can produce more power with the strong positive feedback control. When the DG load level is raised further, the $P - K$ curves are shown in Figure 4.18 where R_L is set equal to $1.73\Omega(4p.u.)$. In this scenario, the constant power-controlled DG has higher power transfer capability or larger steady-state stability margin than the constant current-controlled DG. And the power transfer capability gap between the two DGs is enlarged when the positive feedback anti-islanding control is strengthened.

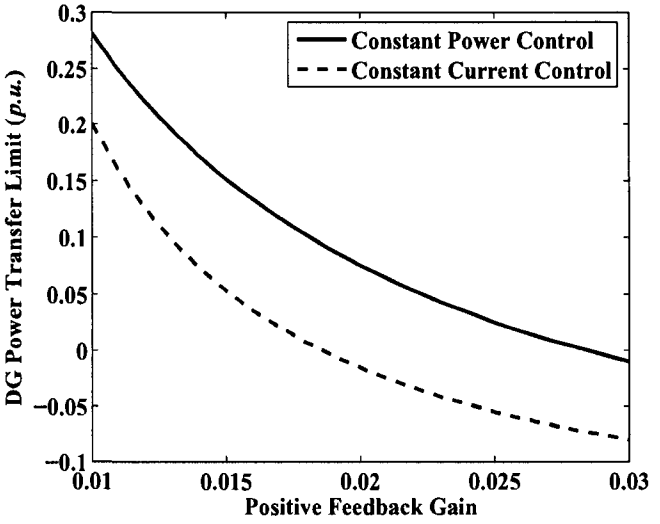

Figure 4.18: $P - K$ curves of the DG system with different interface controls(R_L=1.73Ω (4$p.u.$))

Thus, from the above three scenarios one can see that the inverter-based DG has different power transfer capability when the inverter interface controls are different. This power transfer capability will decrease with the increasing of the positive feedback gain of the anti-islanding control. In addition, the DG local load level also has the great effect on the DG power transfer limit.

The sensitivity of cf_0 on the $P-K$ curves for the two inverter controllers is also investigated. The results are shown in Figure 4.19. cf_0 is changed from 0 to 0.06 for each controller. It can be observed that the DG power transfer capability for both controllers is reduced when cf_0 is getting larger. Moreover, the $P-K$ curve change for the constant current-controlled DG is more sensitive to cf_0 variation in the DG system steady-state stability analysis.

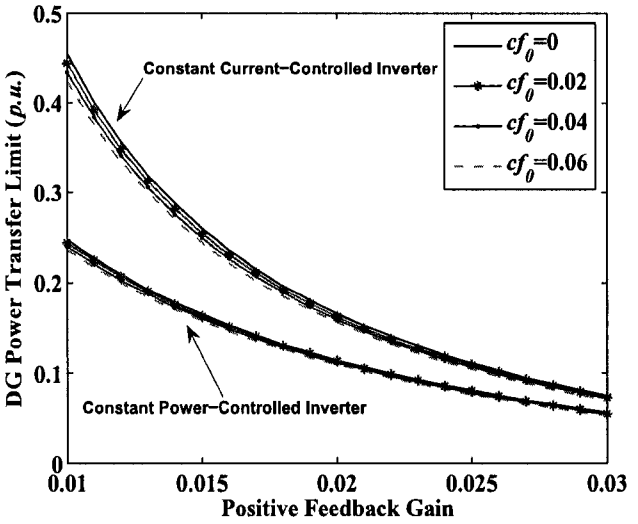

Figure 4.19: $P-K$ curves of the DG systems for different cf_0 (R_L=4.32Ω (10$p.u.$))

4.3 Analysis of Single DG System with Induction Motor Load

RLC load is constant impedance load and the load power changes dramatically with the load voltage. However, induction motor is close to the constant power load and its load active power does not change a lot when the voltage on the motor is altered. This section investigated the impact of the positive feedback anti-islanding control on the small-signal stability of the single DG system with induction motor load.

4.3.1 Operation Characteristics of DG System

An illustrated single DG system with induction motor load is shown in Figure 3.16. The system parameter settings are listed in Table E.2. In order to study the operation characteristics of the DG system in a weak power distribution system, the network line impedance is replaced with $R + jX = 0.2 + j0.3\Omega$. The motor has the constant mechanical torque $T_m = 0.373p.u.$ which is also the rated motor torque. Figure 4.20 shows the operation characteristics of the tested single DG system. As seen from the figure, the DG terminal voltage or the PCC voltage is increased when the DG outputs more power. However, the active power consumed on the motor does not change a lot with the increasing of the PCC voltage because of the motor constant mechanical torque. It decreases a little when the DG output power P_{ref} is raised greatly. The extra power delivered by the DG is transferred to the network. On the other hand, the reactive power consumed by the motor is getting bigger with the increasing of P_{ref}, which means the motor need more reactive power from the network at this time. The motor speed ω_r will increase according to the relationship between it and the electromagnetic torque T_e [76].

In Figure 4.20, point **A** is corresponding to the small-signal stability of the DG system without considering the positive feedback anti-islanding control in the DG inverter. point **B** and point **C** are for the cases of $K_f = 0.01$ and $K_f = 0.02$, respectively. cf_0 is zero for these cases. One can see the stronger the positive feedback gain is, the smaller the small-signal stability margin the system has. The figure also shows that the PCC voltage could be within the voltage limit range ($0.95p.u.$ $1.05p.u.$) when the positive feedback anti-islanding control begins to affect the DG system small-signal stability. This is because the high inductive load power will lower the PCC voltage while the high DG transfer active power will change the PCC voltage in a reverse way. The reactive power consumed by the motor is increased with the raising power transferred from the DG to the network. Thus, increasing of the the PCC voltage with the increasing of the DG transfer power is not as obvious as the that for the resonant RLC load.

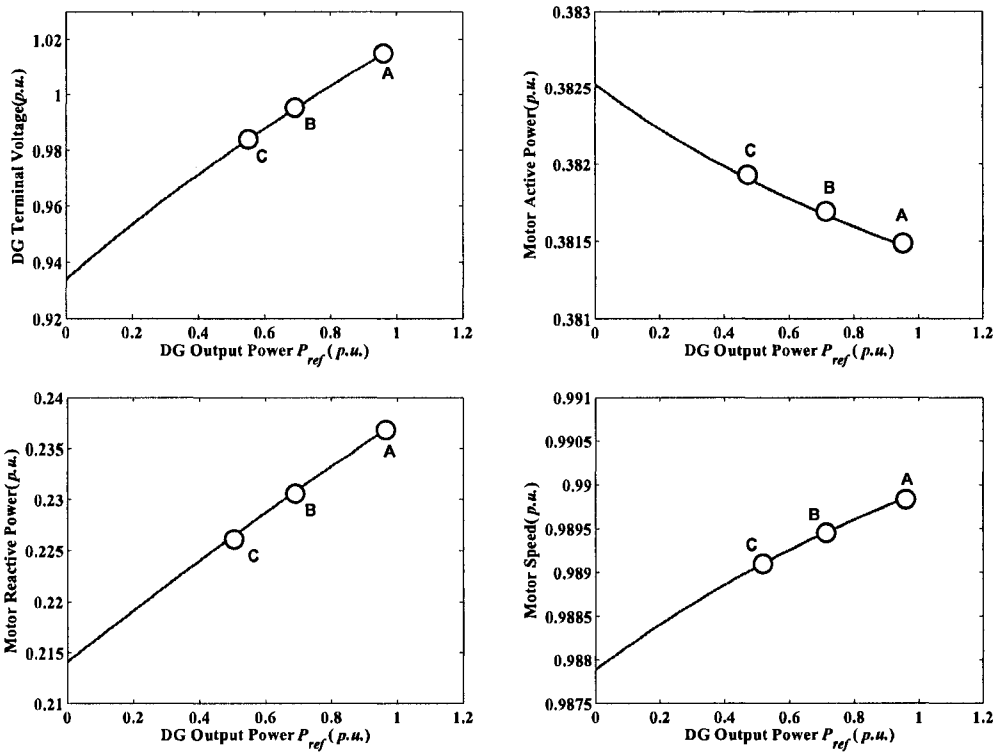

Figure 4.20: Operation characteristics of single DG system with induction motor load (Stability Limit - point **A**: K_f=0; point **B**: K_f=0.01; point **C**: K_f=0.02)

4.3.2 Key Factors Affecting the DG System Small-Signal Stability

The sensitivity analysis was conducted to investigate the key factors affecting the studied DG system small-signal stability. In this section, the parametric influences of the SFS control on the dynamic performance of the DG and the motor load are presented and discussed. The system parameter settings are listed in Table E.2 and the network line impedance is replaced with $R + jX = 0.2 + j0.3\Omega$. The inverter is constant-power controlled.

- Positive Feedback Gain

Figure 4.21 shows the $P - K$ curve of the single DG system with induction motor load. cf_0 is zero for the SFS control. The figure reveals that the DG power transfer

limit to the network reduces fast when the positive feedback control is small and the $P-K$ curve is becoming flat at the large K_f value. The negative value of the transfer limit means the DG can only output limited power and the extra power (negative DG power transfer limit) needed by the motor is supplied by the grid. Thus, if the positive feedback anti-islanding control is strong the inverter output power will be greatly restricted.

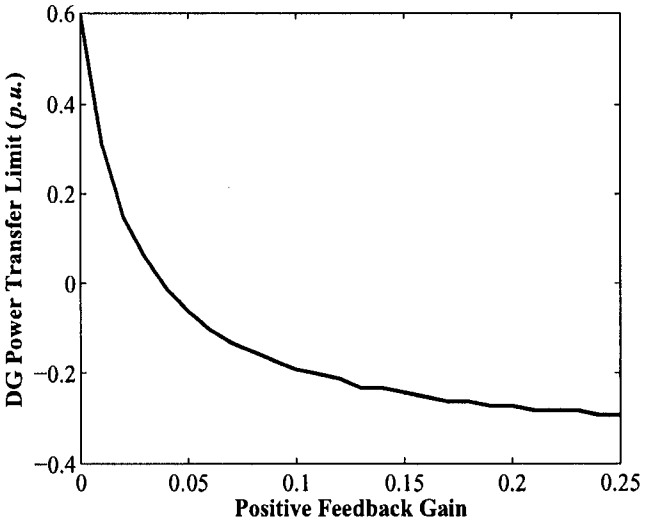

Figure 4.21: $P-K$ curve of the single DG system with induction motor load

- Motor Mechanical Torque

In many situations, the motor load will not be operated at the rated mechanical torque (T_b). The sensitivity of the DG system stability to the motor mechanical torque (T_m) is analyzed for the constant motor mechanical torque in Figure 4.22. The figure displays that the DG system will be more stable when T_m is lower. This phenomenon also indicates that large size motor will have relatively strong interaction with the positive feedback anti-islanding control.

- Motor Inertia Constant

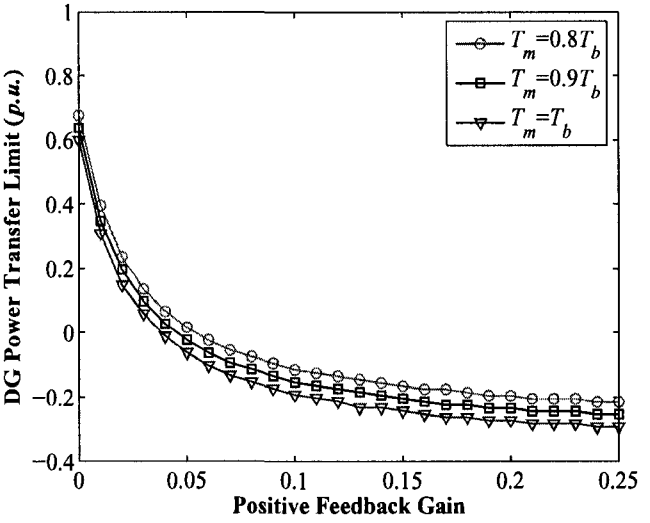

Figure 4.22: $P - K$ curves of the single DG system with induction motor load for different motor mechanical torques (T_m)

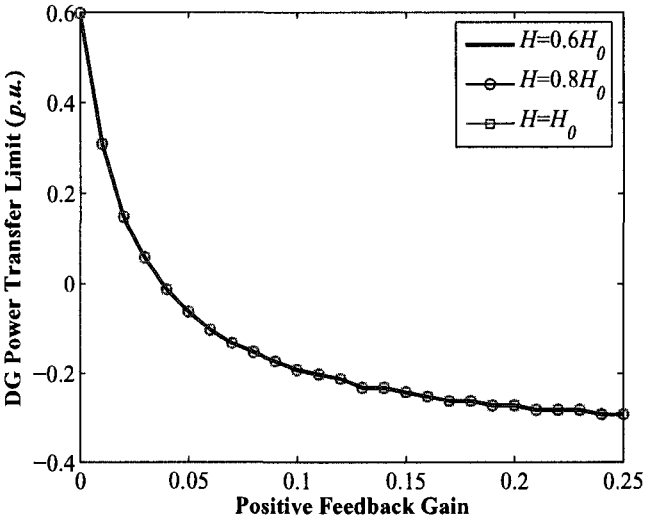

Figure 4.23: $P - K$ curves of the single DG system with induction motor load for different motor inertia constants (H)

Figure 4.23 shows the DG system $P-K$ curves when the motor inertia constant is changed from $0.6H_0$ to H_0. H_0 is the designed motor inertia constant shown in Table E.2. The comparison of the $P-K$ curves demonstrates the motor inertia constant has little effect on the DG power transfer limit.

The other factors affecting the DG system stability such as initial chopping fraction and distribution line impedance were also investigated for the motor load case. The conclusions for these factors drawn from the motor load case are similar with those drawn from the *RLC* load case.

4.4 Summary

This chapter presents a comprehensive analysis of the impact of the positive feedback anti-islanding scheme on the small-signal stability of grid-connected inverter-based DG systems. The analysis is based on the small-signal models of the single DG systems equipped with the SFS method. The *DG power transfer limit versus the positive feedback gain* $(P-K)$ curve is introduced as an index to determine and analyze the stability of DG systems. By using the curve, an extensive sensitivity study is conducted. According to the sensitivity analysis results, it is concluded that a strong positive feedback of the anti-islanding scheme will destabilize the grid-connected DG system when the grid is weak and the DG local load level is high. The conclusion is suitable for both the *RLC* load case and the induction motor load case.

The interaction between the inverter interface controls and the positive feedback anti-islanding control is also investigated. It is observed that the effect of the constant power controller and the constant current controller on the inverter-based DG system small-signal stability is different when the DG is connected to the grid in the presence of positive feedback anti-islanding scheme. The interaction between the controllers and the positive feedback anti-islanding scheme makes the difference more complex. The constant current-controlled DG has larger small-signal stability margin than the

constant power-controlled DG when the DG local load level is low for the *RLC* load case. However, the constant power-controlled DG can deliver more power at the high load level.

In addition, the chapter proposes to use the $P - t$ curve as a tool to design the parameters of the positive feedback anti-islanding methods for the *RLC* load case. With this curve, one can find a trade-off solution between the maximum power transfer limit and islanding detection capability.

Chapter 5

Impact of Positive Feedback Anti-Islanding Scheme on Multi-DG System

From the analysis of single DG systems, we know that the maximum DG transfer power can be determined by using small-signal analysis. In this chapter, the proposed methodology is extended to a power distribution system embedded with multiple DG units to determine their penetration limit. With the help of this analytical tool, the impact of the positive feedback control on the distribution system small-signal stability is investigated quantitatively. The interactions among the multiple DGs caused by the positive feedback anti-islanding protection are studied as well. Based on electromagnetic transient simulations, this chapter also presents the investigation results on the dynamic characteristics of the multiple inverter-based DG system in the presence of positive feedback anti-islanding protection. The conflict problem between multiple DG units stability and islanding detection capability is investigated as well.

5.1 DG Penetration Level in Distribution System

DG has changed the topology of modern distribution systems. Problems such as voltage rise effect, harmonics and flicker, over current protection, and distribution system instability can be caused by installing multiple DGs in distribution systems. Due to these restrictions, the amount of power, which is defined as the DG penetration level, that can be transferred from DGs to the distribution system is significantly

limited.

Because of the complexity of the subject, determining the DG penetration limit is difficult if all these constraints are considered. Usually, the DG penetration limit in a given distribution system is viewed in terms of the individual aspect. Discussions of the impact of voltage rise limitations, harmonic limitations and overcurrent protection on the DG penetration level can be found in [82]- [84].

In this section, the small-signal analysis approach is used to determine the penetration limit of multiple inverter-based DGs installed on a distribution system feeder. When the DGs provide more power than the loads, the feeder begins to transfer the surplus power to the upstream sub-transmission or transmission systems. As is well known, this extra power has a boundary because of the feeder's voltage quality limitation. Another limitation could be the DGs' dynamic characteristics. For example, if the positive feedback anti-islanding control is relatively strong, the DGs will lose their local stability, and the whole feeder will become unstable eventually. This situation may happen even when the DGs output less power than their local loads.

It was shown in Chapter 4 that a single DG power transfer limit can be related to the positive feedback gain of the DG anti-islanding control through a $P - K$ curve expressed as follows:

$$P_{max} = f(K_f) \tag{5.1}$$

where the function of the curve is f. In applications of multiple DG units, a similar curve can be derived. The $P - K$ curve for n DGs can be expressed as

$$P_{max} = f(K_{f1}, K_{f1}, ..., K_{fn}) \tag{5.2}$$

where the positive feedback gains $K_{f1}, K_{f1}, ..., K_{fn}$ are related to the anti-islanding

control of individual inverter DG1, DG2,..., DGn, respectively. Unlike P_{max} in Equation (5.1), P_{max} in Equation (5.2) represents the **DG output power limit** instead of the **DG power transfer limit**, which is defined in Chapter 4 as the power limit transferred from the DG to the distribution network without including the DG local load. In multiple DG units application, it is convenient to use the *DG output power limit versus positive feedback gain curve*, which is also called $P-K$ curve in this thesis, to conduct the sensitivity analysis. The relationships between each positive feedback gain and the maximum output power limit of each generator are not independent in the function f because the multiple DGs interact with each other through the distribution network.

5.1.1 Key Factors Affecting the Penetration Level of Multiple DG Units

The definition of the multiple DG units $P-K$ curve facilitates the stability analysis of multiple DGs with a positive feedback anti-islanding scheme. With this curve, the collective impact of the positive feedback anti-islanding control on the small-signal stability of the distribution system with multiple DG units can be quantified, and the factors affecting the penetration limit of multiple DGs for an existing distribution system can be investigated comparatively. This section presents the investigation results for several factors affecting the DG penetration limit level in distribution systems. The main factors analyzed were DG location, number of DGs, substation capacitor size, transformer sizes, and feeder length. In order to carry out these stability studies, the Canadian Urban Benchmark Distribution System proposed in [77] is utilized. The schematic diagram of the test system is shown in Figure 3.24, and the details of the system are described in Chapter 3.

- DG Location

Because the multiple DGs are installed along the distribution feeder, the distance from each DG to the substation is different. The impact of the DG location on the DG penetration level is illustrated by Figure 5.1, where four $P-K$ curves are shown. For"K_{f1} changes" curve, the positive feedback gains of DG2, DG3 and DG4

(K_{f2}, K_{f3}, K_{f4}) are set as zero, and the DGs' output power (P_2, P_3, P_4) is fixed at $0.1p.u.$. The positive feedback gain of DG1 (K_{f1}) is increased to observe the changes in its output power limit (P_1). The DG output power limit will be the sum of P_1, P_2, P_3 and P_4. The other three curves are obtained in the same way by fixing the settings and output power of three DGs , and varying the setting and power of the other generator. Figure 5.1 shows that the DG output power limit is the highest for the "K_{f1} changes" curve and the lowest for the "K_{f4} changes" curve when the positive feedback gains of the four curves are the same. This result means that DG1 in the former curve can produce more power than DG4 in the later curve. In other words, the DG near the substation has less impact on the distribution system small-signal stability than the DG far away from the substation.

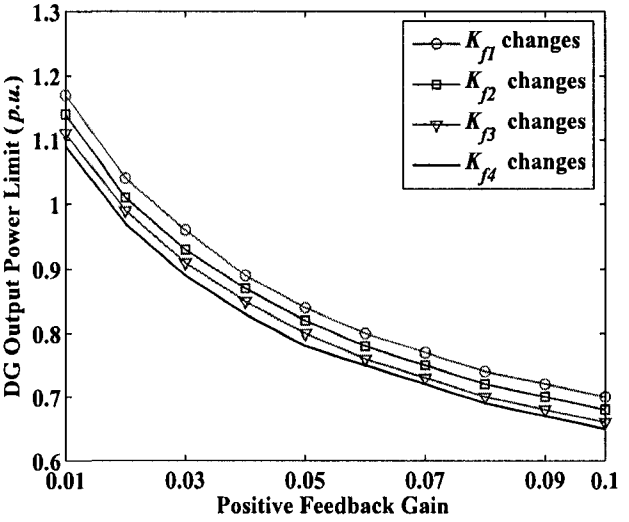

Figure 5.1: $P - K$ curves of the multiple DGs

This phenomenon can be further confirmed by participation factor analysis of the four DGs. Figure 5.2(a) shows the root loci of the distribution system with multiple DGs for the following situation: the four positive feedback gains are set as 0.1, and the active power of the four DGs is changed simultaneously and equally to get the root loci of the system eigenvalues. When this setting is used, the only difference among the DGs is the location. When the DGs' output power is increased to a specific

level, a pair of critical eigenvalues $(\lambda_{c1}, \lambda_{c2})$, whose real parts become positive, will be obtained (see Figure 5.2(b)). The participation factors of the DGs' state variables in the critical mode are displayed in Figure 5.3, which reveals that DG4 variables have the highest magnitude of the participation factors, and the DG1 variables have the lowest one. This result indicates that DG4 is more prone than the other DGs in the distribution system to become unstable.

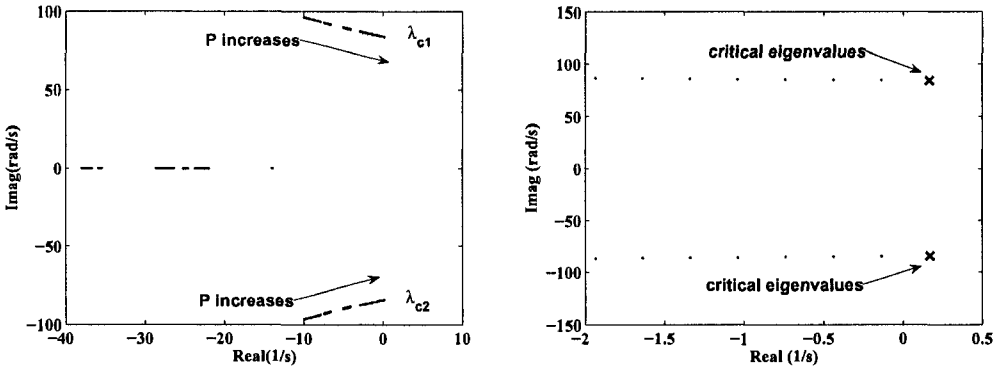

(a) Root loci of all the eigenvalues (b) Dislocation of the critical eigenvalues

Figure 5.2: Root loci of the test distribution system eigenvalues

An eigenvalue sensitivity study was also conducted based on the modal analysis of Figure 5.2. The sensitivity of the critical eigenvalue λ_{c1} to the DG positive feedback gains is shown in Table 5.1. The result shows that the critical eigenvalue is more sensitive to changes in K_{f4}, this finding means the positive feedback control of DG4 contributes more instability to the critical eigenvalue.

Table 5.1: Critical Eigenvalue Sensitivity Analysis

$\lvert\partial\lambda_{c1}/\partial K_{f1}\rvert$	8.4079
$\lvert\partial\lambda_{c1}/\partial K_{f2}\rvert$	9.3173
$\lvert\partial\lambda_{c1}/\partial K_{f3}\rvert$	9.9555
$\lvert\partial\lambda_{c1}/\partial K_{f4}\rvert$	10.2871

The main reason for the above result is that a generator far away from the substation has a relatively weak link with the strong power system, in this case represented by the utility source. As a result, this generator may lose its stability

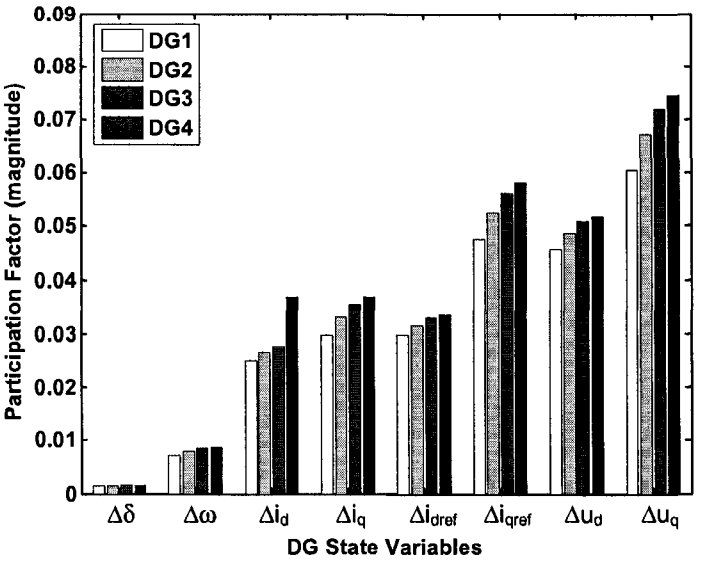

Figure 5.3: Participation factors of multiple DGs

easier if unstable factors such as the positive feedback anti-islanding control, are affecting it.

- DG Unit Number

The impact of DG unit number on the DG penetration level is shown in Figure 5.4 where the results of the following cases are presented:

1. 1 DG case - Only DG1 is installed in the feeder.
2. 2 DG case - Only DG1 and DG2 are installed. Each DG has the same output power and positive feedback gain.
3. 3 DG case - Only DG1, DG2 and DG3 are installed. Each DG has the same output power and positive feedback gain.
4. 4 DG case - All of the DGs are installed, each DG has the same output power and positive feedback gain.

Figure 5.4 displays the total DG power output limit curves. This figure shows that the total DG output power limit increases when there are more DGs spread in the

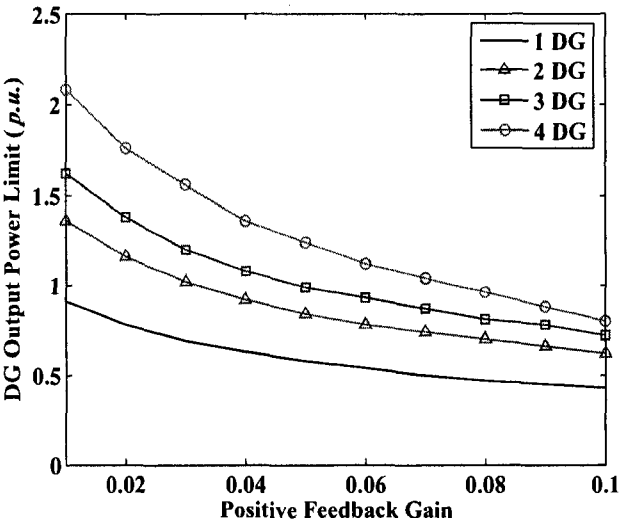

Figure 5.4: DG output power limit for different DG unit number

distribution system. However, the single DG unit output power limit is decreased with the increase in the DG unit numbers. Figure 5.5, showing the limit of DG1, illustrates the result, which is due mainly to the collective influence of the positive feedback anti-islanding control resident in the multiple DGs.

- Substation Capacitor

The capacitor bank installed at the substation provides reactive power to the distribution feeder. Figure 5.6 illustrates the impact of the substation capacitor size on the multiple DG penetration limit in terms of the small-signal stability. The P-K curves are determined by using the same method used for the four-DG case in Figure 5.5. Each curve in Figure 5.6 represents a different capacity of the substation capacitor bank. This figure reveals that when the reactive compensation installed at the substation increases, the multiple DG units' penetration level also increases. A large substation capacitor compensates for the reactive power consumed by the loads and improves the voltage profile along the feeder, and also the stability of the system.

- Substation and Load Transformers

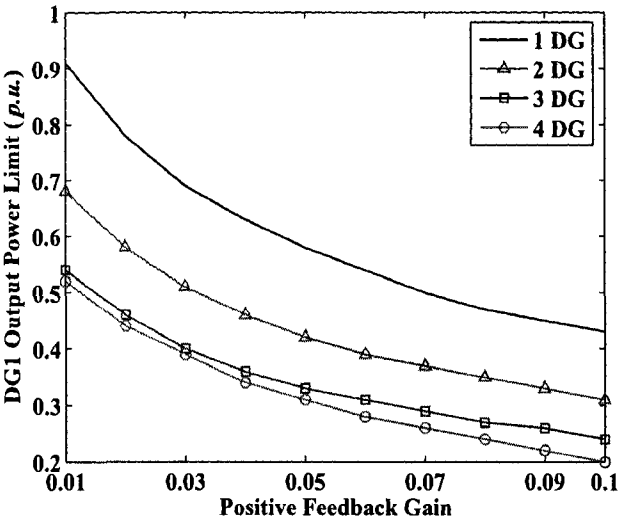

Figure 5.5: DG1 output power limit for different DG unit number

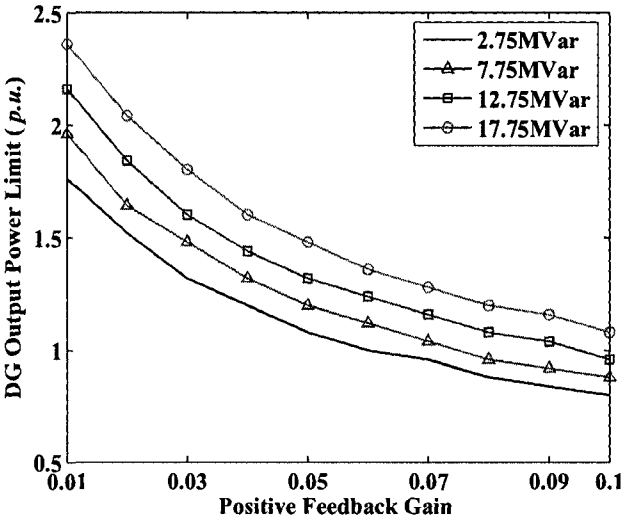

Figure 5.6: DG output power limit for different substation capacitor capacity

An increase in the capacity of the substation step-down transformer can also increase the DG output power limit. The results of the comparison are shown in Figure 5.7 where the substation transformer capacity is changed from $10MVA$ to $40MVA$. This outcome occurs because a high capacity transformer strengthens the connection between the feeder and the transmission system, and thereby, leads to an increase in the stability margin. Consequently, the DGs can deliver more power to the distribution system. Similarly, an increase in the capacity of the load transformers can also help to enlarge the DG output power level (see Figure 5.8). In this case, the connection between the local DG system and the feeder will be strengthened by using a high-capacity transformer.

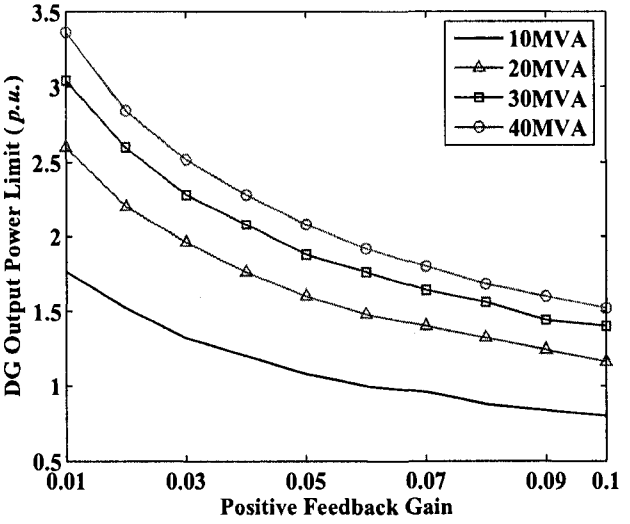

Figure 5.7: DG output power limit for different substation transformer capacity

- Feeder Length

Feeder length is another factor affecting the DG penetration limit in distribution systems. In Figure 5.9, the distance between every two DGs is varied to obtain different $P-K$ curves. This figure shows that a long feeder limits the DG penetration level. This result is understandable since the feeder impedance becomes larger as the length is increased, weakening the feeder's power transfer capability.

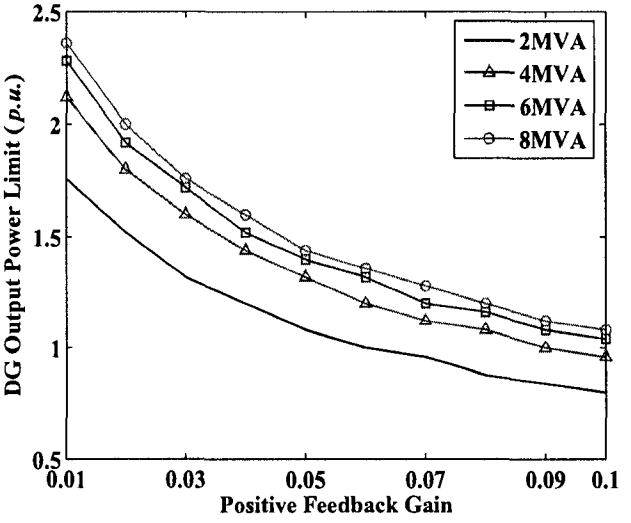

Figure 5.8: DG output power limit for different load transformer capacity

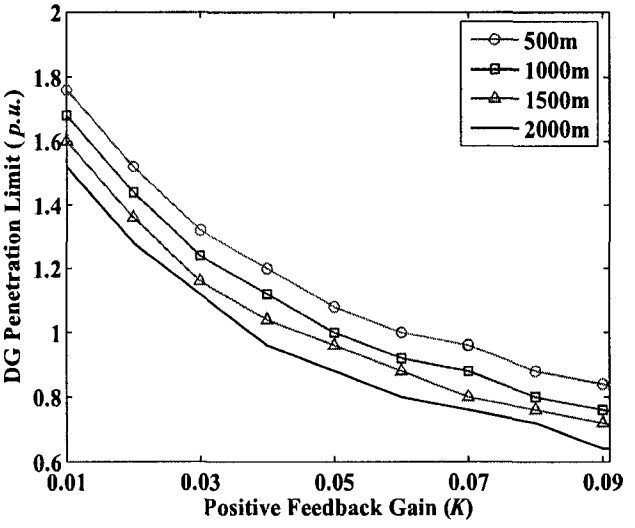

Figure 5.9: DG output power limit for different feeder length

5.1.2 Interaction among Multiple DG Units

The interferences among multiple DGs due to their resident anti-islanding protection are investigated in this section. Figure 5.10 shows the interaction for the cases where only DG1 and DG4 are connected to the distribution system feeder. Figure 5.10(a) exhibits the variation of the DG1 P-K curve when the DG4 output power is fixed at $0.2p.u.$; however, its positive feedback gain K_{f4} is increased from 0.01 to 0.1. This figure shows that the power transfer limit of DG1 decreases due to the increase of positive feedback gain K_{f4}. Therefore, one can conclude that the small-signal stability of a single distributed generator equipped with a positive feedback anti-islanding control will be affected by the positive feedback anti-islanding control of another generator installed in the same feeder. Figure 5.10(b) exhibits the variation of the DG1 $P-K$ curve when the DG4 output power is changed from $0.1p.u.$ to $0.2p.u.$ The positive feedback gain of DG4 is set as 0.1 for the two scenarios. Figure 5.10(b) shows that the DG1 power transfer limit is reduced when the DG4 output power is increased.

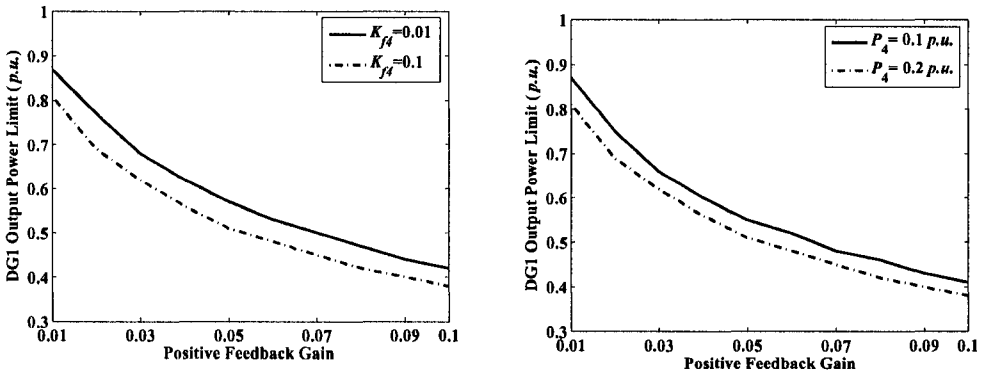

(a) $P_4 = 0.2p.u.$ (b) $K_{f4} = 0.1$

Figure 5.10: Interactions between DG1 and DG4

The relationship between the interaction and the number of DGs connected to the feeder is shown in Figure 5.11. Figure 5.11(a) displays the $P-K$ curves of DG1 for different numbers of DGs. The curve is the highest when only one distributed generator (DG4) is connected and the lowest when three DGs (DG2, DG3 and DG4)

are connected. Figure 5.11(b) investigates the impact of the inverter number on the $P-K$ curve of DG4. Similarly, the DG4 output power limit is reduced with an increase in the inverter number. Thus, Figure 5.11 demonstrates that the small-signal stability of a single distributed generator equipped with a positive feedback anti-islanding control will be affected by the number of DGs existing in the distribution system whether the single generator is close to the substation or at the end of the feeder.

Different distances between two DGs will also change the interaction. In Figure 5.12(a), the impact of DG4 and DG2 on the DG1 $P-K$ curve is compared. DG4 is electrically farther from DG1 than DG2 is. First, only DG1 and DG4 are connected to the feeder. The $P-K$ curve of DG1 is determined by fixing the DG4 output power and positive feedback gain. Then only DG1 and DG2 are connected to the feeder, and another DG1 $P-K$ curve is obtained by setting P_2 and K_{f2} constant. The comparison of the two curves shows that DG1 is more vulnerable to DG4. However, a different phenomenon is observed if the impact of DG1 and DG3 on the DG4 $P-K$ curve is compared. Figure 5.12(b) reveals that DG3 contributes more instability to DG4. That is to say, the generator far away from the substation has a greater impact on another generator's output power limit than the generator near the substation.

Figure 5.12 also shows that the closer a generator is to the substation, the less interaction occurs between this generator and the other DGs. This result is further demonstrated by Figure 5.13 where two cases are compared. In the first case, DG1, DG2 and DG4 are installed in the distribution system. The DG1 and DG4 output power and positive feedback gains are fixed to get the $P-K$ curve of DG2. Correspondingly, the $P-K$ curve of DG3 is obtained in the second case when DG1, DG3 and DG4 are installed. Figure 5.13 reveals that DG2 has a better output power performance than that of DG3.

In summary, when a group of inverter-based DGs exists in a given distribution system, the small-signal stability of each single DG unit is affected by the dynamic

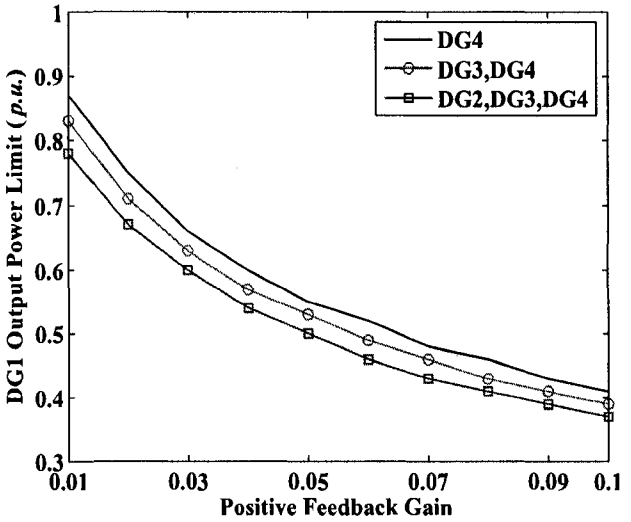

(a) "DG4 case": K_{f4}=0.1, P_4=0.1$p.u.$; "DG3, DG4 case": K_{f3}=K_{f4}=0.1, P_3=P_4=0.1$p.u.$; "DG2, DG3, DG4 case": K_{f2}=K_{f3}=K_{f4}=0.1, P_2=P_3=P_4=0.1$p.u.$

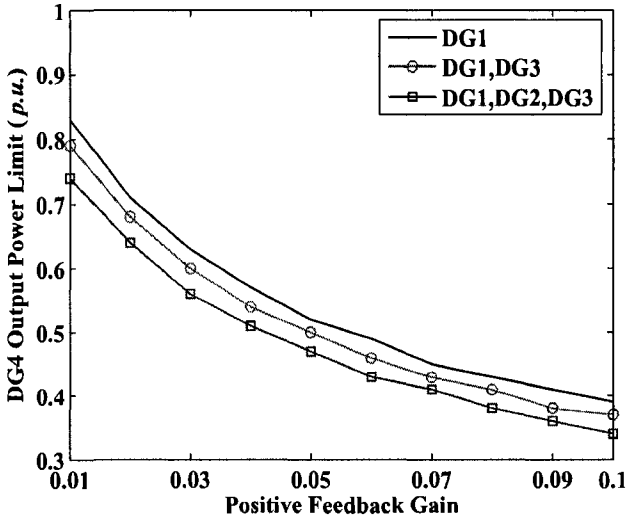

(b) "DG1 case": K_{f1}=0.1, P_1=0.1$p.u.$; "DG1, DG3 case": K_{f1}=K_{f3}=0.1, P_1=P_3=0.1$p.u.$; "DG1, DG2, DG3 case": K_{f1}=K_{f2}=K_{f3}=0.1, P_1=P_2=P_3=0.1$p.u.$

Figure 5.11: Interactions between DG1 and DG4

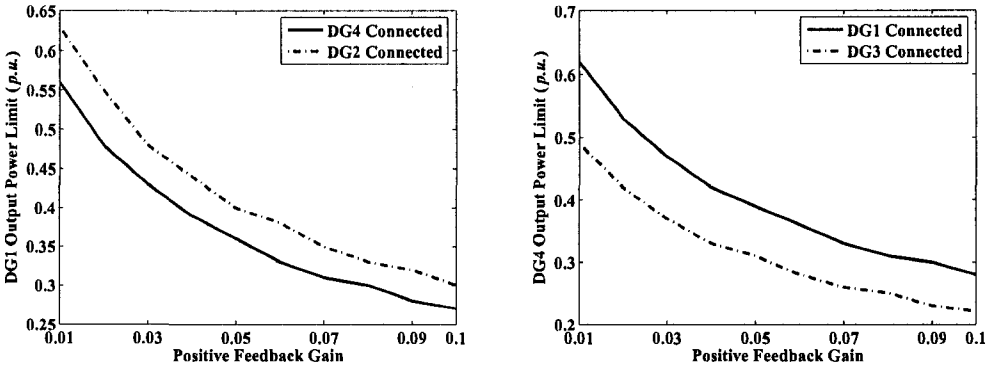

(a) "DG4 case": K_{f4}=0.2, P_4=0.2$p.u.$; "DG2 case": K_{f2}=0.2, P_2=0.2$p.u.$

(b) "DG1 case": K_{f1}=0.2, P_1=0.2$p.u.$; "DG3 case": K_{f3}=0.2, P_3=0.2$p.u.$

Figure 5.12: Effect of distance on the interactions among DGs

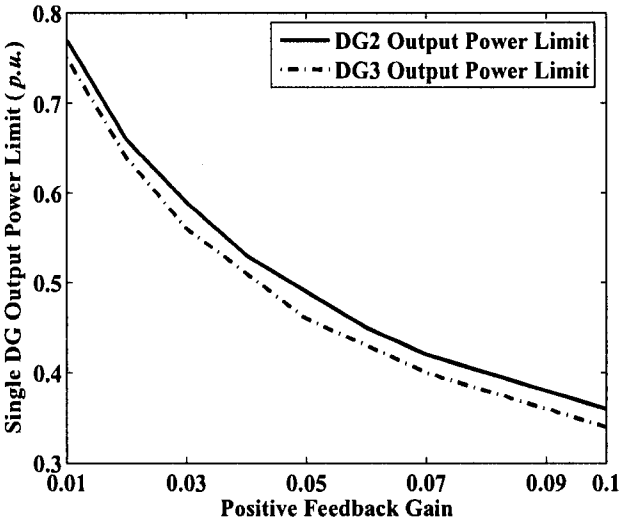

Figure 5.13: Comparison of the interactions of DG2 with DG1 and DG4 and of DG3 with DG1 and DG4 (K_{f1}=K_{f4}=0.1, P_1=P_4=0.1$p.u.$)

controls of the other DGs. The interaction between the single generator and the multiple DGs is strong if the DGs have a high value of the positive feedback gain for their anti-islanding protection. Also, the interaction is strongly related to the topology of the generator distribution. A generator far away from the substation can most easily lose its stability due to the impact of other DGs.

5.2 Impact of Anti-Islanding Control on DG System Dynamics

The potential for DGs to change the dynamics of a specific subsystem or distribution feeder becomes a concern when there is a significant penetration of DG relative to the total load power on that feeder [85]. This section investigates the transient behaviors of the multiple inverter-based DG system shown in Figure 3.24, with the positive feedback anti-islanding scheme as the main concern. The case studies are based on the transient model of the DG system set up in Matlab/Simulink.

5.2.1 Power Change Response

Figure 5.14 shows the DG1-DG4 terminal voltages, substation voltage and DG1 terminal frequency subsequent to a DG output power change disturbance. The output power references of the four DG units are stepped from $0.2p.u.$ $(2MW)$ to $0.3p.u.$ $(3MW)$ at $2.5s$ simultaneously. The DGs have the same anti-islanding settings and are all constant power-controlled. Three scenarios for different positive feedback gains are compared. Figure 5.14 reveals that the dynamic response of the distribution system is notably affected by the positive feedback strength of the anti-islanding scheme. For the $K_f = 0$ scenario, the distribution system goes back to steady state in a relatively short period after the disturbance. When K_f is 0.03, the voltage and frequency within the distribution system experiences a relatively long oscillation which is not well damped. The magnitude and the duration of the oscillation become higher and longer as K_f increases. If the positive feedback gain becomes higher, the system voltage and frequency will violate the restrictions of the DG protection relays after the disturbance, and will cause a nuisance trip for the DG units. Thus,

the strong positive feedback anti-islanding protection decreases the disturbance ride through capability of the interconnected DG units.

Another case is studied to compare the dynamic responses of the multiple DG units to the disturbances from different locations of the feeder. Two scenarios are simulated. In the first scenario, P_{ref1} of DG1 is stepped from $0.2p.u.$ to $0.4p.u.$ at $4s$. The power references of the other three DG units are all $0.2p.u.$. In the second one, P_{ref4} of DG4 is stepped from $0.2p.u.$ to $0.4p.u.$ at $4s$, and the power references of DG1-DG3 are all $0.2p.u.$. The positive feedback gains of the four DG units are all 0.03 for both scenarios. Figure 5.15 shows the dynamics of the terminal voltages and frequencies of DG1-DG4 subsequent to the disturbances. This figure reveals that DG1 is more easily disturbed in the "P_{ref1} **Step**" scenario. This result occurs because the disturbance occurs close to DG1. Similarly, DG4 reacts more drastically in the "P_{ref4} **Step**" scenario. However, even though DG2 is close to the disturbance in the "P_{ref1} **Step**" scenario, DG2 and DG3 are more affected in the "P_{ref4} **Step**" scenario. The comparison indicates that in order to improve the feeder's local stability, the DG units should be installed close to the substation. This observation is in accordance with the small-signal analysis result presented in **Section 5.1**. Figure 5.16 shows the substation voltages in the two scenarios, which also demonstrate the above conclusion.

5.2.2 Capacitor Switching Response

One study found that a DG unit adds additional damping to the capacitor switching transient in distribution systems [85]. The impact of the positive feedback anti-islanding control on the damping effect is investigated in this section. Figure 5.17 shows the substation voltage, the DG1 terminal voltage and the feeder frequency responses to the capacitor bank switching disturbance at the substation. At first, the substation is supplied with a capacitor bank of $1.75MVar$. Another $1.5MVar$ capacitor bank is switched in at $2.5s$. Figure 5.17 shows that the transient voltage and frequency between the $2.5s$ and $2.55s$ are not affected by the positive feedback gains, whereas after $2.55s$, the system with stronger positive feedback gain needs more time to go to the steady state. This finding indicates that for inverter-based

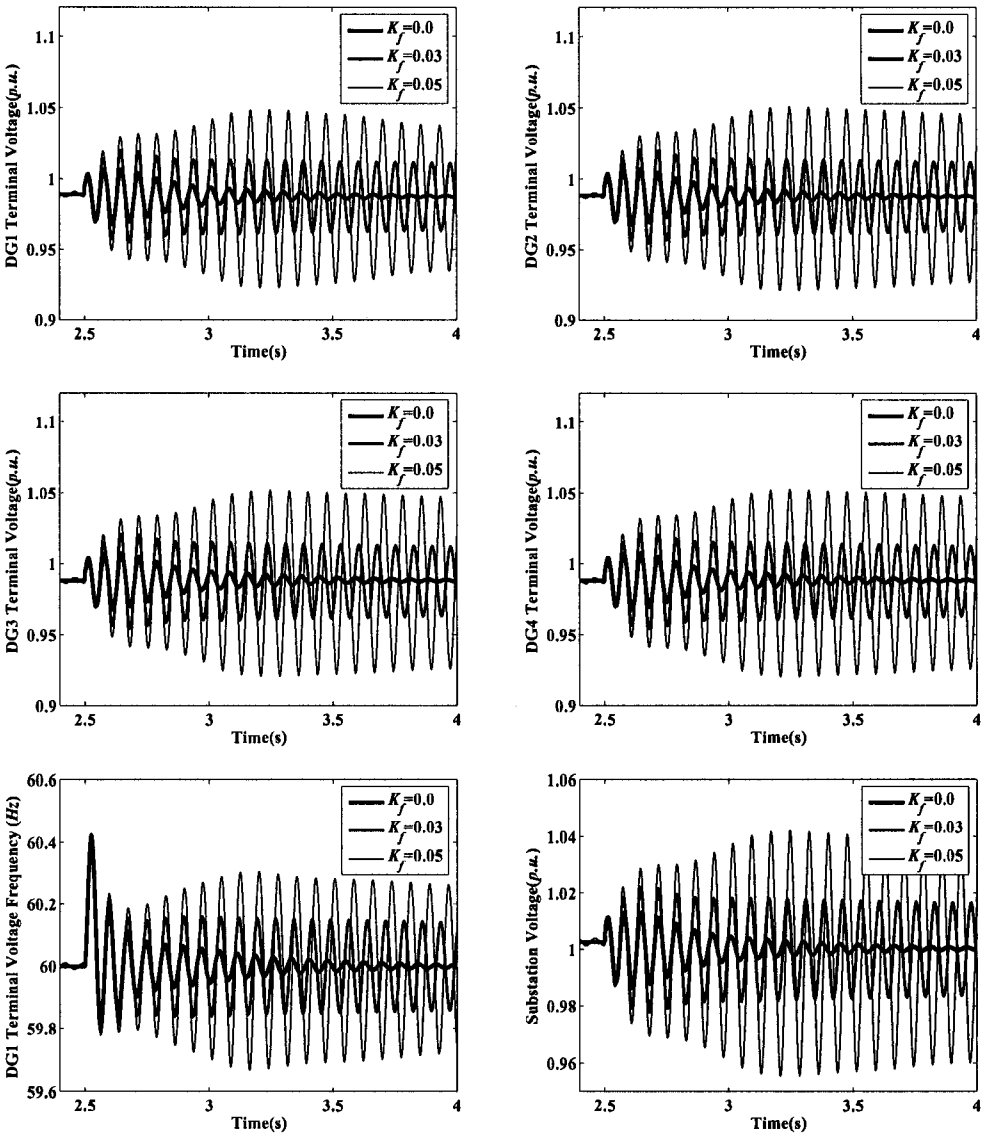

Figure 5.14: Distribution system dynamics subsequent to DG output power change

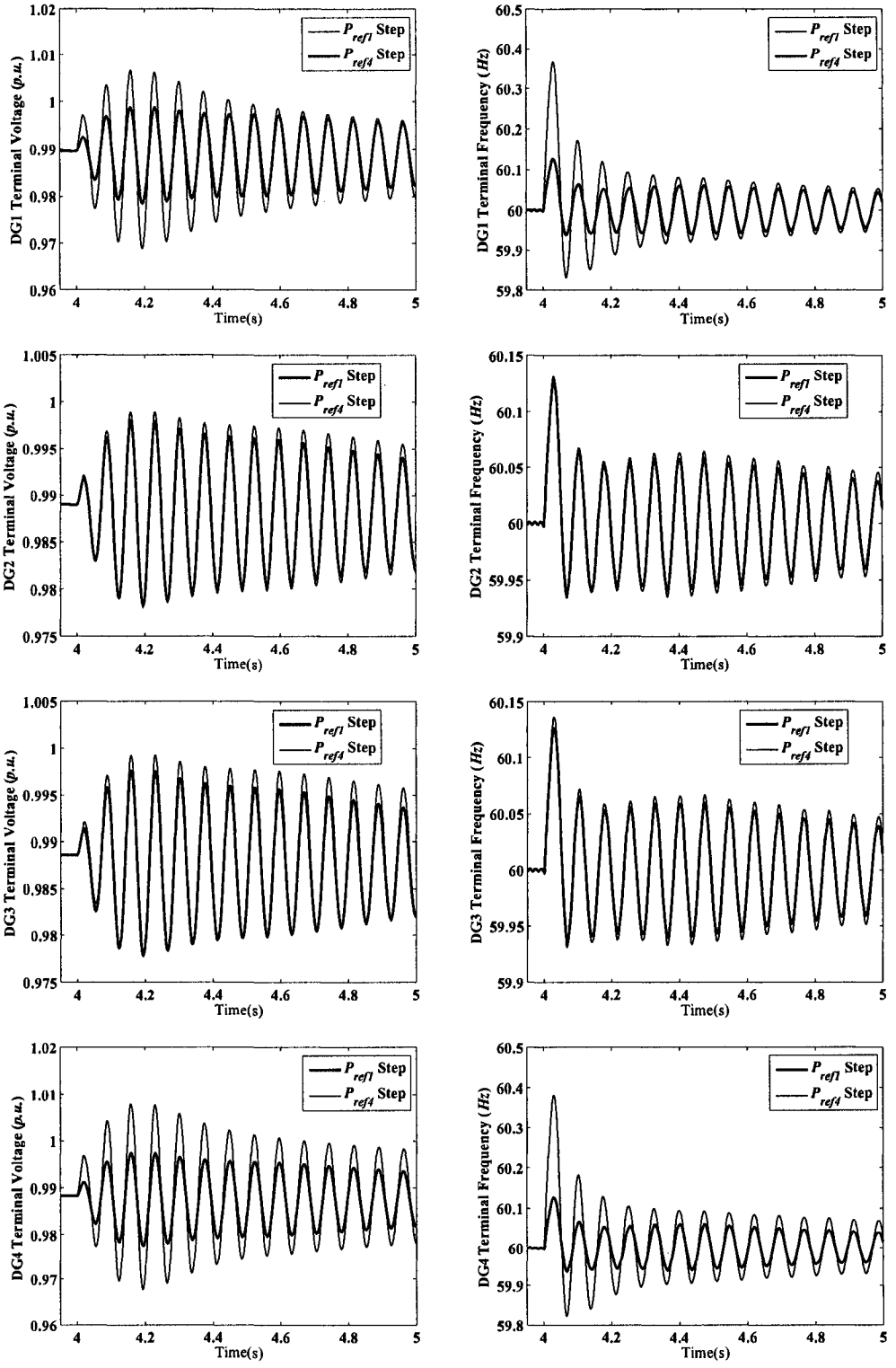

Figure 5.15: DG1-DG4 terminal voltage and frequency responses to different power step disturbances

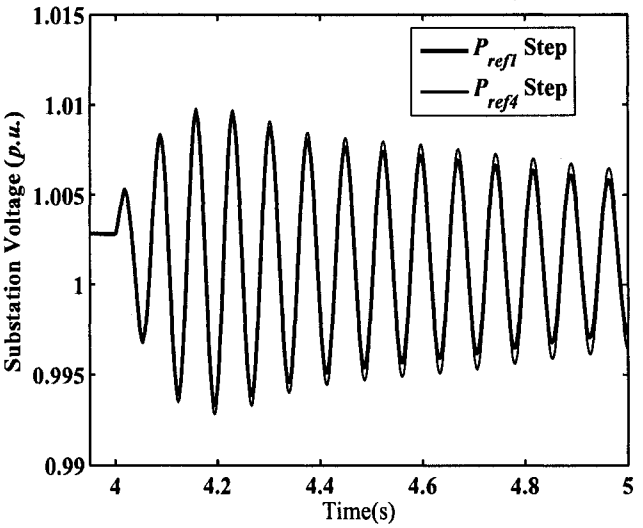

Figure 5.16: Substation voltage responses to different power step disturbances

DG units, the positive feedback anti-islanding control corresponds to a relatively slow transient process compared with the fast transient disturbances occurring in distribution systems such as capacitor switching.

5.2.3 Fault Response

A three-phase-to-ground fault was applied to the terminal of DG4 in EMTP simulation. The fault occurred at $6s$ and was cleared at $6.05s$. Figure 5.18 displays the terminal voltages of the DG units during and after the fault. The transient voltages are compared under three different DG positive feedback gain settings. In the first scenario, all the DG units have a gain of 0.01, and in the later scenarios, the positive feedback gains of the DGs are changed simultaneously. The positive feedback gain has little impact on the voltage sags during the fault; however, the voltages in the scenario with the strongest positive feedback gain have the worst damping characteristic after the fault.

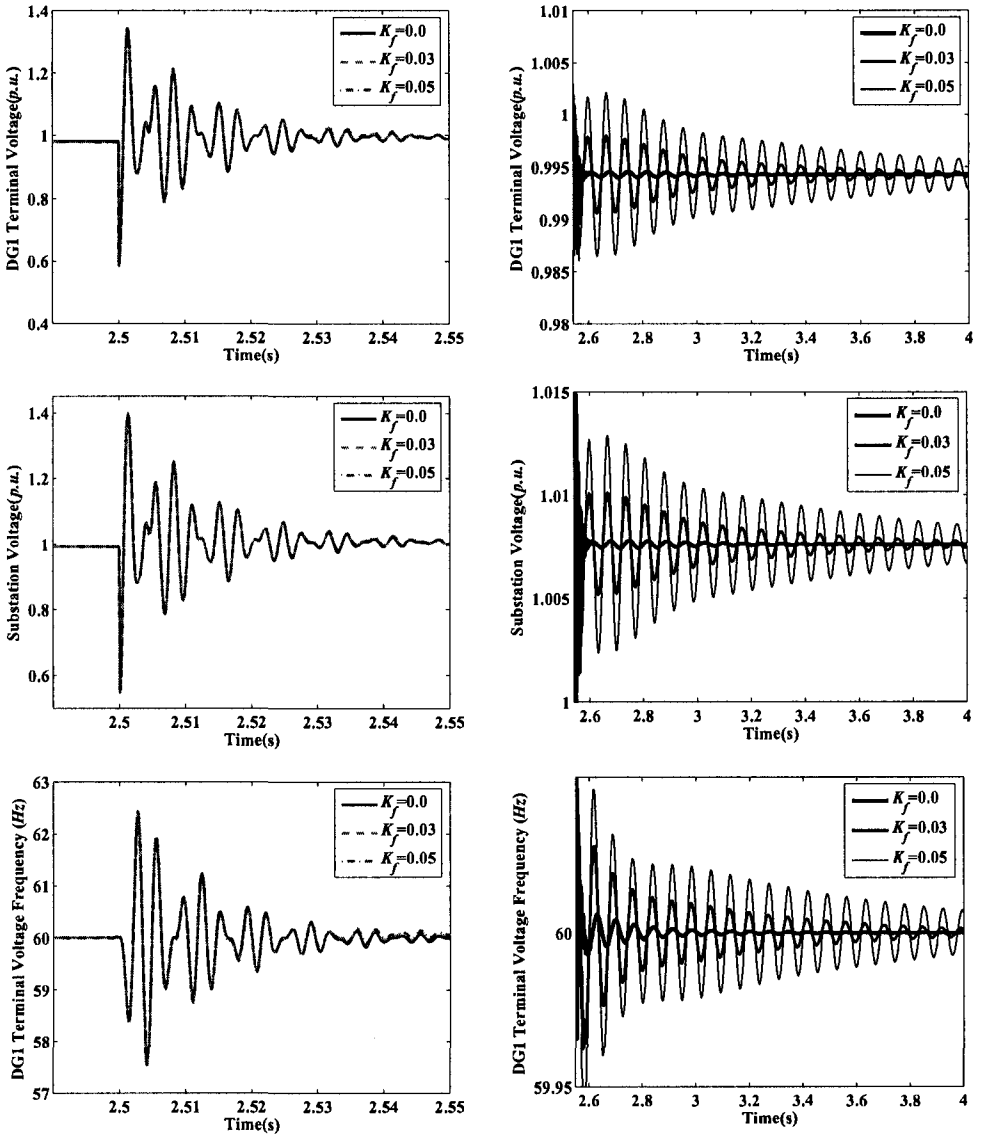

Figure 5.17: Distribution system dynamics subsequent to capacity bank switching

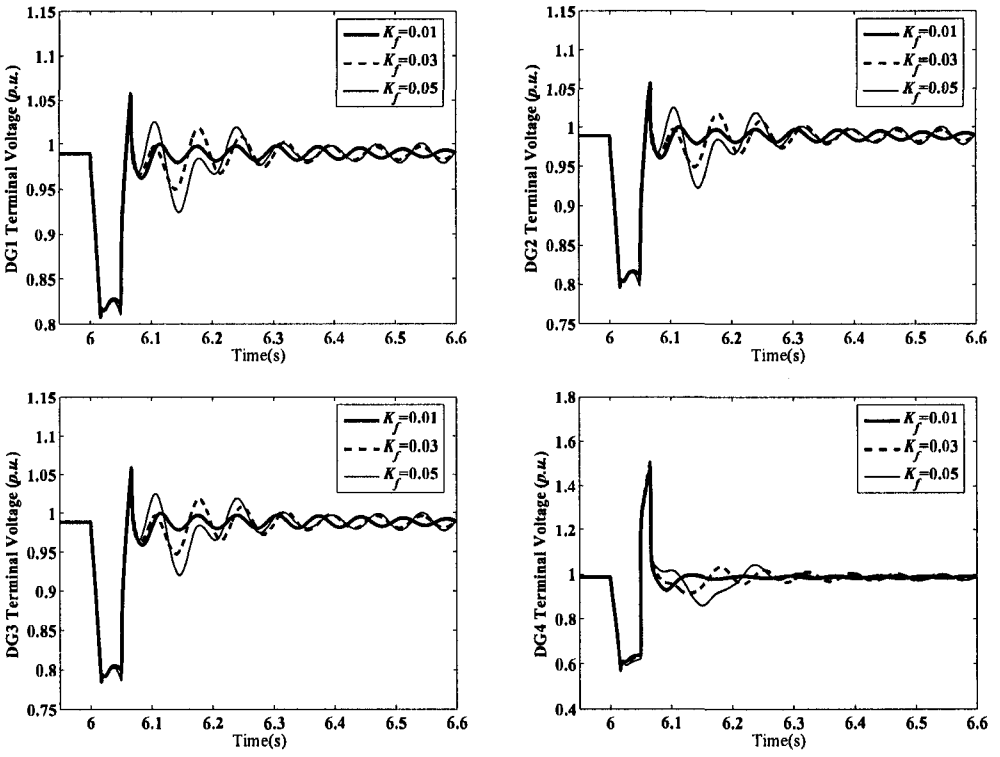

Figure 5.18: Distribution system dynamics subsequent to three-phase-to-ground fault

5.3 Conflict between Multiple DG Units Stability and Islanding Detection Capability

In a distribution system with multiple DG units, if the loads' active and reactive power are well balanced by the DGs and the capacitor banks, the islanding will not be detected by the DGs without additional anti-islanding protection. Figure 5.19 reveals the DG1-DG4 terminal frequency changes after the circuit breaker CB1 in Figure 3.24 is opened at $8s$. The capacitor bank installed at the substation is $2.47MVar$ and the output power references of DG1-DG4 are all $1.85MW(0.185p.u.)$. For these settings, the constant impedance loads are all supplied by the DGs and the capacitor bank. As a result, the active power and reactive power flowing through the substation are almost zero. Figure 5.19 shows that due to the nearly balanced power within the distribution system, the terminal frequencies of the four DGs change a little after

the islanding. The DGs will continue to transfer power to their local loads in this situation. The further study based on EMTP simulations shows that as long as the power balance condition at the spot of substation is satisfied, the DG system islanding will not be detected no matter how the DGs, the compensation capacitor banks and the loads are distributed. The above conclusion is based on the assumption that the islanded system will be stable after the circuit breaker at the substation is open.

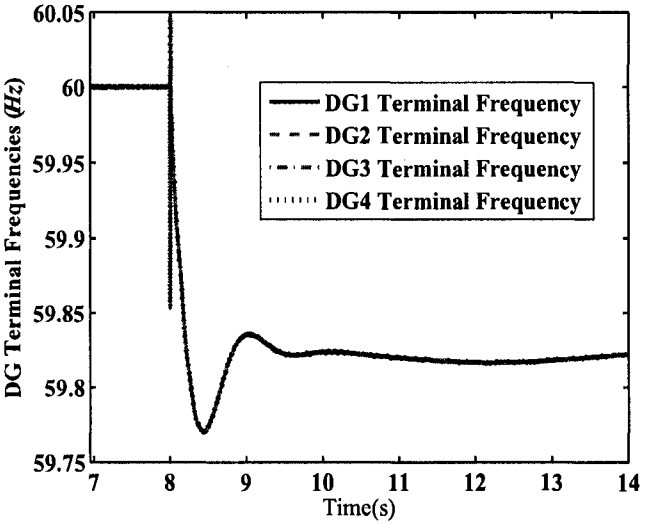

Figure 5.19: Terminal frequencies of DG1-DG4 after pre-balanced islanding

If the multiple DG units are equipped with the positive feedback anti-islanding scheme, the unintentional islanding of the DG system can be detected effectively. Basically, the higher the DG units' positive feedback gains are, the more efficient the detection performance is. However, the strong positive feedback could cause a stability problem when the DG system is connected to the main grid. Thus, the positive feedback gains of the multiple DG units cannot be too high. Compared with the conflict problem in the single DG unit case, the conflict problem addressed in the DG system with multiple DG units is more complex as each individual DG unit can have a unique positive feedback gain setting, and the multiple DG units interact with each other.

5.3.1 Islanding Detection of Multiple DG Units

Figure 5.20 displays the DG1-DG4 terminal frequencies after the DG system islanding for three scenarios. The distribution system's and DG units' parameter settings in these scenarios are the same as those in Figure 5.19. The differences among the scenarios are the positive feedback gain values for the four DG units. The islanding occurs at $8s$. In the first scenario, all the positive feedback gains are 0.01. Obviously, the islanding phenomenon can be quickly detected in this situation as the islanded DG system loses its stability after the loss of the mains. In the second scenario with $K_{f1} = 0, K_{f2} = K_{f3} = K_{f4} = 0.01$, the DGs will not trip themselves as the aggregate positive feedback anti-islanding control is not strong enough to destabilize the islanded DG system, and the island's steady-state frequency is within the trip limits of the frequency relays due to the power balance at the substation. In the third scenario($K_{f1} = 0.05, K_{f2} = K_{f3} = K_{f4} = 0$), the DG system becomes unstable after the islanding; however, only DG1 contributes the destabilizing force.

Thus, different combinations of positive feedback gain settings are available for the multiple DG units to detect the island. The choice could be to equip only one or a few generators with high positive feedback gain, with the others not protected by the positive feedback control, or to equip every generator with moderate positive feedback gain. Although these combinations can ultimately all destabilize the islanded DG system, their islanding detection performance is different. For example, in Figure 5.20, the third scenario has a shorter islanding detection time than the second scenario has. Furthermore, the impact of the anti-islanding control on the grid-connected DG system stability also depends on how the positive feedback gains are distributed among the DG units. Based on these factors, the operators must determine which choice has the least negative impact on the interconnected DG system while offering the better islanding detection performance at the same time.

An example of an investigation of the above conflict problem is illustrated in Figure 5.21, which reveals the DG1 frequency after islanding in four scenarios. In the left

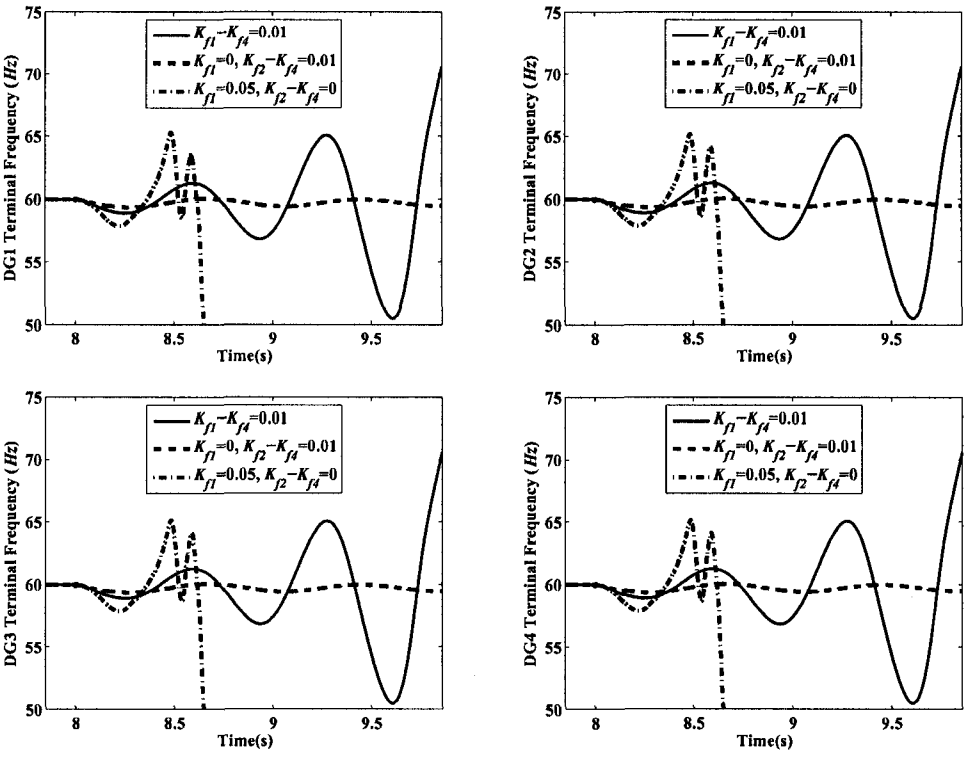

Figure 5.20: DG1-DG4 terminal frequencies for the stable and unstable islanded DG system

part of the figure, two scenarios are compared. In the first scenario, the positive feedback gains of the DG units are $K_{f1} = K_{f2} = 0, K_{f3} = K_{f4} = 0.02$. In the second one, the gains are set as $K_{f1} = K_{f2} = 0.02, K_{f3} = K_{f4} = 0$. The system's other parameter settings are the same with those in Figure 5.20. The comparison shows that the two scenarios have almost the same dynamic process after the feeder is disconnected from the main grid (The substation circuit breaker CB1 is opened at $8s$). The reason is mainly because the topologies of the islanded system do not significantly differ in these scenarios (only the location of the capacitor bank, which is not essential to the dynamics of the islanded system, is different). On the other hand, the small-signal stability analysis of the DG system shows that the power system's critical eigenvalues before the islanding are $-3.2822 \pm j87.0890$ for the first scenario and $-3.3359 \pm j87.1273$ for the second scenario. As a result, the positive

feedback control in the first scenario has more negative impact on the interconnected-DG system than that in the second one as the real part of the critical eigenvalues for the first scenario is closer to zero. This result occurs because when the feeder is connected to the main grid, the topology of the DG system in the two scenarios will be quite different. The DG units with strong positive feedback are far from the substation in the first scenario and near the station in the second scenario. The right part of Figure 5.21 also depicts this phenomenon, where positive feedback gain settings in the third and the fourth scenario are $K_{f1} = K_{f2} = 0, K_{f3} = K_{f4} = 0.05$ and $K_{f1} = K_{f2} = 0.05, K_{f3} = K_{f4} = 0$, respectively. The corresponding critical eigenvalues of the DG system in these two scenarios before the islanding are $-2.5747 \pm j86.5198$ and $-2.6948 \pm j86.6059$. Therefore, it can be concluded that the DG units with strong positive feedback anti-islanding control should be installed near the substation.

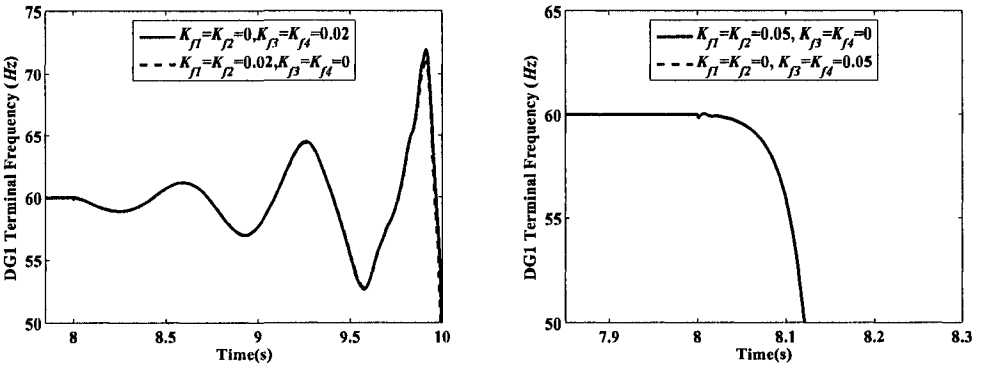

Figure 5.21: DG1 terminal frequency after islanding

5.3.2 $P-t$ Curves for Multiple DG Units

In order to obtain the more general conclusions for the conflict problem of the positive feedback anti-islanding control, the concept of the $P-t$ curve used for a single DG unit is extended to multiple DG units in this section. In Figure 5.22, four $K-t$ curves are plotted for DG1-DG4 based on EMTP simulations. The DG system parameter settings for the $K-t$ curves are as follows:

DG1 curve $P_{ref1} = P_{ref2} = P_{ref3} = P_{ref4} = 0.185 p.u., K_{f2} = K_{f3} = K_{f4} = 0.01$. K_{f1} is changed from 0.011 to 0.03.

DG2 curve $P_{ref1} = P_{ref2} = P_{ref3} = P_{ref4} = 0.185p.u., K_{f1} = K_{f3} = K_{f4} = 0.01$. K_{f2} is changed from 0.011 to 0.03.

DG3 curve $P_{ref1} = P_{ref2} = P_{ref3} = P_{ref4} = 0.185p.u., K_{f1} = K_{f2} = K_{f4} = 0.01$. K_{f3} is changed from 0.011 to 0.03.

DG4 curve $P_{ref1} = P_{ref2} = P_{ref3} = P_{ref4} = 0.185p.u., K_{f1} = K_{f2} = K_{f3} = 0.01$. K_{f4} is changed from 0.011 to 0.03.

Correspondingly, the $P - K$ curves for the above scenarios are obtained through small-signal analysis of the DG system. For the DG1 curve scenario, the power references and positive feedback gains of DG2-DG4 are fixed, and the DG1 output power limit is acquired for each K_{f1}. By this means, the $P - K$ curve for DG1 is procured. The other three $P - K$ curves are plotted similarly by varying the parameters of only one DG.

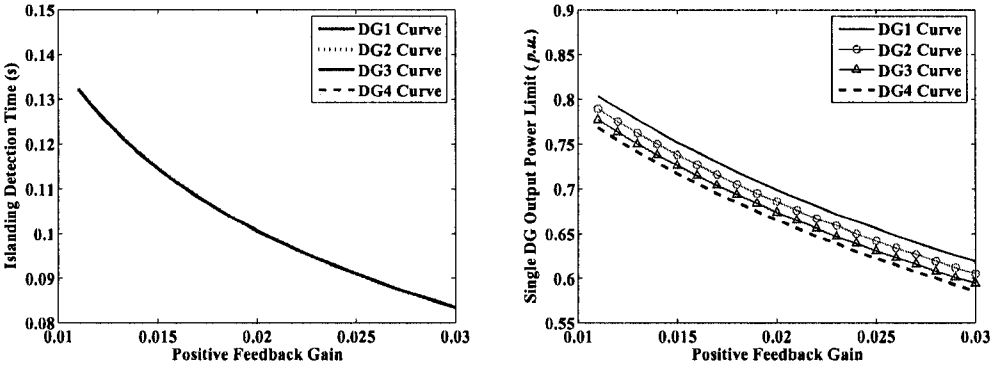

Figure 5.22: $K - t$(left part) and $P - K$(right part) curves for DG1-DG4

Figure 5.23 combines the $K - t$ curves and $P - K$ curves into $P - t$ curves. The $P - t$ curves show that the DG system has the largest output power limit in the DG1 curve scenario if the islanding detection time is required to be the same in the four scenarios. This observation agrees with the conclusion drawn from Figure 5.21.

The interactions among the multiple DG units in the $P - t$ curve study are illustrated in Figure 5.24 where the DG1 curve scenario shown in Figure 5.23 is

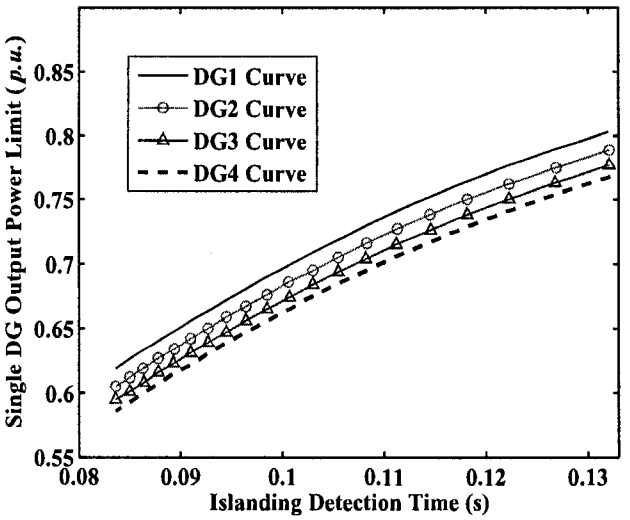

Figure 5.23: $P-t$ curves for DG1-DG4

compared with a new scenario which has $K_{f2} = 0.02$. Only K_{f2} is different in these two scenarios. Figure 5.24 shows that if the same DG1 output power limit is required by the two scenarios, the scenario with $K_{f2} = 0.02$ (refer to point **A**) has a shorter islanding detection time than that of the scenario with $K_{f2} = 0.01$ (refer to point **B**). In fact, point **C** has the same K_{f1} value with point **A**, while K_{f2} is different for these two points. If we assume $K_{f1} = K_{f2} = K_{f3} = K_{f4} = 0.01$ at first, and we want to shorten the DG system islanding detection time, should we increase K_{f1} to 0.017 and keep the other gains unchanged, or should we increase K_{f1} to 0.016 and K_{f2} to 0.02? Actually, these two methods have the same impact on the DG1 output power transfer limit. However, the latter method has a smaller islanding detection time. Similarly, if the same islanding detection time is required by the two scenarios, point **A** should be used instead of point **D** as the DG1 power transfer limit is larger for point **A**.

The impact of DG3 and DG4 on the DG1 $P-t$ curve was also investigated. The result in Figure 5.25 shows that the DG1 $P-t$ curve is affected by DG2-DG4 in almost the same way. Increasing K_{f2} or increasing K_{f4} to reduce the islanding detection time does not provide significantly different results. In addition, the impact of DG1-DG3

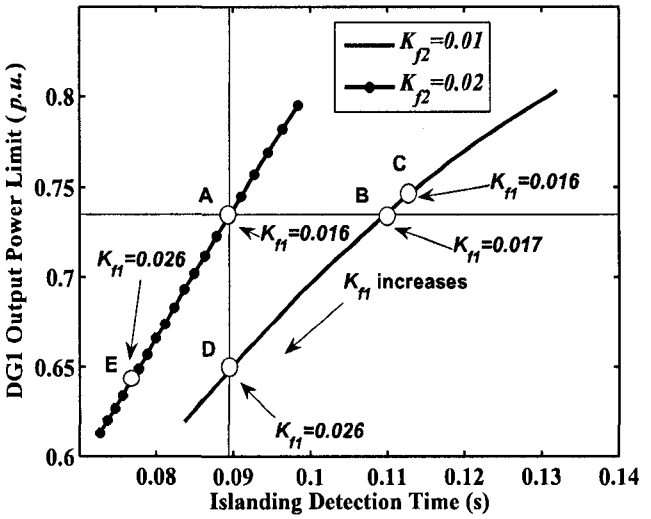

Figure 5.24: Impact of K_{f2} on the DG1 $P-t$ curve

on the DG4 $P-t$ curve is displayed in Figure 5.26. The overall effect of increasing only K_{f4} to a high value on islanding detection is not better than that of increasing K_{f4} and $K_{f1}-K_{f3}$ to moderate values.

5.4 Summary

The investigation of the impact of positive feedback anti-islanding control on a DG system is extended to multiple DG units in this chapter. The power transfer limit of multiple DG units in a given distribution system is analyzed by first using the linearized modeling method. By using the $P-K$ curve, a parametric analysis is conducted to determine how the key factors such as DG location, DG unit number, substation capacitor bank, load transformers and feeder length affect the penetration level of multiple DG units. The following conclusions are drawn from the sensitivity analysis:

- Embedded with positive feedback anti-islanding control, the DGs installed near the substation of distribution systems contribute less destabilizing force on the power system than those located at the end of the feeders.

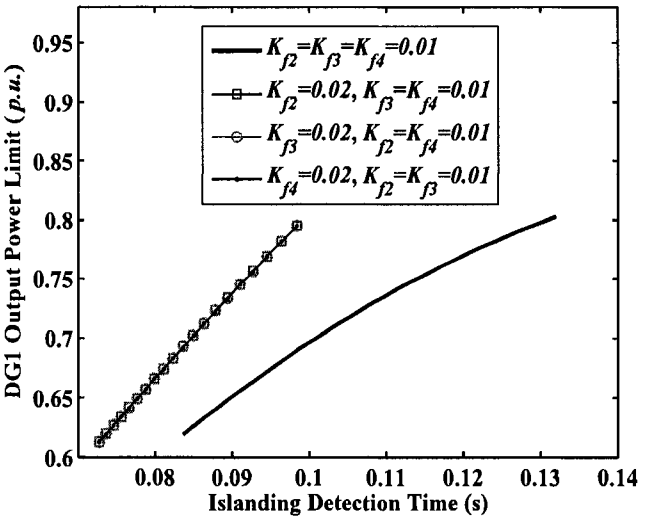

Figure 5.25: Impact of DG2-DG4 on the DG1 $P-t$ curve

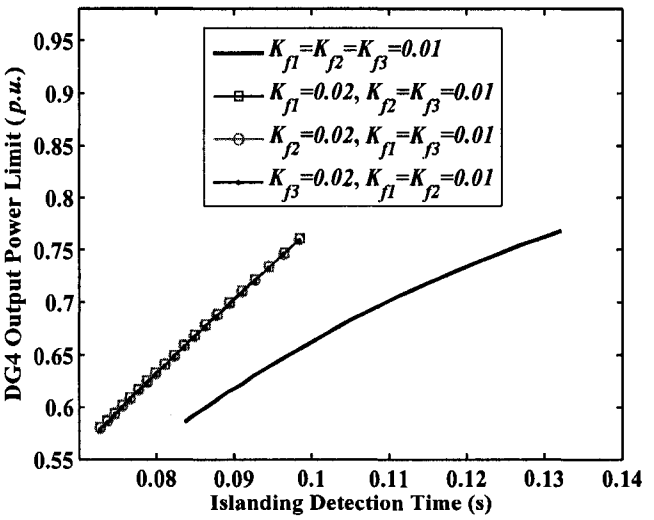

Figure 5.26: Impact of DG1-DG2 on the DG4 $P-t$ curve

- An increase in the capacity of the substation capacitor bank and the step-down transformers can enhance the penetration level of multiple DG units.
- The total DG transfer power capability can be enlarged by installing more DG units; however, the individual DG output power level will be limited to the increase of the DG unit number.
- The power transfer limit of multiple DG units is reduced if the feeder between the DGs is increased in length.

This chapter also studied the interactions among multiple DGs due to their resident anti-islanding protection. The small-signal stability of a single interconnected-DG unit is greatly affected by the positive feedback anti-islanding control strength of other DG units within the distribution system. The more DG units there are, the stronger the interactions are. As well, the interactions are influenced by the distribution topology of the DG units.

Besides the small-signal stability analysis of the multi-DG system, the impact of a positive feedback anti-islanding scheme on the DG system transient behaviors is explored based on the EMTP simulations. The simulation results show that the strong positive feedback anti-islanding control decreases the disturbance ride through capability of the interconnected DG units, and that the positive feedback anti-islanding control is related to a relatively slow transient process compared to the network-induced fast transients.

The conflict problem between DG power transfer capability and islanding detection capability addressed in single DG systems also exists in multi-DG systems. Correspondingly, the concept of the $P - t$ curve is applied to multi-DG systems in this chapter. With the help of the curve, it is concluded that in order to obtain high efficiency in islanding detection and a low impact on DG system stability, the DG units with strong positive feedback gain should be installed close to the substation, and the

positive feedback protection of multiple DGs should be coordinated together instead of increasing the strength of individual DG units' anti-islanding control arbitrarily.

Chapter 6

Islanding Detection Performance of Positive Feedback Anti-Islanding Scheme

The traditional NDZ analysis methods used for anti-islanding schemes are all based on the assumption that the islanded DG system will reach a new steady state after the islanding. If the voltage and frequency of the new steady state are within the ranges of the relay settings, then the islanding will not be detected, and the DG will not be tripped. The dynamic process of the islanding is not considered in these methods. For the positive feedback anti-islanding methods, the steady-state information of the islanding alone is not enough to explain their nature and characteristics. Understanding the impact of the positive feedback mechanism on the stability of the islanded DG system is necessary in NDZ studies. This chapter utilizes small-signal stability analysis of the islanded DG system to study the NDZ of positive feedback anti-islanding scheme resident in single or multiple inverters.

6.1 Small-Signal Analysis of Islanded DG system

The positive feedback anti-islanding control is known to always try to destabilize the DG unit even if it is grid-connected. When the DG unit is connected to the utility system, the strength of the grid is much stronger than that of the positive feedback, and the DG system will be operated in a stable manner. Once the islanding is formed, the positive feedback begins to disturb the DG in a noticeable manner. If the

strength of the positive feedback is weak, the islanded system will finally ride through the destabilization. For the single inverter-based DG system shown in Figure 2.1, the following phase criteria can be used in the NDZ analysis of the SFS method [69]:

$$R(\frac{1}{\omega_s L} - \omega_s C) = -\tan(\frac{\pi}{2}(cf_0 + K_f(\omega_s - \omega_0))) \tag{6.1}$$

where the radian frequency of the islanded system is ω_s. Equation (6.1) can be also rewritten as [70]

$$Q_f(\frac{f_r}{f_s} - \frac{f_s}{f_r}) = -\tan(\frac{\pi}{2}(cf_0 + 2\pi K_f(\omega_s - \omega_0))) \tag{6.2}$$

where the frequency f_r is the resonant frequency of the RLC load; the frequency f_s is the islanded system frequency, and the frequency f_0 is the grid frequency. The NDZ of the SFS method is acquired by changing the quality factor Q_f and calculating the frequency f_r from Equation (6.2). The frequency f_s is selected as the upper or lower frequency relay limit. The resistance of the RLC load is set as the value which makes the imbalance active power P_N zero in Figure 2.1. As a result, the DG terminal voltage changes will be very small before and after the islanding, so the effect of the voltage relays can be excluded. Figure 6.1 shows the illustrated NDZ of the SFS method applied to the single inverter-based DG system. The inverter is constant current-controlled. For a selected Q_f, if the resonant frequency of the RLC load is higher than f_r on the $Q_f - f_r$ curve of $f_s = 60.5Hz$ or lower than f_r on the curve of $f_s = 59.3Hz$, the steady-state frequency of the islanded DG system will be out of the limits of the frequency relays, and the DG will be tripped. Thus, the region under the $f_s = 60.5Hz$ curve and over the $f_s = 59.3Hz$ curve forms the NDZ of the SFS method with the fixed setting of cf_0 and K_f. Figure 6.1 reveals that no such area is present in the left plane of the vertical line crossing point **A**. That is to say, the NDZ does not exist when the quality factor Q_f is smaller than some value. This finding is usually explained by stating that when the quality factor of the RLC load is small, the islanding can be easily detected, and no NDZ for SFS is present under

these conditions. Although this explanation has been demonstrated by experiments, it has no theoretical justification [44]. In order to clarify the problem theoretically, small-signal analysis is used in this section to study the islanded DG system.

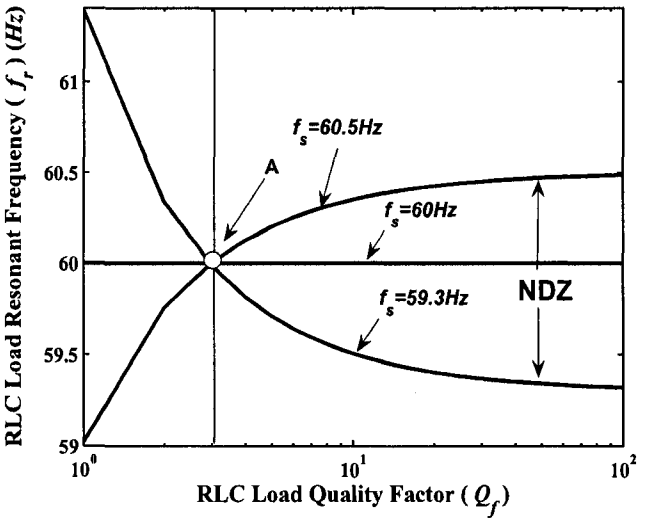

Figure 6.1: NDZ of the SFS method acquired by phase criterion for single inverter

Small-signal analysis has been utilized in [86] and [87] for the islanding study of single-phase utility-connected photovoltaic inverters. In this chapter, the modal analysis method is extended to three-phase inverters to investigate the islanding characteristics of DG systems with a positive feedback anti-islanding scheme. Figure 6.2 shows the change in the grid-connected DG system after being island. The small-signal analysis of Figure 6.2(a) was presented in the previous chapters to study the impact of the positive feedback control on the operation stability of the DG system when it is connected to the grid. If the the circuit breaker CB in the subfigure is open for some reason, the DG system will be operated as the system shown in Figure 6.2(b). The aim of the small-signal analysis of the islanded DG system is to check if the DG system can maintain the island's small-signal stability under the perturbation of the positive feedback anti-islanding control. If the islanded DG system is unstable, the islanding phenomenon will be detected successfully. However, if the current or power regulators of the inverter can defeat the anti-islanding control within the island, the

DG unit probably will not be tripped after islanding.

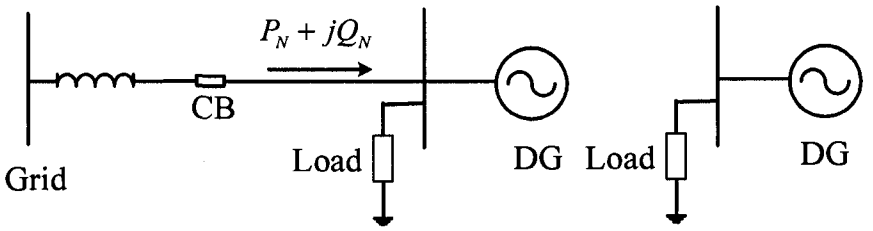

(a) Grid-connected DG system (b) Islanded DG system

Figure 6.2: DG system subsequent to island

Strictly speaking, islanding is a large-signal state for the DG system. Thus, the transient stability method can be most accurately used to study the dynamic response of the DG system after it has been islanded. However, if the imbalance power ($P_N + jQ_N$ in Figure 6.2(a)) between the grid and the DG system is small before the islanding, the operating point of the DG system will not change much after the islanding. As we know from Chapter 2, if $P_N + jQ_N$ is considerable, the islanded DG system voltage or frequency will drift out of the limits of the voltage or frequency relays even without the help of the positive feedback control. In this situation, the NDZ of the positive feedback anti-islanding methods does not have to be studied. It needs to be studied only when $P_N + jQ_N$ is small enough to cause the relays to fail. At this time, small-signal analysis can be employed as the islanding is like a small-signal disturbance to the DG system in this case.

The small-signal model of the islanded DG system can be easily obtained based on the analytical models presented in Chapter 3. The eigenvalues of the model provide the basis for the small-signal stability analysis of the islanded DG system. When we change the parameters of the islanded system, different root loci can be acquired. Figure 6.3(a) shows the root loci of the DG system when the quality factor Q_f is decreased from 4 to 1. The DG parameters settings are the same as those in Table E.1. The resistance of the RLC load is set as $4.32\Omega(10p.u.)$, which meets the active power output of the DG. (The inverter output reference current is $0.1p.u.$.) The

frequency f_s defined in Equation (6.2) is $60.5Hz$. Figure 6.3(a) reveals when the quality factor is reduced, a critical eigenvalue λ_1 movies from the left half-plane to the right half-plane, which means the islanded DG system will lose its small-signal stability when Q_f is below some limit. The result shows that this limit matches the value of Q_f at point **A** in Figure 6.1. Based on this analysis, we can conclude that the NDZ is not present in Figure 6.1 because the positive feedback causes the instability of the islanded system under some circumstances. The islanded DG system can reach a new steady state if the quality factor Q_f is higher than this limit, and the NDZ will appear when the frequency f_s is located within the range of frequency relays under this premise.

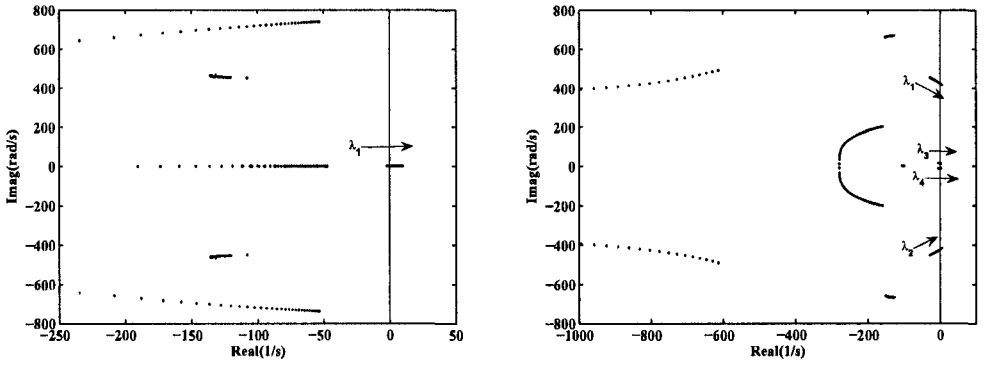

(a) Constant current control (b) Constant power control

Figure 6.3: Root Loci of the islanded single DG system

Small-signal analysis provides the dynamic information about the islanded DG system and explains the non-existence of the SFS NDZ theoretically. One important application of this method is that it is suitable for the NDZ study of the constant power-controlled inverters. When the SFS method is applied to these inverters, the steady state of the islanded system will have the following characteristic:

$$R(\frac{1}{\omega_s L_L} - \omega_s C_L) = \frac{Q_{DG}}{P_{DG}} \tag{6.3}$$

If the inverter reactive power Q_{DG} is controlled as zero, then the steady-state frequency of the islanded system will be the resonant frequency of the RLC load. The impact of the positive feedback on the NDZ cannot be exhibited from this steady-state analysis. With small-signal analysis, the stability limit of the islanded DG system can be acquired. Figure 6.3(b) shows the root loci of the constant power-controlled DG system after islanding. The DG parameter settings are the same as those in Figure 6.3(a) except for $P_{ref} = 0.1p.u.$ and $Q_{ref} = 0p.u.$. The quality factor of the RLC load is changed from 0.5 to $0.2p.u.$. Figure 6.3(b) displays that two pairs of conjugate eigenvalues move from the left half-plane to the right half-plane during this process. The critical Q_f value is 0.27, which is much smaller than that in Figure 6.3(a). The comparison indicates that constant current-controlled inverters are more easily disturbed by the positive feedback control.

Figure 6.4 exhibits the NDZs of the SFS method for the two inverter interface controls. For the constant power-controlled inverter, each RLC resonant frequency f_r, which is equal to the islanded system steady-state frequency f_s, is related to a critical Q_f value through the small-signal stability analysis. Then the NDZ of the constant power-controlled inverter (**Area A** plus **Area B** in the figure) can be formed if the load resonant frequency varies between the frequency relay limits ($59.3Hz$ and $60.5Hz$). For the constant current-controlled inverter, small-signal analysis and the phase criteria are used together to find the critical Q_f value and the NDZ of the SFS method. The NDZ of the constant current-controlled inverter is covered by **Area B**, which is much smaller than that of the constant power-controlled DG. Thus, the SFS anti-islanding method is more effective for the constant current-controlled inverters.

Figure 6.4 also reveals that for the constant power-controlled inverters when the quality factor of the RLC load is greater than the critical Q_f value at some f_s setting, the islanded DG system will be stable, and the NDZ of the SFS method will be the same as that of the frequency relays for this scenario. Only if the RLC load has a quality factor smaller than the critical Q_f value, can the SFS anti-islanding method display its advantages over the passive frequency relays. The positive feedback

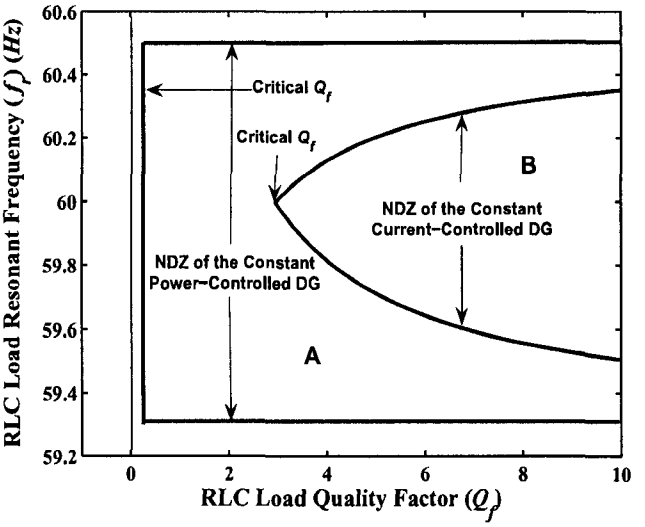

Figure 6.4: NDZs of the SFS method ($K_f = 0.01, cf_0 = 0$)

will destabilize the islanded DG system, and the islanding frequency will collapse eventually in this scenario. However, the critical Q_f value is usually small and makes the SFS method not sensitive to the constant power-controlled inverters. This result also demonstrates that the SFS anti-islanding method is more effective for the constant current-controlled inverters.

6.2 Key Factors Affecting the Non-Detection Zones

By using a small-signal model, the sensitivity analysis of the factors affecting the performance of the positive feedback anti-islanding scheme can be investigated. The impact of the positive feedback gain and the initial chopping fraction on the NDZs of the SFS method are studied in this section.

6.2.1 Positive Feedback Gain

Positive feedback gain determines the strength of the SFS method. The larger the gain is, the more effective the anti-islanding scheme is. However, a higher Q_f of the RLC load will hinder the islanding detection as a higher Q_f will make the

islanded system more stable. The concept of positive feedback gain versus quality factor ($K - Q_f$) curve is proposed here to express the relationship between these two factors. The curve is acquired by calculating the critical Q_f value by using the eigenvalue analysis for each K_f. Figure 6.5 displays such $K-Q_f$ curves at different R_L levels for the constant current-controlled inverter. For each R_L, the inverter output current is set to satisfy the load active power consumption before the islanding. Figure 6.5 shows that the RLC load level has no influence on the $K - Q_f$ curve if the power $P_N = 0$ in Figure 2.1. Figure 6.5 also reveals the proportional relationship between K_f and Q_f. The strong positive feedback gain can destabilize the islanded DG system easily even when the RLC load has a relatively large quality factor. The constant power-controlled inverter has a similar characteristic; however, its critical Q_f value will be much smaller if the values of K_f are the same for these two inverters.

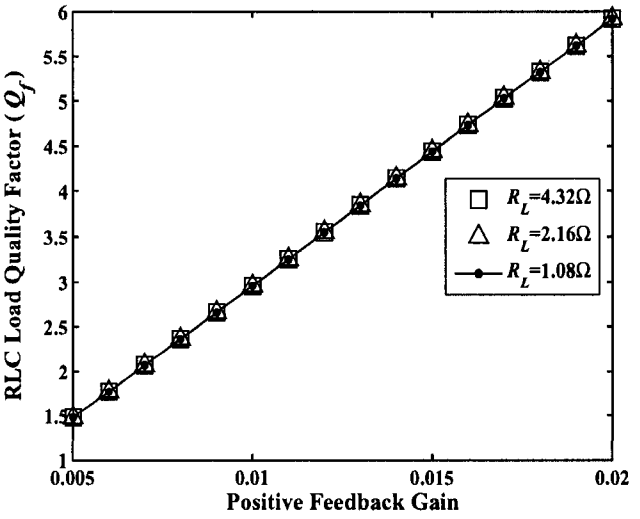

Figure 6.5: $K - Q_f$ curves of the SFS method ($cf_0 = 0, f_s = 60.5Hz$)

6.2.2 Initial Chopping Fraction

The initial chopping fraction will alter the NDZ of the SFS method for the constant current-controlled inverter. Figure 6.6 shows the drift of the NDZ when the initial chopping fraction cf_0 is changed. Point **A** moves vertically with the varying of cf_0.

The *RLC* load resonant frequency is quite different at point **A**, **A'** and **A"**. However, the critical Q_f value at these points almost does not change with cf_0. Figure 6.7, where the initial chopping fraction cf_0 has no detectable influence on the $K - Q_f$ curve of the anti-islanding method when the positive feedback gain K_f is small, also demonstrates this point. The figure reveals that a high K_f will cause the obvious difference.

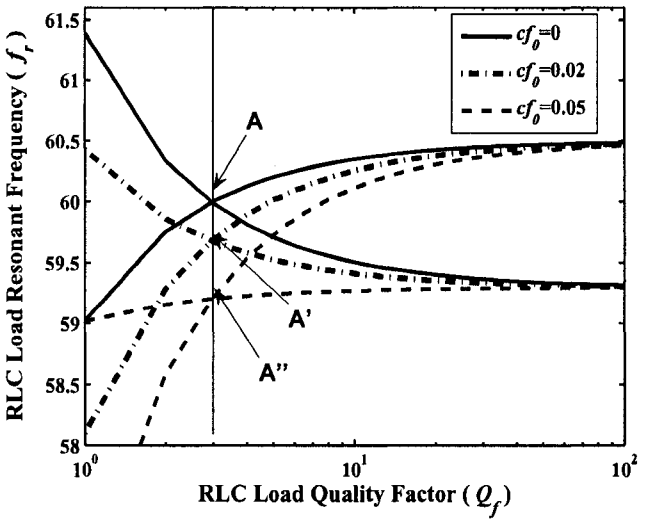

Figure 6.6: SFS NDZs affected by $cf_0(K_f = 0.01)$)

Given the results from Figures 6.6 and 6.7, one can say that the area of the NDZ of the SFS scheme will not be greatly affected by cf_0 for a small K_f. However, cf_0 does change the NDZ position notably in the load parameter space for the constant current-controlled inverter. Further study indicates that the chopping fraction has no influence on the NDZ of the constant power-controlled inverter.

6.3 Non-Detection Zones of SFS for Multiple Inverters

Usually, an inverter-based DG unit has a small capacity, and multiple DGs are often operated in parallel or installed along the distribution line to supply the local load.

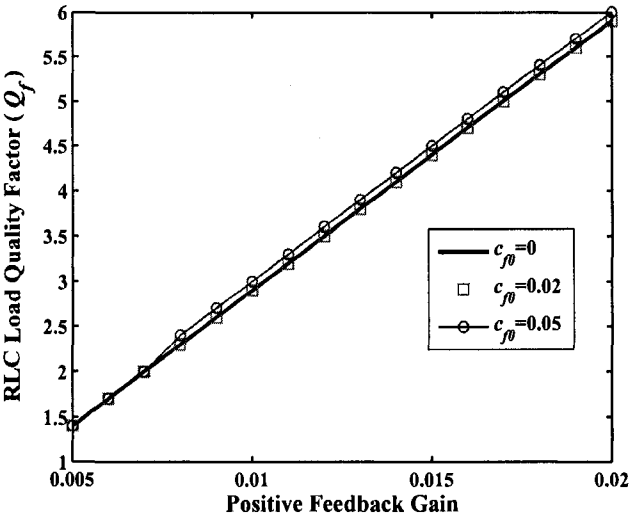

Figure 6.7: $K - Q_f$ curves with different cf_0 ($R_L = 4.32\Omega, i_{dref} = 0.1p.u., i_{qref} = 0p.u., f_s = 60.5Hz$)

For these situations, the inverters may have different anti-islanding schemes. Even if they are equipped with the same scheme, its parameter settings may be different. The inverters could interact because of either the incompatibility of the various anti-islanding schemes or the disharmony of the diverse settings of one scheme. As well, the overall anti-islanding performance can also be degraded in the multi-inverter case. This section investigates the anti-islanding interaction among the multiple inverters when they are configured with the SFS method. Figure 6.8 illustrates the operation of multiple grid-connected inverters in parallel. For simplification and demonstration of the interaction, two DG units are used in the studies. The conclusions drawn from the investigation can be extended to more than two inverters.

In Figure 6.8, the two DG units both have the SFS anti-islanding control and are connected to the common DG terminal. As a result, the two inverters utilize the same voltage information for the frequency positive feedback control. DG1 has the output power $P_1 + jQ_1$, and its output current is $I_1\angle\delta + \theta_{f1}$. DG2 has the output power $P_2 + jQ_2$, and its output current is $I_2\angle\delta + \theta_{f2}$. The angles θ_{f1} and θ_{f2} are the positive feedback signals for the two DG units. When the islanding occurs,

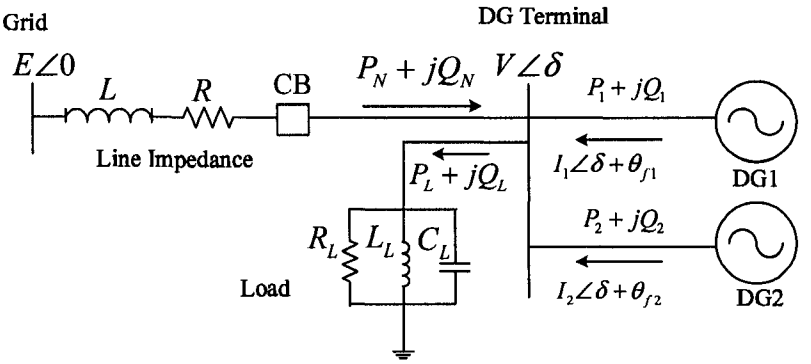

Figure 6.8: Schematic diagram of multiple inverters operated in parallel

the two inverters have two positive feedback paths with the same input (i.e., the same DG terminal voltage frequency). Thus, they will interact with each other after the islanding, and the interaction could affect the performance of the anti-islanding scheme. In addition, if the inverters have different interface controls, the interaction will be more sophisticated.

If we assume that DG1 and DG2 have the positive feedback parameters K_{f1}, cf_{01} and K_{f2}, cf_{02}, respectively, and that both of them are all constant current-controlled, then the phase criterion of the DG system will be

$$Q_f(\frac{f_r}{f_s} - \frac{f_s}{f_r}) = -\frac{I_1 \sin\theta_{f1} + I_2 \sin\theta_{f2}}{I_1 \cos\theta_{f1} + I_2 \cos\theta_{f2}} \tag{6.4}$$

where

$$\theta_{f1} = \frac{\pi}{2}(cf_{01} + 2\pi K_{f1}(f_s - f_0)) \tag{6.5}$$

$$\theta_{f2} = \frac{\pi}{2}(cf_{02} + 2\pi K_{f2}(f_s - f_0)) \tag{6.6}$$

Equation (6.4) provided the affecting weight of each DG unit on the phase criterion. If the two generators have the same output current (i.e., $I_1 = I_2$), and their positive feedback control parameter settings are also equal to each other (i.e., $\theta_{f1} = \theta_{f2}$), then

Equation (6.4) is no different from the phase criterion equation of a single inverter, so that the SFS method, when applied to identical multiple DG units, is as effective as it is when applied to a single DG unit. The small-signal analysis of the multi-DG system also reveals that the critical Q_f value does not change in the above scenario. Furthermore, if $\theta_{f1} = \theta_{f2}$, then the phase criterion will not be affected no matter how much the ratio of I_1/I_2 changes. Figure 6.9 shows the changes of the SFS NDZ when the two inverters have different positive feedback gains or initial chopping fractions. $I_1 = I_2$, and the total active power output of the two generators is well balanced by the resistance of the RLC load before the islanding (i.e., $P_N = 0$). The other parameter settings of the inverters are the same as those in Table E.1.

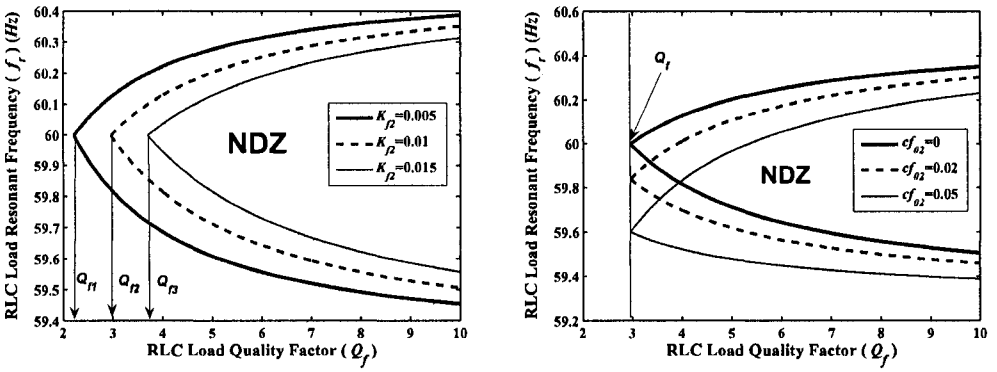

(a) $K_{f1} = 0.01, K_{f2}$ changes, $cf_{01} = cf_{02} = 0$ (b) $K_{f1} = K_{f2} = 0.01, cf_{01} = 0, cf_{02}$ changes

Figure 6.9: DG system subsequent to island

Figure 6.9(a) reveals that the NDZ shrinks with the increasing of K_{f2} and drifts with the changing of cf_{02} in Figure 6.9(b). The area of the NDZ is not changed in Figure 6.9(b). Obviously, the sum of the positive feedback strengths determines the anti-islanding performance of the SFS scheme in this multi-inverter case.

The above analysis is based on the assumption that all the inverters are constant-current controlled. However, in some situations, the inverters may have different interface controls. If DG1 in Figure 6.8 is constant current-controlled, and DG2 is constant power-controlled, the phase criterion will be decided by the following

equations:

$$\frac{V^2}{R_L} = VI_1 \cos\theta_{f1} + P_2 \tag{6.7}$$

$$V^2(\frac{1}{\omega_s L_L} - \omega_s C_L) = -VI_1 \sin\theta_{f1} + Q_2 \tag{6.8}$$

By solving Equation (6.7), the DG terminal voltage V can be obtained:

$$V = R_L \frac{I_1 \cos\theta_{f1} + \sqrt{I_1^2 \cos^2\theta_{f1} + 4P_2/R_L}}{2} \tag{6.9}$$

If $Q_2 = 0$, then the new phase criterion is expressed as

$$Q_f(\frac{f_r}{f_s} - \frac{f_s}{f_r}) = -\frac{R_L I_1 \sin\theta_{f1}}{V} = -\frac{2I_1 \sin\theta_{f1}}{I_1 \cos\theta_{f1} + \sqrt{I_1^2 \cos^2\theta_{f1} + 4P_2/R_L}} \tag{6.10}$$

Equation (6.10) alone is not enough to obtain the NDZ as this equation does not include the impact of the DG2 positive feedback. Small-signal analysis must be used to obtain the critical Qf value of the multi-DG system at first, and then the NDZ can be plotted by using Equation (6.10). Figure 6.10 compares the NDZs of the two cases with different inverter interface controls.

In the first case, two constant current-controlled inverters are used in Figure 6.8. The inverters have the settings of $I_1 = I_2 = 0.05p.u., K_{f1} = K_{f2} = 0.01$ and $cf_{01} = cf_{02} = 0$. The resistance R_L is set to make the mismatch power P_N zero. The NDZ of this case is the NDZ1, and the critical Q_f value is Q_{f1} in Figure 6.10. In the second case, one inverter is constant current-controlled, and the other is constant power-controlled. The DG parameter settings are $I_1 = P_2 = 0.05p.u., K_{f1} = K_{f2} = 0.01$ and $cf_{01} = cf_{02} = 0$. The value of R_L is not changed. The NDZ and the critical Q_f value are changed to NDZ2 and Q_{f2} in the figure. The comparison between NDZ1 and NDZ2 reveals that the effectiveness of the anti-islanding scheme has been discounted

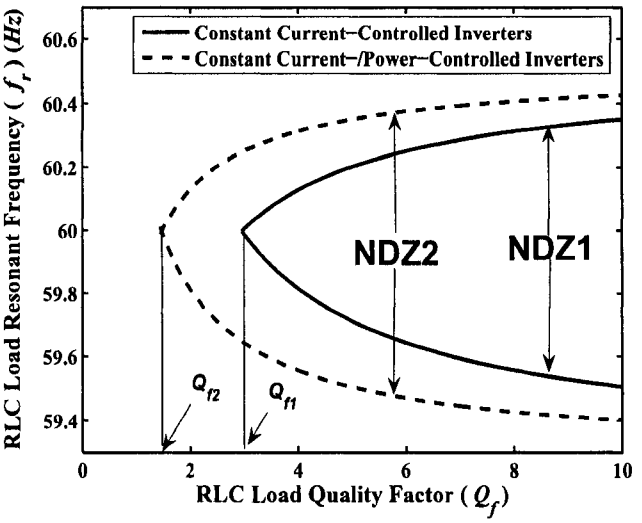

Figure 6.10: Impact of the interface controls on the NDZ of the multiple inverters

in the second case. Figure 6.11 shows the changes of the critical Q_f value for the second case when the ratio of I_1/P_2 is varied. The sum of I_1 and P_2 is maintained as constant $0.1p.u.$ to make $P_N = 0$ in Figure 6.8. This figure reveals that when the contribution of the constant power-controlled inverter is high the critical Q_f value will be small, so that the area of the NDZ will be large.

6.4 Key Factors Affecting the Islanding Detection Time

Another important index for the performance evaluation of anti-islanding methods is the islanding detection time, which is described as the time from the beginning of the islanding to the instant when the islanding is detected. An efficient anti-islanding method should have a short detection time. The small-signal analysis method provides a convenient and accurate way to determine the NDZs of a positive feedback anti-islanding scheme. However, this method cannot be used to obtain the islanding detection time information. That is to say, we know if the islanding will be detected but we do not know when it will be detected through modal analysis. In order to acquire all the details of the islanding process, EMTP simulations are necessary. In

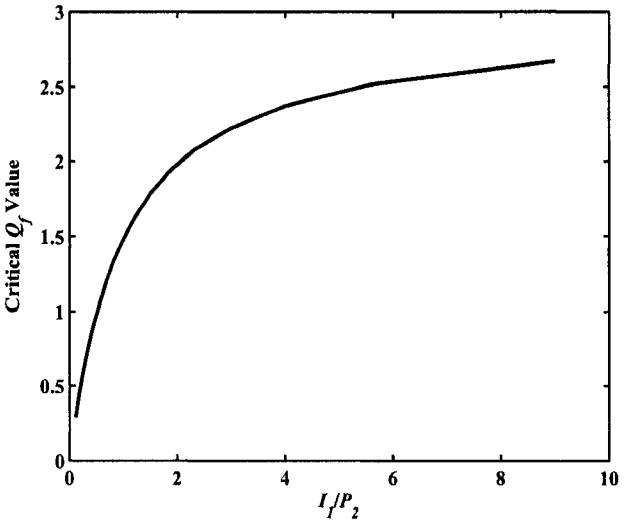

Figure 6.11: Changes of the critical Q_f value with I_1/P_2 for constant current-/power-controlled inverters

Chapters 4 and 5 we discussed the conflict problem between the DG units' stability and islanding detection capability, and the impact of positive feedback gains on DG islanding detection time was investigated through EMTP simulations. This section continues the study of the DG islanding detection time by focusing on anti-islanding protection. The factors, such as load characteristics and inverter interface controls, affecting DG islanding detection time are the main focus.

6.4.1 Load Quality Factor

Figure 6.12 displays the islanded DG system frequency change for different *RLC* load Q_f settings for the single DG system shown in Figure 2.1. The inverter is constant current-controlled. The islanding occurs at $0.3s$. The steady-state frequency of the islanded DG system f_s is set as $60.3Hz$(assume the positive feedback control does not destabilize the islanded DG system). According to the small-signal analysis, the system will be unstable after the islanding if the quality factor Q_f is smaller than 3 based on the K_f setting (0.01). Figure 6.12 reveals that when the value of Q_f is 2.9 which is close to stability limit value, the DG frequency will take a long time to lose its stability. Although the DG will be tripped finally in this scenario, the use of

anti-islanding protection is not practical as the islanding detection time is too long. However, if the quality factor Q_f is much smaller than the stability limit, the DG frequency will be turned over in a short time, as the scenario of $Q_f = 2.5$ shows. For a Q_f larger than the limit, the islanded DG system will go to another steady state, and the DG frequency will be equal to f_s eventually. If the frequency f_s is located outside of the frequency limits, then the islanding can also be detected, and the islanding detection time is also affected by the value of Q_f.

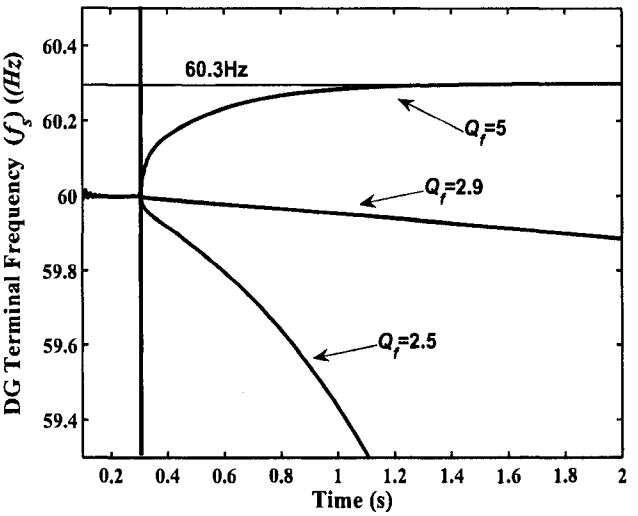

Figure 6.12: Islanded DG system frequency for different Q_f ($f_s = 60.3Hz$, $K_f = 0.01$, $cf_0 = 0$, $R_L = 10p.u.$, $I_{ref} = 0.1p.u.$)

Figure 6.13(a) shows the RLC load quality factor versus the islanding detection time curves of different K_f for the unstable islanded DG system scenario. The frequency relay limits are $59.3Hz$ and $60.5Hz$. The comparison indicates that the islanding detection time is reduced with the decreasing of Q_f and the increasing of K_f. For the stable islanded DG system scenario where the value f_s is set as $60.6Hz$, the RLC load quality factor versus the islanding detection time curves are displayed in Figure 6.13(b). Unlike the islanding detection time in the unstable scenario, the islanding detection time is reduced with the increasing of Q_f and the decreasing of K_f in this figure. The frequency responses of the two scenarios are displayed in Figure

6.14. Figure 6.14(a) shows that the DG frequency will be unstable after the islanding when the quality factor Q_f is small. The larger K_f causes a faster decay of the frequency because the strong positive feedback speeds up the instability. However, for the stable scenario shown in Figure 6.14(b), the DG frequency goes to steady state faster with the smaller the K_f. As a result, the time needed for the frequency to pass the frequency limit $60.5Hz$ is shorter than that for the larger K_f. In other words, for the stable case, the strong positive feedback delays the recovery time of the DG frequency and extends the islanding detection time when the islanding steady-state frequency is over the frequency relay limit.

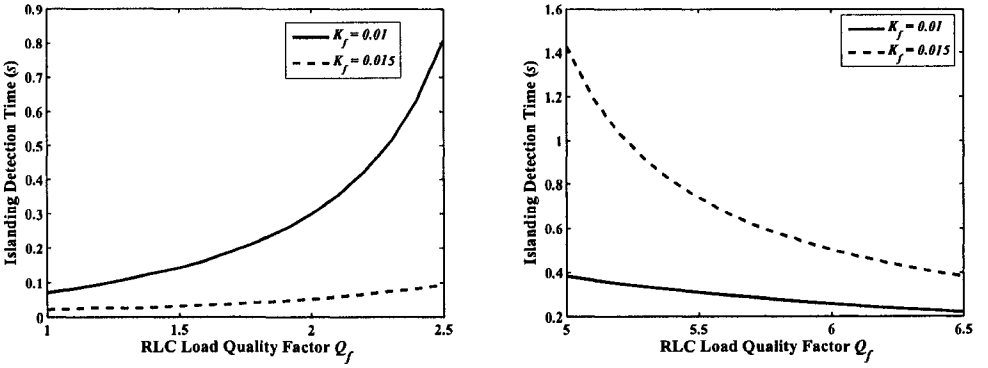

(a) unstable islanded DG system (b) stable islanded DG system

Figure 6.13: Islanding detection time of the SFS method ($f_s = 60.6Hz$, $cf_0 = 0$, $R_L = 10p.u.$, $I_{ref} = 0.1p.u.$

Figure 6.15 displays the simulation results of the $Q_f - t$ curves for the multi-DG system shown in Figure 6.8. In Figure 6.15(a), DG1 and DG2 are both constant current-controlled, and the positive feedback strength of DG1 is fixed (i.e., $K_{f1} = 0.01, cf_{01} = 0$). K_{f2} and cf_{02} are changed to observe the impact of DG2 on the islanding detection time. Q_f is in the range where the DG system will lose its stability after the islanding. The subfigure reveals that a large K_{f2} reduces the islanding detection time greatly. However, the change of cf_{02} has almost no influence on the islanding detection time because the curve with $K_{f2} = 0.01$, $cf_{02} = 0$ and the curve with $K_{f2} = 0.01, cf_{02} = 0.05$ are not significantly different. Also, the

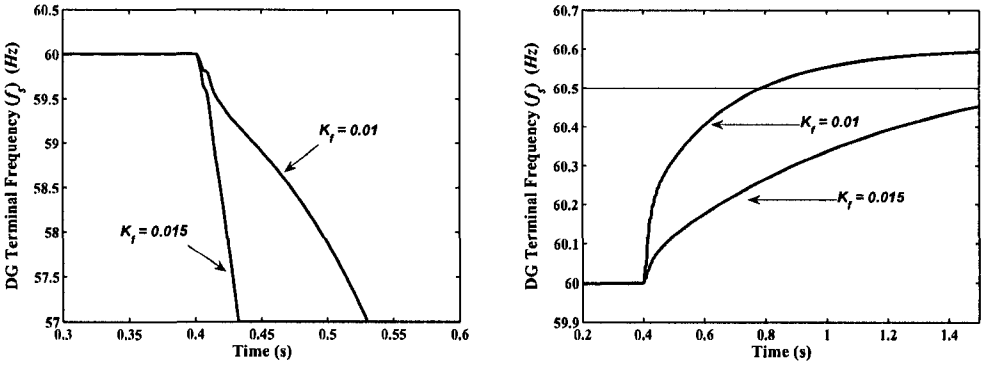

(a) $Q_f = 1, f_s = 60.6Hz$ (b) $Q_f = 5, f_s = 60.6Hz$

Figure 6.14: DG terminal frequency responses after the islanding

curve with $K_{f2} = 0.015, cf_{02} = 0$ and the curve with $K_{f2} = 0.015, cf_{02} = 0.05$ are coincident. Figure 6.15(b) shows the $Q_f - t$ curves plotted for the cases in which the DG system can maintain its stability after the islanding. Unlike the phenomenon in Figure 6.15(a), a large K_{f2} increases the islanding detection time here, and cf_{02} has an observable influence when the value of K_{f2} is 0.015. A high cf_{02} will delay the islanding detection of the multi-DG system.

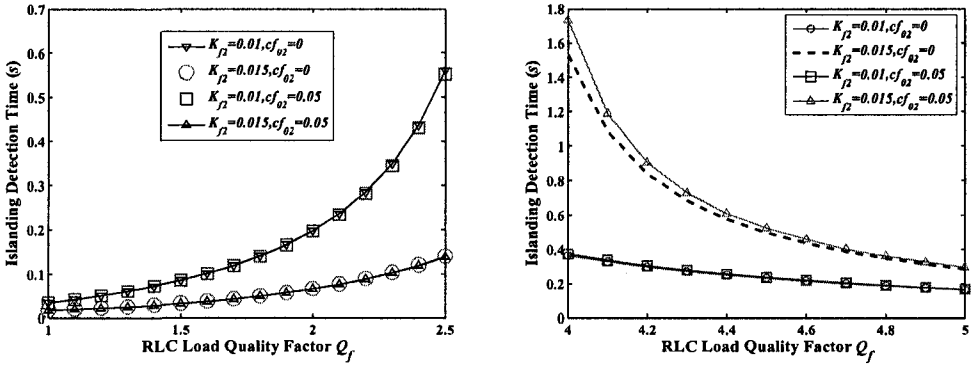

(a) unstable islanded DG system (b) stable islanded DG system

Figure 6.15: Islanding detection time of the SFS method for multiple inverters ($I_1 = I_2 = 0.05p.u., R_L = 10p.u., f_s = 60.8Hz$)

6.4.2 Inverter Interface Controls

The inverter interface controls will also affect the dynamics of the islanded DG system. Figure 6.16 compares the frequency changes of the constant current-controlled and the constant power-controlled inverters after the islanding. Figure 6.16(a) reveals that an overshoot occurs for the constant power-controlled inverter frequency curve. When the steady-state islanding frequency is $60.5Hz$, which is the upper limit of the frequency relays, the constant power-controlled inverter will exceed this limit in a short time and then fall down to $60.5Hz$. However, the constant current-controlled inverter frequency will require a relatively long time to increase to the frequency limit and then stay there. Thus, if the dynamic process is considered when obtaining the islanding detection time, the constant power-controlled inverter will be more efficient than the constant current-controlled inverter for this case. However, when the quality factor Q_f is small enough to make the islanded DG system unstable, the constant current-controlled inverter has the better islanding detection performance. Figure 6.16(b), where the DG frequency collapses quickly for the constant current-controlled inverter, demonstrates this point.

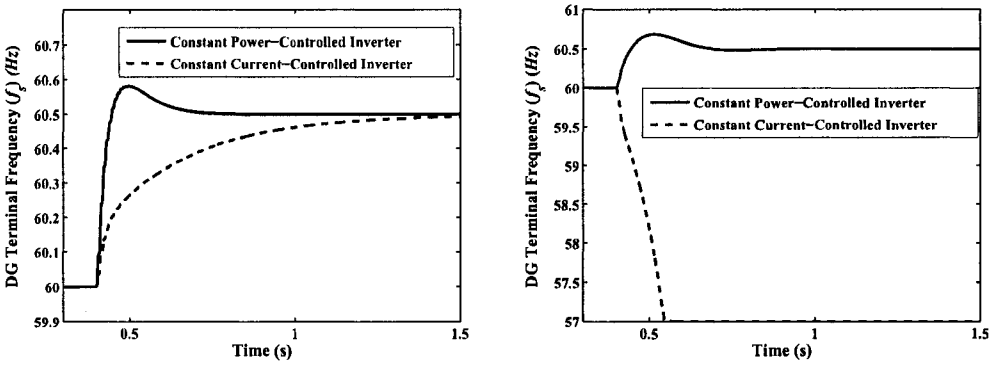

(a) $Q_f = 5, f_s = 60.6Hz$ (b) $Q_f = 1, f_s = 60.6Hz$

Figure 6.16: Impact of the inverter interface controls on the dynamics of the islanding ($K_f = 0.01, cf_0 = 0$)

For the situations where the inverters have hybrid interface controls, the constant power-controlled inverter not only changes the NDZ of the SFS method but also

affects the DG system transient performance when the DG system transfers from the grid-connected mode to the islanding operation mode (see Figure 6.17(a)). When the two inverters in Figure 6.8 are both constant current-controlled, the DG system frequency will gradually increase and reach the steady-state frequency ($60.5Hz$) at the instant of t_2 after the islanding occurs at $0.4s$. However, if one inverter is constant current-controlled, and the other one is constant power-controlled, the DG system frequency will increase sharply after the islanding and reach the steady state at t_1. The introduction of the constant power-controlled inverter into the multiple DG system reduces the period of the transient process. However, the opposite result occurs in Figure 6.17(b) where the Q_f of the RLC load is small, and the positive feedback of the SFS anti-islanding method destabilizes the DG system after the islanding. This subfigure reveals that the constant power-controlled inverter delays the collapse of the DG frequency.

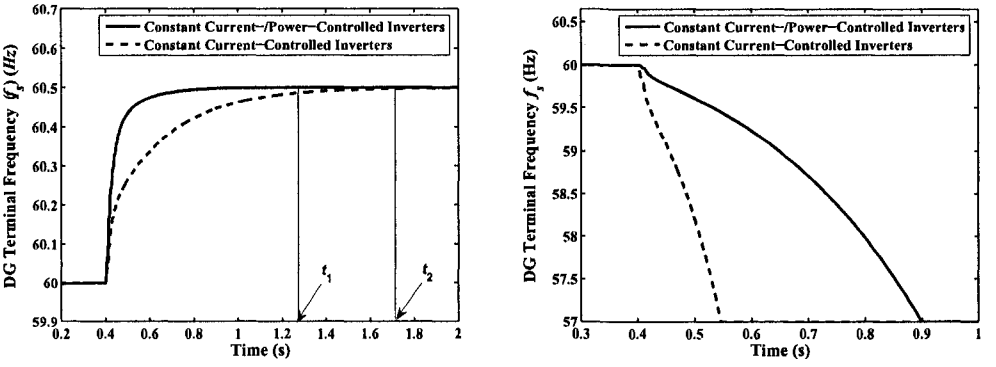

(a) stable islanded DG system ($Q_f = 5$) (b) unstable islanded DG system ($Q_f = 1$)

Figure 6.17: Influence of the constant power controller on the transient performance of the multi-DG system

6.5 Summary

The conventional performance evaluation methods for DG anti-islanding schemes focus on only the steady state of the islanded DG systems. The dynamic process of the island formation is not considered in these methods, so that their assessment of DG anti-islanding protection is incomplete. In this chapter, the small-signal analysis

method, which provides the stability information for an islanded DG system, is utilized together with the steady-state phase criteria method to study the NDZs of the positive feedback anti-islanding methods for inverter-based DGs. By this means, the phenomenon of the non-existence of NDZ for the positive feedback anti-islanding methods under some conditions can be analytically explained. The impact of different inverter interface controls on the NDZ of the investigated anti-islanding method can also be analytically determined. Additionally, in view of the efficiency of the estimated anti-islanding method, electromagnetic transient simulations are conducted to obtain the anti-islanding method's islanding detection time, which reveals how fast an island can be recognized. The key factors affecting the islanding detection time of the islanded DG system are also investigated. The following main conclusions are reached in this chapter:

- For a given single DG system with the parallel RLC load, each positive feedback gain of the SFS method is related to a critical quality factor Q_f. If the load quality factor is smaller than the critical Q_f, the DG system will lose its stability after the islanding with the corresponding positive feedback gain setting. At this time, the islanding will be absolutely detected and the NDZ of the anti-islanding method will not exist. Otherwise, the islanded DG system will be stable eventually, and the NDZ can be formed based on the resonant frequency of the RLC load. The initial chopping fraction of the SFS method will not change the area of the NDZ but it will alter the shape of the NDZ.

- The small-signal analysis method can be used to acquire the NDZ of the SFS method when the former method is applied to the constant power controlled-inverters while the steady-state methods cannot be used to do so. A constant power-controlled inverter has a larger NDZ than a constant current-controlled inverter when they work individually with the frequency positive feedback anti-islanding control.

- When multiple inverters equipped with the SFS control are operated in parallel, their islanding effect is decided by the aggregate positive feedback strength.

Constant power-controlled inverters will degrade the overall anti-islanding performance of the multiple inverters if they are installed together with constant current-controlled inverters.

- The stronger positive feedback gains will cause a shorter islanding detection time when the islanded DG system loses its stability after the islanding. However, the opposite conclusion will occur if the islanded DG system is stable after the islanding.

Chapter 7

Conclusions and Future Work

7.1 Conclusions

The positive feedback anti-islanding scheme has been recognized as one of the most effective methods for inverter-based DG anti-islanding protection. Various derivatives of the scheme have been widely applied to commercial grid-connected inverters. However, there is always the concern that the collective destabilizing force of the positive feedback control could be too significant to be ignored when a large number of inverters are connected to a power system. In addition, the potential interactions among the DG units caused by the positive feedback anti-islanding control are also unclear. In response to these challenges, this thesis developed a set of analytical and simulation tools for inverter-based DG anti-islanding studies and investigated the impact of the positive feedback anti-islanding scheme on interconnected inverter-based DG systems. The islanding detection performance of the scheme was evaluated based on the proposed concepts and methods. The investigation results provide meaningful guidance for inverter-based DG anti-islanding protection. The main contributions and conclusions of this research are summarized as follows:

- In view of the variety of the available anti-islanding schemes involving inverter-based DGs, this thesis carried out a thorough survey to select the representative anti-islanding scheme with the most significant potential impact on power systems. Based on the literature review results, the positive feedback anti-islanding scheme was chosen for studying, and it was found that little theoretical work had been done on the issues addressed by this thesis.

- Small-signal models of the grid-connected inverters and the positive feedback anti-islanding methods were developed to provide the analytical tools for inverter-based DG anti-islanding studies. The SFS method was selected as the representative positive feedback anti-islanding method for the analysis and was extended from single-phase systems to three-phase systems. An extensive comparison between the small-signal model responses and the simulation results of the electromagnetic transient models showed that the small-signal models accurately predicted the performance of the transient models.

- Based on the small-signal models of the inverter-based DG systems, a comprehensive analysis of the impact of positive feedback anti-islanding scheme on the stability of inverter-based DG systems was conducted. The concept of DG power transfer limit versus the positive feedback gain ($P - K$) curve was introduced to determine and analyze the stability limit of the DG systems. The systematic approach was applied to both single DG systems and multi-DG systems. It was concluded that strong positive feedback anti-islanding control will destabilize the grid-connected DG systems when the grid is weak and the DG penetration level is high.

- The conflict problem between the anti-islanding capability of positive feedback anti-islanding scheme and DG system stability was identified. The electromagnetic transient simulation results showed that the anti-islanding control with weak positive feedback gain needed a relatively long time to detect islanding. The tool of the $P - t$ curve was proposed to provide design guidance for the positive feedback gain setting. The curve can also be used as a reference for the optimal placement of multiple DG units in a power distribution system when the issues of stability and anti-islanding protection are dealt with.

- The thesis also clarified the interactions among the multiple inverters due to the positive feedback anti-islanding action. It was found that the single DG unit output power limit was influenced by the anti-islanding controls of the other DG units within the distribution system. The interactions were greatly affected by the location, number and penetration level of the DG units.

- The anti-islanding protection performance of the positive feedback anti-islanding scheme was evaluated from the perspective of dynamics. The modal analysis method used for NDZ analysis overcame the shortcoming of the steady-state analysis method, which is not suitable for constant power-controlled inverters. Additionally, the interactions between the inverter interface controls and positive feedback anti-islanding control were investigated in terms of stability impact, NDZ and islanding detection time. The investigation results indicated that the constant power controller counteracted the destabilizing force introduced by the positive feedback anti-islanding control, but it also decreased the islanding detection performance of the scheme.

Overall, this thesis disclosed the nature and characteristics of positive feedback anti-islanding scheme for inverter-based grid-connected DGs. The analysis methods and conclusions derived from the thesis support the adaptation of inverter-based DG technologies in modern power systems.

7.2 Suggestions for Future Work

In continuation of the work of this thesis, the following topics are suggested for future research:

- With the development of DG technologies, more and more complex inverter interface controls are implemented in inverter controllers. These control strategies coexist with the anti-islanding schemes and they could have significant impact on the performance of the anti-islanding schemes when the operating time of the DG increases. Thus, it is necessary to investigate how these inverter interface controls interact with the anti-islanding controls. The corresponding findings can deliver meaningful results for the improvement of anti-islanding schemes.

- In the NDZ studies for active anti-islanding schemes, the NDZs defined in the power imbalance space($\Delta P - \Delta Q$) and load parameter space ($C_{norm} - L_L$ or $Q_f - f_r$) all have disadvantages. A new space defined by $\Delta P - \Delta Q/Q_C$ can be

used to evaluate the NDZs of active anti-islanding schemes for the situations where there are multiple DGs existing in an distribution system and the load flow at the PCC point of the substation is close to zero. In the new definition, ΔP, ΔQ, Q_C are the active imbalance power, reactive imbalance power and capacitive reactive power of the load, respectively. The proposed work is of significance to evaluate the performance anti-islanding schemes in the multi-DG systems and the DG systems with motor and other non-linear loads.

- In the course of the research, it has been noticed that positive feedback anti-islanding scheme has been applied to synchronous machine based DGs, however, no similar work conducted by this thesis has been done for the rotational machine based DGs. In fact, due to their relatively large size and lack of flexibility in output control, the rotational machine based DGs have become the most challenging type to establish adequate anti-islanding protection. The islanding detection performance issues associated with the rotational machine-based DGs are of interest in the future research.

Bibliography

[1] N. Jenkins, R. Allan, P. Crossley, D. Kirschen and G. Strbac, *Embedded Generation*, Institute of Electrical Engineers, 2000.

[2] N. W. Miller, R. A. Walling and A. S. Achilles, "Impact of distributed resources on system dynamic performance," *IEEE 2001 Transmission and Distribution Conf. Expo.*, vol. 2, Atlanta, GA, USA, 28 Oct.-2 Nov. 2001 pp. 951-952.

[3] B. Verhoeven, "Utility aspects of grid connected photovoltaic power systems," International Energy Agency, Task V IEA-PVPS T5-01, Dec. 1998.

[4] *Standard for interconnecting distributed resources with electric power systems*, IEEE Std. 1547-2003, 2003.

[5] *IEEE recommended practice for utility interface of photovoltaic (PV) systems*, IEEE Std. 929-2000, 2000.

[6] *Measurement and assessment of power quality characteristics of grid connected wind turbines*, IEC Std. 61400-21, 2001.

[7] *Photovoltaic (PV) systems - characteristics of the utility interface*, IEC Std. 61727, 1995.

[8] *Standard for static inverters and charge controllers for use in photovoltaic power systems*, UL Std. UL1741, 1999.

[9] *Wind energy conversion systems (WECS) - interconnection to the electric utility*, Canadian Standards Association, CAN/CSA F418-M91, 1991.

[10] W. Xu, K. Mauch and S. Martel, "An assessment of distributed generation islanding detection methods and issues for Canada," report # CETC-Varennes 2004-074 (TR), CANMET Energy Technology Centre - Varennes, Natural Resources Canada, Jul. 2004, 47 pages.

[11] W. Bower and M. E. Ropp, "Evaluation of islanding detection methods for photovoltaic utility-interactive power systems," International Energy Agency, Task V IEA-PVPS T5-09, Mar. 2002.

[12] R. Jones, T. Sims and A. Imece, "Investigation of potential islanding of dispersed photovoltaic systems," Sandia National Laboratories report SAND87-7027, Sandia National Laboratories, Albuquerque, NM, 1988.

[13] H. Kobayashi, K. Takigawa and E. Hashimoto, "Method for preventing islanding phenomenon on utility grid with a number of small scale PV Systems," *Proceedings of the 21st IEEE Photovoltaic Specialists Conference*, pp. 695-700, 1991.

[14] M. Xu, R. V. N. Melnik and U. Borup, "Modeling anti-islanding protection devices for photovoltaic systems," *Renewable Energy*, vol. 29, no. 15, pp. 2195-2216, Dec. 2004.

[15] M. E. Ropp, M. Begovic and A. Rohatgi, "Prevention of islanding in grid-connected photovoltaic systems," *Progress in Photovoltaics: Research and Applications 7*, pp. 39-59, 1999.

[16] H. Kobayashi, K. Takigawa, E. Hashimito, A. Kitamura and H. Matsuda, "Problems and countermeasures on safety of utility grid with a number of small-scale PV systems," *The Twenty First Photovoltaic Specialists Conference*, vol. 2, pp. 850-855, 21-25 May 1990.

[17] T. Mizuno, T. ishikawa, Y. Noda, H. Koizumi, K. Kurokawa, Y. Arai, N. Goshima, M. Kawasaki and H. Kobayashi, "The islanding detection algorithm of a new AC module for grid connection in Japan," *Proceeding of PV In Europe*, pp. 703-706, Oct. 2002.

[18] T. Mizuno, Y. Noda, H. Koizumi, K. Nagasaka, K. Kurokawa, and H. Kobayashi, "The experimental results of an islanding detection method for Japanese AC modules," *Proceedings of 3rd World Conference on Photovoltaic Energy Conversion*, vol. 2, pp. 2058-2061, 12-16 May 2003.

[19] S. Jang and K. Kim, "Development of a logical rule-based islanding detection method for distributed resources," *IEEE Power Engineering Society Winter Meeting*, vol. 2, pp. 800-806, 27-31 Jan. 2002.

[20] J. Park, J. Kim, K. J. Yoo and B. H. Cho, "The power variation islanding detection method for the 3-phase grid-connected photovoltaic system," *PVSEC*, pp. 487-488, Jan. 2004.

[21] M. A. Redfern, J. I. Barret and O. Usta, "A new microprocessor based islanding protection algorithm for dispersed storage and generation units", *IEEE Trans. Power Delivery*, vol. 10, no. 3, pp. 1249-1254, Jul. 1995.

[22] M. A. Redfern, O. Usta, G. Fielding and E. P. Walker, "Power based algorithm to provide loss of grid protection for embedded generation," *IEE Proceedings-Generation, Transmission and Distribution*, vol. 141, no. 6, pp. 640-646, Nov. 1994.

[23] S. Huang and F. Pai, "A new approach to islanding detection of dispersed generators with self-commutated static power converters," *IEEE Trans. Power Delivery*, vol. 15, no. 2, pp. 500-507, Apr. 2000.

[24] H. Kobayashi and K. Takigawa, "Statistical evaluation of optimum islanding preventing method for utility interactive small scale dispersed PV systems," *First World Conference on Photovoltaic Energy Conversion*, vol. 1, pp. 1085-1088, 5-9 Dec. 1994.

[25] W. Freitas, Z. Huang and W. Xu, "A method for assessing the effectiveness of vector surge relays for distributed generator applications," *IEEE Trans. Power Delivery*, vol. 20, no. 1, pp. 57-63, Jan. 2005.

[26] O. Usta, "A power based digital algorithm for the protection of embedded generators," PhD thesis, University of Bath, 1992

[27] K. El-Arroudi, G. Joos, I. Kamwa and D. T. McGillis, "Intelligent-based approach to islanding detection in distributed generation," *IEEE Trans. Power Delivery*, vol. 22, no. 2, pp. 828-835, Apr. 2007.

[28] K. El-Arroudi and G. Joos, "Data mining approach to threshold settings of islanding relays in distributed generation," *IEEE Trans. Power Systems*, vol. 22, no. 3, pp. 1112-1119, Aug. 2007.

[29] H. Haeberlin, J. Graf and B. Fachhochschule, "Islanding of grid-connected PV inverters: test circuits and some test results," *2nd World Conference and Exhibition on Photovoltaic Solar Energy Conversion*, Vienna, Austria, pp. 2020-2023, 6-10 Jul. 1998.

[30] S. Yuyama, T. Ichinose, K. Kimoto, T. Itami, T. Ambo, C. Okado, K. Nakajima, S. Hojo, H. Shinohara, S. Ioka and M. Kuniyoshi, "A high-speed frequency shift method as a protection for islanding phenomena of utility interactive PV systems," *Solar Energy Materials and Solar Cells*, vol. 35, pp. 477-486, 1994.

[31] A. Tuladhar, "Anti-islanding device and method for grid connected inverters using random noise injection," U.S. Patent 6,853,940, Feb. 8, 2005.

[32] P. O'Kane and B. Fox, "Loss of mains detection for embedded generation by system impedance monitoring," *IEE Conf. Developments in Power System Protection*, Aberdeen, U.K., 1990.

[33] O. Johansen, N. Peguiront and P. Schnegg, "A new system of measurement of the network impedance," *Measurement Magazine*, Switzerland, vol. 9 no. 2, pp 50-55, Apr./Jun. 1991.

[34] G. A. Smith, P. A. Onions, and D. G. Infield, "Predicting islanding operation of grid connected PV inverters," *IEE Proceedings on Electric Power Applications*, vol. 147, no. 1, pp. 1-6, Jan. 2000.

[35] O. Tsukamoto, T. Okayasu, and K. Yamagishi, "Study on islanding of dispersed photovoltaic power systems connected to a utility power grid," *Solar Energy*, vol. 70, no. 6, pp. 505-511, 2001.

[36] A. Woyte, R. Belmans, K. Leuven and J. Nijs, "Islanding of grid-connected AC module inverters," *Proceedings of the 28th IEEE Photovoltaic Specialists Conference*, pp. 1683-1686, 17-22 Sept. 2000.

[37] A. Woyte, R. Belmans and J. Nijs, "Testing the islanding protection function of photovoltaic inverters," *IEEE Trans. Energy Conversion*, vol. 18, no. 1, pp. 157-162, Mar. 2003.

[38] E. Masaki, K. Hirokazu, T. Tsukasa and N. Hirofumi, "Inverter apparatus islanding operation detecting method and inverter apparatus capable of surely detecting an islanding operation with a simple construction," U.S. Patent 6 172 889, Jan. 9, 2001.

[39] M. E. Ropp, "Design issues for grid-connected photovoltaic systems," Ph.D. dissertation, Georgia Institute of Technology, Atlanta, GA, 1998.

[40] M. E. Ropp, M. Begovic, A. Rohatgi, "Analysis and performance assessment of the active frequency drift method of islanding prevention," *IEEE Trans. Energy Conversion*, vol. 14, no. 3, pp. 810-816, Sept. 1999.

[41] V. John, Z. Ye and A. Kolwalkar, "Investigation of anti-islanding protection of power converter based distributed generators using frequency domain analysis," *IEEE Trans. Power Electronics*, vol. 19, no. 5, pp. 1177-1183, Sept. 2004.

[42] M. E. Ropp, A. Rohatgi and M. Begovic, "Systems and methods for preventing islanding of grid-connected electrical power systems," U.S. Patent 6 429 546, Aug. 6, 2002.

[43] J. Stevens, et al, "Development and testing of an approach to anti-islanding in utility-interconnected photovoltaic systems," Sandia National Laboratories Report SAND200-1939, Aug. 2000.

[44] G. A. Kern, R. H. Bonn, J. Ginn and S. Gonzalez, "Results of Sandia national laboratories grid-tied inverter testing," *2nd World Conference and Exhibition on Photovoltaic Solar Energy Conversion*, Vienna, Austria, 6-10 Jul. 1998.

[45] Z. Ye, R. Walling, L. Garces, R. Zhou, L. Li and T. Wang, "Study and development of anti-islanding control for grid-connected inverters," NREL/SR-560-36243, Golden, CO: National Renewable Energy Laboratory, May 2004.

[46] G. A. Kern, "Sunsine300, utility interactive AC module anti-islanding test results," *Proceedings of the Twenty Sixth IEEE Photovoltaic Specialist Conference*, Anaheim, California, Sept./Oct., 1997.

[47] K. Kaln, A. Grabitz, P. Kremer, and B. Kress, "Five years of ENS (MSD) islanding protection-What could be the next steps?" *Proc. 17th European Photovoltaic Solar Energy Conf. Exhibition*, Munich, Germany, p. 2544, 2001.

[48] G. Hung, C. Chang and C. Chen, "Automatic phase-shift method for islanding detection of grid-connected photovoltaic inverters," *IEEE Trans. Energy Conversion*, vol. 18, no. 1, pp. 169-173, Mar. 2003.

[49] O. Tsukamoto and K. Yamagishi, "Detection of islanding of multiple dispersed photovoltaic power systems," *Solar Energy*, 58(1), pp. 9-15, 1996.

[50] R. M. Hudson, T. Thorne, F. Mekanik, M. R. Behnke, S. Gonzalez and J. Ginn, "Implementation and testing of anti-islanding algorithms for IEEE 929-2000 compliance of single phase photovoltaic inverters," *The Twenty-Ninth IEEE Photovoltaic Specialists Conference*, pp. 1414-1419, May 2002.

[51] C. Jeraputra and P. N. Enjeti, "Development of a robust anti-islanding algorithm for utility interconnection of distributed fuel cell powered generation," *IEEE Trans. Power Electronics*, vol. 19, no. 5, pp. 1163-1170, Sept. 2004.

[52] C. Jeraputra, P. N. Enjeti, and I. H. Hwang, "Development of a robust anti-islanding algorithm for utility interconnection of distributed fuel cell powered generation," *Proc. APEC'04 Conf.*, vol. 3, pp. 1534-1540, 2004.

[53] I. H. Hwang, "A novel anti-islanding method for utility interconnection of distributed power generation systems," *KIEE International Trans. EMECS*, vol. 4-B, no. 4, pp. 217-224, 2004.

[54] Ballard Power Systems Inc., "Ecostar power converter anti-islanding capability," [Online], Available: http://www.ballard.com/

[55] J. W. Warin, "Loss of mains protection," *Proc. ERA Conf. Circuit Protection Industrial Commercial Inst.*, London, U.K., 1990.

[56] C. B. Cooper, "Standby generation - Problems and prospective gains from parallel running," *Proc. Power System Protection*, Singapore, 1989.

[57] A. Kitamura, M. Okamoto, F. Yamamoto, K. Nakaji, H. Matsuda and K. Hotta, "Islanding phenomenon elimination study at Rokko test center," *Proceedings of the 1st World Conference on Photovoltaic Energy Conversion*, pt. 1, pp. 759-762, 1994.

[58] A. Kitamura, M. Okamoto, K. Hotta, K. Takigawa, H. Kobayashi and Y. Ariga, "Islanding prevention measures: demonstration testing at Rokko test center for advanced energy systems," *Proceedings of the 23rd IEEE Photovoltaic Specialists Conference*, pp. 1063-1067, 1993.

[59] P. Toggweiler, "Summary and conclusions," Proceedings of the IEA-PVPS Task V Workshop "Grid Connected Photovoltaic Systems," pp. 15-17, 15-16 Sept. 1997.

[60] M. E. Ropp, K. Aaker, J. Haigh and N. Sabbah, "Using power line carrier communications to prevent islanding," *Proceedings of the 28th IEEE Photovoltaic Specialists Conference*, pp. 1675-1678, 17-22 Sept. 2000.

[61] W. Xu, G. Zhang, C. Li, W. Wang, G. Wang and J. Kliber, "A power line signaling based technique for anti-islanding protection of distributed generators - Part I: scheme and analysiss," *IEEE Trans. Power Delivery*, vol. 22, no. 3, pp. 1758-1772, Jul. 2007.

[62] *IEEE guide for interfacing dispersed storage and generation facilities with electric utility systems*, ANSI/IEEE STANDARD 1001-1988, New York, 1989.

[63] IEEE SPECIAL REPORT: "Inter-tie protection of consumer-owned source of generation, 3 VA or less," IEEE Publication 88TH0224-6-PWR, 1989

[64] L. J. Powell, "An industrial view of utility cogeneration protection requirements," *IEEE Trans. Industry Applications*, vol. 24, no. 1, pp. 75-85, Jan. 1988.

[65] C. J. Mozina, "Interconnection protection of IPP generators at commercial/ industrial facilities," *IEEE Trans. Industry Applications*, vol. 37, no. 3, pp. 681-689, May 2001.

[66] M. A. Referrn, O. Usta, and G. Fielding, "Protection against lost of utility grid supply for a dispersed storage and generation unit", *IEEE Trans. Power Delivery*, vol. 8, no. 3, pp. 948-954, Jul. 1993.

[67] R. M. Rifaat, "Critical considerations for utility/cogeneration inter-tie protection scheme configuration," *IEEE Trans. Industry Applications*, vol. 31, no. 5, pp. 973-977, Sept. 1995.

[68] Y. Tomita, C. Fukui, H. Kudo, J. Koda and K. Yabe, "A cooperative protection system with an agent model," *IEEE Trans. Power Delivery*, vol. 13, no. 4, pp. 1060-1064, Oct. 1998.

[69] M. E. Ropp, M. Begovic, A. Rohatgi, G. A. Kern, R. H. Bonn and S. Gonzalez, "Determining the relative effectiveness of islanding detection methods using phase criteria and nondetection zones," *IEEE Trans. Energy Conversion*, vol. 15, no. 3, pp. 290-296, Sept. 2000.

[70] L. A. C. Lopes and H. Sun, "Performance assessment of active frequency drifting islanding detection methods," *IEEE Trans. Energy Conversion*, vol. 21, no. 1, pp. 171-180, Mar. 2006.

[71] B. Kroposki, R. DeBlasio, and J. Galdo, "Distributed power program DER pilot test at the Nevada test site," NREL, Golden, CO, NREL/TP-560-32063, May 2002.

[72] R. A. Walling and N. W. Miller, "Distributed generation islanding-implications on power system dynamic performance," *IEEE Power Engineering Society Summer Meeting*, vol. 1, pp. 92-96, 21-25 July 2002.

[73] N. W. Miller and Z. Ye, "Report on distributed generation penetration study," National Renewable Energy Lab, Contract no: DE-AC36-99-GO10337, 2003.

[74] J. Liao and S. Yeh, "A novel instantaneous power control strategy and analytic model for integrated rectifier/inverter systems," *IEEE Trans. Power Electronics*, vol. 15, no. 6, pp. 996-1006, November 2000.

[75] A. M. Gole, V. K. Sood and L. Mootosamy, "Validation and analysis of a grid control system using d-q-z transformation for static compensator systems," in *Proc. Canadian Conf. Elect. Comput. Eng.*, Montreal, QC, Canada, September 1989, pp. 745-748.

[76] P. Kundur, "Power system stability and control," Electric Power Research Institute, California, 1994.

[77] E. P. Dick and A. Narang, "Canadian urban benchmark distribution systems," CANMET Energy Technology Centre - Varennes, Nature Resources Canada, Tech. Rep., 36 pages, March 2005. http://cetc-varennes.nrcan.gc.ca/fichier.php/codectec/En/2005-121/2005-121e.pdf

[78] F. Katiraei, M. R., Iravani, "Power management strategies for a microgrid with multiple distributed generation units," *IEEE Trans. Power Systems*, vol. 21, no. 4, pp. 1821-1831, Nov. 2006.

[79] P. Sanchis, L. Marroyo and J. Coloma, "Design methodology for the frequency shift method of islanding prevention and analysis of its detection capability," *Progress in Photovoltaics: Research and Applications*, vol. 13, pp. 409-428, 2005.

[80] Z. Ye, A. Kolwalkar, Y. Zhang, P. Du and R. Walling, "Evaluation of anti-islanding schemes based on nondetection zone concept," *IEEE Trans. Power Electronics*, vol. 19, no. 5, pp. 1171-1176, Sept. 2004.

[81] H. H. Zeineldin, E. F. El-Saadany and M. M. A. Salama, "Impact of DG interface control on islanding detection and nondetection zones," *IEEE Trans. Power Delivery*, vol. 21, no. 3, pp. 1515-1523, Jul. 2006.

[82] S. N. Liew and G. Strbac, "Maximising penetration of wind generation in existing distribution networks," *Proc. Inst. Elect. Eng.-Gener. Transm. Distrib.*, vol. 149, no. 3, pp. 256-262, May 2002.

[83] A. Bhowmik, A. Maitra, S. M. Halpin and J. E. Schatz, "Determination of allowable penetration levels of distributed generation resources based on harmonic limit considerations," *IEEE Trans. Power Delivery*, vol. 18, no. 2, pp. 619-624, Apr. 2003.

[84] S. K. Salman and I. M. Rida, "Investigating the impact of embedded generation on relay settings of utilities' electrical feeders," *IEEE Trans. Power Delivery*, vol. 16, no. 2, pp. 246-251, Apr. 2001.

[85] "DG power quality, protection and reliability case studies report program: Reliable, low cost distributed generator/utility system interconnect," National Renewable Energy Lab., Contract NAD-1-30 605-01, 2001.

[86] S. J. Ranade, R. P. Nadipuram, S. Omick and L. F. Kazda, "A study of islanding in utility-connected residential photovoltaic systems - Part I: models and analytical methods," *IEEE Trans. Energy Conversion*, vol. 4, no. 3, pp. 436-445, Sept. 1989.

[87] S. J. Ranade, R. P. Nadipuram, S. Omick and L. F. Kazda, "A study of islanding in utility-connected residential photovoltaic systems - Part II: case studies," *IEEE Trans. Energy Conversion*, vol. 4, no. 3, pp. 446-452, Sept. 1989.

[88] S. L. Varricchio, N. Martins and L. T. G. Lima, "A newton-raphson method based on eigenvalue sensitivities to improve harmonic voltage performance," *IEEE Trans. Power Delivery*, vol. 18, no. 1, pp. 334-342, Jan. 2003.

Appendix A

Modeling of Single-Phase Inverter

Single-phase VSI is more applied in small size DGs. Figure A.1 displays the switching function model a single-phase grid-connected VSI. The inverter output current i_a is compared with a reference current i_{aref} to generate the error signal required by the PWM generator. The reference current is controlled by the variables i_d, i_q and θ. The angle θ is the single-phase voltage angle measured by a single-phase PLL. The currents i_d, i_q can be the presetting values of the inverter or from the power controller shown in Figure A.2. They determine the inverter output current amplitude I and the inverter power factor angle ϕ. The inverter will be the unity power factor inverter if the angle ϕ is zero. With the power controller the inverter active and reactive power are decoupled and controlled separately. The power equations are as follows:

$$i_d = (k_{pp} + \frac{k_{ip}}{s})(P_{ref} - P) \tag{A.1}$$

$$i_q = (k_{pp} + \frac{k_{ip}}{s})(Q_{ref} - Q) \tag{A.2}$$

where the variables P and Q can also be calculated by Equations (3.14) and (3.15). The voltages v_d and v_q needed in the calculation are obtained by the following $\alpha\beta$ - dq transformation:

$$\begin{bmatrix} v_d \\ v_q \end{bmatrix} = \begin{bmatrix} \cos\theta & \sin\theta \\ -\sin\theta & \cos\theta \end{bmatrix} \begin{bmatrix} v_\alpha \\ v_\beta \end{bmatrix} \tag{A.3}$$

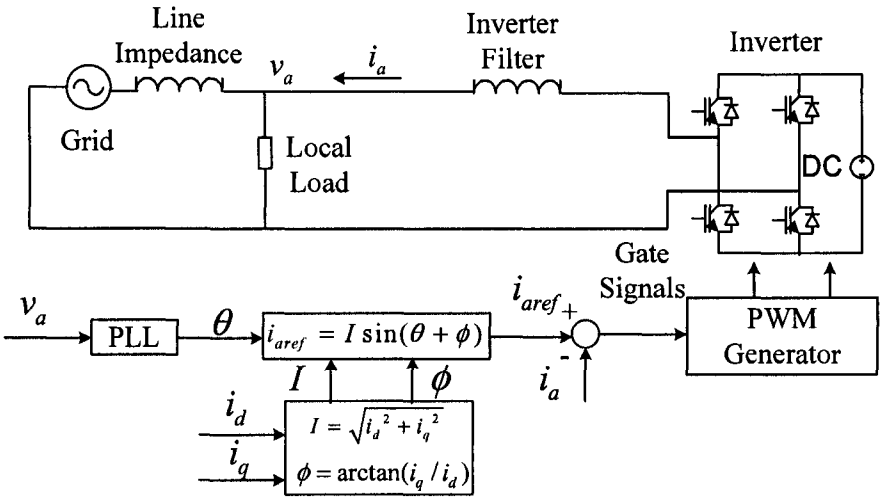

Figure A.1: Single-phase grid-connected VSI

where the inverter terminal voltage v_a is v_α and the virtual voltage orthogonal to v_a is v_β.

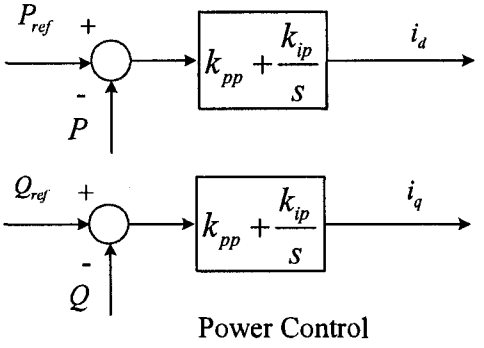

Figure A.2: Single-phase VSI power controller

The single-phase VSI is replaced by a controlled current source in its average model which is seen in Figure A.3. The PWM generator and inverter filter are neglected in this analytical model. By using the dq-$\alpha\beta$ transformation defined in Equation (A.4) the inverter output current is synchronized to the inverter output voltage.

$$\begin{bmatrix} i_\alpha \\ i_\beta \end{bmatrix} = \begin{bmatrix} \cos\theta & -\sin\theta \\ \sin\theta & \cos\theta \end{bmatrix} \begin{bmatrix} i_d \\ i_q \end{bmatrix} \tag{A.4}$$

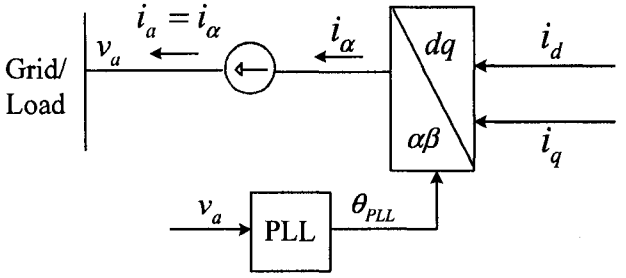

Figure A.3: Single-phase average VSI model

The structure of the single-phase PLL is different with that of the three-phase PLL in some degree as the input voltage of the single-phase PLL is only one phase. The single-phase PLL model is shown in Figure A.4 where the virtual phase voltage v_β is acquired through the dq-$\alpha\beta$ transformation in the implementation. In the analytical model, the voltage v_β can be regarded as the ideal orthogonal of v_a. For example, if the voltage v_a is $V \sin \omega t$ then the voltage $V \cos \omega t$ is used as v_β directly. Consequently, the equations of the single-phase PLL are the same with the three-phase PLL.

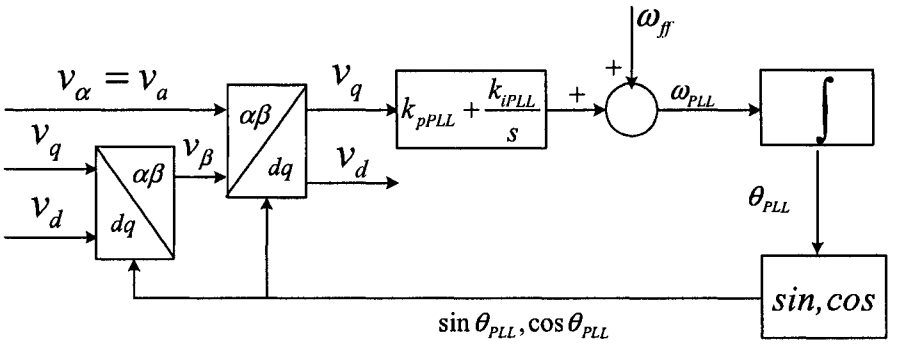

Figure A.4: Single-phase PLL model

Appendix B

Small-Signal Model of Single DG System with Parallel *RLC* Load

The small-signal model of the single DG system with parallel RLC load is described as follows:

$$\begin{aligned}\Delta v_d &= Lp\Delta i_{Nd} + R\Delta i_{Nd} - \omega_0 L\Delta i_{Nq} - Li_{Nq0}\Delta\omega_{PLL} - E\sin\delta_0\Delta\delta_{PLL}\\ \Delta v_q &= Lp\Delta i_{Nq} + R\Delta i_{Nq} + \omega_0 L\Delta i_{Nd} + Li_{Nd0}\Delta\omega_{PLL} - E\cos\delta_0\Delta\delta_{PLL}\end{aligned} \tag{B.1}$$

$$\begin{aligned}\Delta u_d &= L_s p\Delta i_d\\ \Delta u_q &= L_s p\Delta i_q\end{aligned} \tag{B.2}$$

$$\begin{aligned}\Delta i_{Nd} &= \Delta i_d - \Delta i_{Rd} - \Delta i_{Ld} - \Delta i_{Cd}\\ \Delta i_{Nq} &= \Delta i_q - \Delta i_{Rq} - \Delta i_{Lq} - \Delta i_{Cq}\end{aligned} \tag{B.3}$$

$$\begin{aligned}\Delta i_{Rd} &= \frac{\Delta v_d}{R_L}\\ \Delta i_{Rq} &= \frac{\Delta v_q}{R_L}\end{aligned} \tag{B.4}$$

$$\begin{aligned}\Delta v_d &= L_L p\Delta i_{Ld} - \omega_0 L_L\Delta i_{Lq} - L_L i_{Lq0}\Delta\omega_{PLL}\\ \Delta v_q &= L_L p\Delta i_{Lq} + \omega_0 L_L\Delta i_{Ld} + L_L i_{Ld0}\Delta\omega_{PLL}\end{aligned} \tag{B.5}$$

$$\begin{aligned}\Delta i_{Cd} &= C_L p\Delta v_d - \omega_0 C_L\Delta v_q - C_L v_{q0}\Delta\omega_{PLL}\\ \Delta i_{Cq} &= C_L p\Delta v_q + \omega_0 C_L\Delta v_d + C_L v_{d0}\Delta\omega_{PLL}\end{aligned} \tag{B.6}$$

$$\begin{aligned} p\Delta u_d &= k_{pi}p(\Delta i^*_{dref} - \Delta i_d) + k_{ii}(\Delta i^*_{dref} - \Delta i_d) \\ p\Delta u_q &= k_{pi}p(\Delta i^*_{qref} - \Delta i_q) + k_{ii}(\Delta i^*_{qref} - \Delta i_q) \end{aligned} \tag{B.7}$$

$$\begin{aligned} p\Delta i_{dref} &= -k_{pp}p\Delta P - k_{ip}\Delta P + k_{ip}\Delta P_{ref} \\ p\Delta i_{qref} &= -k_{pp}p\Delta Q - k_{ip}\Delta Q + k_{ip}\Delta Q_{ref} \end{aligned} \tag{B.8}$$

$$p\Delta\delta_{PLL} = \Delta\omega_{PLL} \tag{B.9}$$

$$p\Delta\omega_{PLL} = k_{pPLL}p\Delta v_q + k_{iPLL}\Delta v_q \tag{B.10}$$

$$\begin{aligned} \Delta P &= v_{d0}\Delta i_d + i_{d0}\Delta v_d + v_{q0}\Delta i_q + i_{q0}\Delta v_q \\ \Delta Q &= v_{d0}\Delta i_q + i_{q0}\Delta v_d - v_{q0}\Delta i_d - i_{d0}\Delta v_q \end{aligned} \tag{B.11}$$

$$\Delta\theta_f + T_w p\Delta\theta_f = \frac{\pi}{2}K_f T_w p\Delta\omega_{PLL} \tag{B.12}$$

$$\begin{aligned} \Delta i^*_{dref} &= \cos\theta_{f0}\Delta i_{dref} - \sin\theta_{f0}\Delta i_{qref} - i_{q0}\Delta\theta_f \\ \Delta i^*_{qref} &= \sin\theta_{f0}\Delta i_{dref} + \cos\theta_{f0}\Delta i_{qref} + i_{d0}\Delta\theta_f \end{aligned} \tag{B.13}$$

where the variables with the subscript $_0$ are the steady-state values. This model is suitable for constant power-controlled inverter. The input variations of the inverter areΔP_{ref} and ΔQ_{ref}. If a constant current-controlled inverter is used in the DG system, Equation (B.8) and (B.11) will be removed and the input variations of the inverter will be Δi_{dref} and Δi_{qref}.

As the above small-signal model is composed of a set of differential-algebraic equations (DAEs) and it is not easy to analyze the model directly, the thesis utilizes the descriptor system technique [88] to get the system characteristics. The following descriptor system equation is obtained for the complete system:

$$\mathbf{E}p\Delta\mathbf{x} = \mathbf{A}\Delta\mathbf{x} + \mathbf{B}\Delta\mathbf{u} \tag{B.14}$$

where

$$\Delta\mathbf{x} = [\Delta v_d \Delta v_q \Delta i_d \Delta i_q \Delta i_{Nd} \Delta i_{Nq} \Delta i_{Rd} \Delta i_{Rq} \Delta i_{Ld} \Delta i_{Lq} \Delta i_{Cd} \Delta i_{Cq} \\ \Delta u_d \Delta u_q \Delta i_{dref} \Delta i_{qref} \Delta\delta_{PLL} \Delta\omega_{PLL} \Delta P \Delta Q \Delta\theta_f \Delta i^*_{dref} \Delta i^*_{qref}]^T \tag{B.15}$$

$$\Delta\mathbf{u} = [\Delta P_{ref} \Delta Q_{ref}]^T \tag{B.16}$$

The superscript ^{T} denotes the vector transpose. The matrix $\mathbf{E}$ $(_{23\times23})$ is singular and the state matrix $\mathbf{A}$ $(_{23\times23})$ is regular. The input matrix $\mathbf{B}$ $(_{23\times2})$ is decided by Equation (B.8). There are redundant states in Equation (B.15), which results in some infinite eigenvalues of Equation (B.14). The eigenvalues of Equation (B.14) provide the basis for the small-signal stability analysis of the DG system. The matrices in Equation (B.14) are as follows:

$$\mathbf{E} = \begin{bmatrix} \mathbf{E}_1 & \mathbf{E}_2 & \mathbf{E}_3 \\ \mathbf{E}_4 & \mathbf{E}_5 & \mathbf{E}_6 \\ \mathbf{E}_7 & \mathbf{E}_8 & \mathbf{E}_9 \end{bmatrix} \tag{B.17}$$

$$\mathbf{E}_1 = \begin{bmatrix} 0 & 0 & 0 & 0 & -L & 0 & 0 & 0 \\ 0 & 0 & 0 & 0 & 0 & -L & 0 & 0 \\ 0 & 0 & L_s & 0 & 0 & 0 & 0 & 0 \\ 0 & 0 & 0 & L_s & 0 & 0 & 0 & 0 \\ 0 & 0 & 0 & 0 & 0 & 0 & 0 & 0 \\ 0 & 0 & 0 & 0 & 0 & 0 & 0 & 0 \\ 0 & 0 & 0 & 0 & 0 & 0 & 0 & 0 \\ 0 & 0 & 0 & 0 & 0 & 0 & 0 & 0 \end{bmatrix} \tag{B.18}$$

$$\mathbf{E}_4 = \begin{bmatrix} 0 & 0 & 0 & 0 & 0 & 0 & 0 \\ 0 & 0 & 0 & 0 & 0 & 0 & 0 \\ -C_L & 0 & 0 & 0 & 0 & 0 & 0 \\ 0 & -C_L & 0 & 0 & 0 & 0 & 0 \\ 0 & 0 & k_{pi} & 0 & 0 & 0 & 0 \\ 0 & 0 & 0 & k_{pi} & 0 & 0 & 0 \\ 0 & 0 & 0 & 0 & 0 & 0 & 0 \\ 0 & 0 & 0 & 0 & 0 & 0 & 0 \end{bmatrix} \tag{B.19}$$

$$\mathbf{E}_5 = \begin{bmatrix} -L_L & 0 & 0 & 0 & 0 & 0 & 0 & 0 \\ 0 & -L_L & 0 & 0 & 0 & 0 & 0 & 0 \\ 0 & 0 & 0 & 0 & 0 & 0 & 0 & 0 \\ 0 & 0 & 0 & 0 & 0 & 0 & 0 & 0 \\ 0 & 0 & 0 & 0 & 1 & 0 & 0 & 0 \\ 0 & 0 & 0 & 0 & 0 & 1 & 0 & 0 \\ 0 & 0 & 0 & 0 & 0 & 0 & 1 & 0 \\ 0 & 0 & 0 & 0 & 0 & 0 & 0 & 1 \end{bmatrix} \tag{B.20}$$

$$\mathbf{E}_6 = \begin{bmatrix} 0 & 0 & 0 & 0 & 0 & 0 & 0 \\ 0 & 0 & 0 & 0 & 0 & 0 & 0 \\ 0 & 0 & 0 & 0 & 0 & 0 & 0 \\ 0 & 0 & 0 & 0 & 0 & 0 & 0 \\ 0 & 0 & 0 & 0 & 0 & -k_{pi} & 0 \\ 0 & 0 & 0 & 0 & 0 & 0 & -k_{pi} \\ 0 & 0 & k_{pp} & 0 & 0 & 0 & 0 \\ 0 & 0 & 0 & k_{pp} & 0 & 0 & 0 \end{bmatrix} \tag{B.21}$$

$$\mathbf{E}_7 = \begin{bmatrix} 0 & 0 & 0 & 0 & 0 & 0 & 0 & 0 \\ 0 & -k_{p_{PLL}} & 0 & 0 & 0 & 0 & 0 & 0 \\ 0 & 0 & 0 & 0 & 0 & 0 & 0 & 0 \\ 0 & 0 & 0 & 0 & 0 & 0 & 0 & 0 \\ 0 & 0 & 0 & 0 & 0 & 0 & 0 & 0 \\ 0 & 0 & 0 & 0 & 0 & 0 & 0 & 0 \\ 0 & 0 & 0 & 0 & 0 & 0 & 0 & 0 \end{bmatrix} \tag{B.22}$$

$$\mathbf{E}_9 = \begin{bmatrix} 1 & 0 & 0 & 0 & 0 & 0 & 0 \\ 0 & 1 & 0 & 0 & 0 & 0 & 0 \\ 0 & 0 & 0 & 0 & 0 & 0 & 0 \\ 0 & 0 & 0 & 0 & 0 & 0 & 0 \\ 0 & \frac{\pi}{2}K_f T_w & 0 & 0 & -T_w & 0 & 0 \\ 0 & 0 & 0 & 0 & 0 & 0 & 0 \\ 0 & 0 & 0 & 0 & 0 & 0 & 0 \end{bmatrix} \tag{B.23}$$

$$\mathbf{E}_2 = [\mathbf{0}]_{8\times 8}, \mathbf{E}_3 = [\mathbf{0}]_{8\times 7}, \mathbf{E}_8 = [\mathbf{0}]_{7\times 8} \tag{B.24}$$

$$\mathbf{A} = \begin{bmatrix} \mathbf{A}_1 & \mathbf{A}_2 & \mathbf{A}_3 \\ \mathbf{A}_4 & \mathbf{A}_5 & \mathbf{A}_6 \\ \mathbf{A}_7 & \mathbf{A}_8 & \mathbf{A}_9 \end{bmatrix} \tag{B.25}$$

$$\mathbf{A}_1 = \begin{bmatrix} -1 & 0 & 0 & 0 & R & -X & 0 & 0 \\ 0 & -1 & 0 & 0 & X & -R & 0 & 0 \\ 0 & 0 & 0 & 0 & 0 & 0 & 0 & 0 \\ 0 & 0 & 0 & 0 & 0 & 0 & 0 & 0 \\ 0 & 0 & 1 & 0 & -1 & 0 & -1 & 0 \\ 0 & 0 & 0 & 1 & 0 & -1 & 0 & -1 \\ 1/R_L & 0 & 0 & 0 & 0 & 0 & -1 & 0 \\ 0 & 1/R_L & 0 & 0 & 0 & 0 & 0 & -1 \end{bmatrix} \tag{B.26}$$

$$\mathbf{A}_2 = \begin{bmatrix} 0 & 0 & 0 & 0 & 0 & 0 & 0 \\ 0 & 0 & 0 & 0 & 0 & 0 & 0 \\ 0 & 0 & 0 & 1 & 0 & 0 & 0 \\ 0 & 0 & 0 & 0 & 1 & 0 & 0 \\ -1 & 0 & -1 & 0 & 0 & 0 & 0 \\ 0 & -1 & 0 & -1 & 0 & 0 & 0 \\ 0 & 0 & 0 & 0 & 0 & 0 & 0 \\ 0 & 0 & 0 & 0 & 0 & 0 & 0 \end{bmatrix} \tag{B.27}$$

$$\mathbf{A}_3 = \begin{bmatrix} -E\sin\delta_0 & -Li_{Nq0} & 0 & 0 & 0 & 0 & 0 \\ -E\cos\delta_0 & Li_{Nd0} & 0 & 0 & 0 & 0 & 0 \\ 0 & 0 & 0 & 0 & 0 & 0 & 0 \\ 0 & 0 & 0 & 0 & 0 & 0 & 0 \\ 0 & 0 & 0 & 0 & 0 & 0 & 0 \\ 0 & 0 & 0 & 0 & 0 & 0 & 0 \\ 0 & 0 & 0 & 0 & 0 & 0 & 0 \\ 0 & 0 & 0 & 0 & 0 & 0 & 0 \end{bmatrix} \tag{B.28}$$

$$\mathbf{A}_4 = \begin{bmatrix} -1 & 0 & 0 & 0 & 0 & 0 & 0 \\ 0 & -1 & 0 & 0 & 0 & 0 & 0 \\ 0 & -\omega_0 C_L & 0 & 0 & 0 & 0 & 0 \\ \omega_0 C_L & 0 & 0 & 0 & 0 & 0 & 0 \\ 0 & 0 & -k_{ii} & 0 & 0 & 0 & 0 \\ 0 & 0 & 0 & -k_{ii} & 0 & 0 & 0 \\ 0 & 0 & 0 & 0 & 0 & 0 & 0 \\ 0 & 0 & 0 & 0 & 0 & 0 & 0 \end{bmatrix} \tag{B.29}$$

$$\mathbf{A}_5 = \begin{bmatrix} 0 & -\omega_0 L_L & 0 & 0 & 0 & 0 & 0 & 0 \\ \omega_0 L_L & 0 & 0 & 0 & 0 & 0 & 0 & 0 \\ 0 & 0 & -1 & 0 & 0 & 0 & 0 & 0 \\ 0 & 0 & 0 & -1 & 0 & 0 & 0 & 0 \\ 0 & 0 & 0 & 0 & 1 & 0 & 0 & 0 \\ 0 & 0 & 0 & 0 & 0 & 1 & 0 & 0 \\ 0 & 0 & 0 & 0 & 0 & 0 & 0 & 0 \\ 0 & 0 & 0 & 0 & 0 & 0 & 0 & 0 \end{bmatrix} \tag{B.30}$$

$$\mathbf{A}_6 = \begin{bmatrix} 0 & -L_L i_{Lq0} & 0 & 0 & 0 & 0 & 0 \\ 0 & L_L i_{Ld0} & 0 & 0 & 0 & 0 & 0 \\ 0 & -C_L v_{q0} & 0 & 0 & 0 & 0 & 0 \\ 0 & C_L v_{d0} & 0 & 0 & 0 & 0 & 0 \\ 0 & 0 & 0 & 0 & 0 & k_{ii} & 0 \\ 0 & 0 & 0 & 0 & 0 & 0 & k_{ii} \\ 0 & 0 & -k_{ip} & 0 & 0 & 0 & 0 \\ 0 & 0 & 0 & -k_{ip} & 0 & 0 & 0 \end{bmatrix} \tag{B.31}$$

$$\mathbf{A}_7 = \begin{bmatrix} 0 & 0 & 0 & 0 & 0 & 0 & 0 & 0 \\ 0 & k_{iPLL} & 0 & 0 & 0 & 0 & 0 & 0 \\ i_{d0} & i_{q0} & v_{d0} & v_{q0} & 0 & 0 & 0 & 0 \\ i_{q0} & -i_{d0} & -v_{q0} & v_{d0} & 0 & 0 & 0 & 0 \\ 0 & 0 & 0 & 0 & 0 & 0 & 0 & 0 \\ 0 & 0 & 0 & 0 & 0 & 0 & 0 & 0 \\ 0 & 0 & 0 & 0 & 0 & 0 & 0 & 0 \end{bmatrix} \tag{B.32}$$

$$\mathbf{A}_8 = \begin{bmatrix} 0 & 0 & 0 & 0 & 0 & 0 & 0 & 0 \\ 0 & 0 & 0 & 0 & 0 & 0 & 0 & 0 \\ 0 & 0 & 0 & 0 & 0 & 0 & 0 & 0 \\ 0 & 0 & 0 & 0 & 0 & 0 & 0 & 0 \\ 0 & 0 & 0 & 0 & 0 & 0 & 0 & 0 \\ 0 & 0 & 0 & 0 & 0 & 0 & \cos\theta_{f0} & -\sin\theta_{f0} \\ 0 & 0 & 0 & 0 & 0 & 0 & \sin\theta_{f0} & \cos\theta_{f0} \end{bmatrix} \tag{B.33}$$

$$\mathbf{A}_9 = \begin{bmatrix} 0 & 1 & 0 & 0 & 0 & 0 & 0 \\ 0 & 0 & 0 & 0 & 0 & 0 & 0 \\ 0 & 0 & -1 & 0 & 0 & 0 & 0 \\ 0 & 0 & 0 & -1 & 0 & 0 & 0 \\ 0 & 0 & 0 & 0 & 1 & 0 & 0 \\ 0 & 0 & 0 & 0 & -i_{q0} & -1 & 0 \\ 0 & 0 & 0 & 0 & i_{d0} & 0 & -1 \end{bmatrix} \tag{B.34}$$

B is the 23 × 2 matrix and all of its elements are zero except for:

$$\begin{aligned} B_{(15,1)} &= k_{ip} \\ B_{(16,2)} &= k_{ip} \end{aligned} \tag{B.35}$$

The steady-state values of the state variables in the model as calculated as follows:

$$\theta_{f0} = \frac{\pi}{2} cf_0 \tag{B.36}$$

$$v_{d0} = V_0, v_{q0} = 0 \tag{B.37}$$

$$i_{d0} = \frac{P_{ref}}{V_0}, i_{q0} = \frac{Q_{ref}}{V_0} \tag{B.38}$$

$$i_{Rd0} = \frac{v_{d0}}{R_L}, i_{Rq0} = \frac{v_{q0}}{R_L} \tag{B.39}$$

$$i_{Ld0} = \frac{v_{q0}}{\omega_0 L_L}, i_{Lq0} = \frac{v_{d0}}{\omega_0 L_L} \tag{B.40}$$

$$i_{Cd0} = -v_{q0}\omega_0 C_L, i_{Cq0} = v_{d0}\omega_0 C_L \tag{B.41}$$

$$\begin{aligned} i_{Nd0} &= i_{d0} - i_{Rd0} - i_{Ld0} - i_{Cd0} \\ i_{Nq0} &= i_{q0} - i_{Rq0} - i_{Lq0} - i_{Cq0} \end{aligned} \tag{B.42}$$

The necessary values V_0 and δ_0 needed in the calculations are obtained from the power flow of the equivalent circuit shown in Figure B.1 where $X = \omega_0 L$, $X_L = \omega_0 L_L$ and $X_C = 1/\omega_0 C_L$.

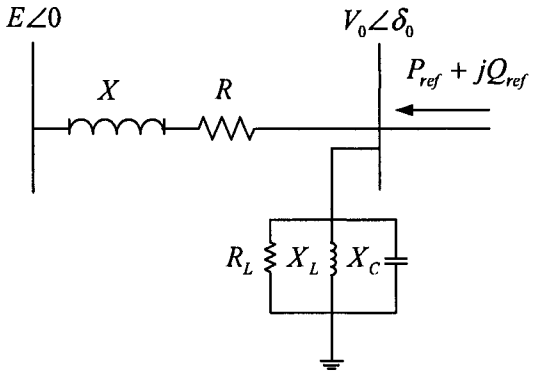

Figure B.1: Equivalent steady-state circuit of the single DG system with RLC load

The power flow equation is shown in Equation B.43.

$$P_{ref} + jQ_{ref} = V_0\angle\delta_0\left(\frac{V_0\angle\delta_0 - E\angle 0}{R + jX} + \frac{V_0\angle\delta_0}{Z_L}\right)^{\star} \tag{B.43}$$

where the superscript * designates conjugate in phasor expression and

$$Z_L = \frac{R_L X_L X_C}{X_L X_C + jX_L R_L - jX_C R_L} \tag{B.44}$$

It is important to point out that for constant power-controlled inverter, although the SFS control is inserted into the inverter controller the output power of the inverter will still be the reference power ($P_{ref} + jQ_{ref}$) during the steady state. This is because the outer power loop control counteracts the current phase shift effect of the SFS control. However, for constant current-controlled inverter, the SFS control will begin to affect the inverter steady-state output current. If the inverter output current reference is set as $i_{dref} + ji_{qref}$ then the real output current will be:

$$\begin{bmatrix} i_{d0} \\ i_{q0} \end{bmatrix} = \begin{bmatrix} \cos\theta_{f0} & -\sin\theta_{f0} \\ \sin\theta_{f0} & \cos\theta_{f0} \end{bmatrix} \begin{bmatrix} i_{dref} \\ i_{qref} \end{bmatrix} \tag{B.45}$$

Correspondingly, the system steady-state equation will change to:

$$i_{d0} + ji_{q0} = \frac{V_0\angle\delta_0 - E\angle 0}{R + jX} + \frac{V_0\angle\delta_0}{Z_L} \tag{B.46}$$

Appendix C

Small-Signal Model of Single DG System with Motor Load

The small-signal model of the single DG system model with motor load is as follows (the inverter part is not included):

$$\begin{aligned} \Delta v_x &= \frac{p\Delta\psi_{sx}}{\omega_0} - \Delta\psi_{sy} + R_s\Delta i_{sx} \\ \Delta v_y &= \frac{p\Delta\psi_{sy}}{\omega_0} + \Delta\psi_{sx} + R_s\Delta i_{sy} \end{aligned} \tag{C.1}$$

$$\begin{aligned} 0 &= \frac{p\Delta\psi_{rx}}{\omega_0} - \frac{\omega_0 - \omega_{r0}}{\omega_0}\Delta\psi_{ry} + \frac{\psi_{ry0}}{\omega_0}\Delta\omega_r + R_r\Delta i_{rx} \\ 0 &= \frac{p\Delta\psi_{ry}}{\omega_0} + \frac{\omega_0 - \omega_{r0}}{\omega_0}\Delta\psi_{rx} - \frac{\psi_{rx0}}{\omega_0}\Delta\omega_r + R_r\Delta i_{ry} \end{aligned} \tag{C.2}$$

$$\begin{aligned} \Delta\psi_{sx} &= (X_m + X_s)\Delta i_{sx} + X_m\Delta i_{rx} \\ \Delta\psi_{sy} &= (X_m + X_s)\Delta i_{sy} + X_m\Delta i_{ry} \end{aligned} \tag{C.3}$$

$$\begin{aligned} \Delta\psi_{rx} &= (X_m + X_r)\Delta i_{rx} + X_m\Delta i_{sx} \\ \Delta\psi_{ry} &= (X_m + X_r)\Delta i_{ry} + X_m\Delta i_{sy} \end{aligned} \tag{C.4}$$

$$\Delta T_e = \psi_{sx0}\Delta i_{sy} + i_{sy0}\Delta\psi_{sx} - i_{sx0}\Delta\psi_{sy} - \psi_{sy0}\Delta i_{sx} \tag{C.5}$$

$$\frac{p\Delta\omega_r}{\omega_0} = \frac{1}{2H}(\Delta T_e - \Delta T_m) \tag{C.6}$$

$$\begin{aligned}\Delta v_d &= \cos\delta_0\Delta v_x - v_{x0}\sin\delta_0\Delta\delta_{PLL} \\ &\quad + \sin\delta_0\Delta v_y + v_{y0}\cos\delta_0\Delta\delta_{PLL} \\ \Delta v_q &= -\sin\delta_0\Delta v_x - v_{x0}\cos\delta_0\Delta\delta_{PLL} \\ &\quad + \cos\delta_0\Delta v_y - v_{y0}\sin\delta_0\Delta\delta_{PLL}\end{aligned} \tag{C.7}$$

$$\begin{aligned}\Delta i_x &= \cos\delta_0\Delta i_d - i_{d0}\sin\delta_0\Delta\delta_{PLL} \\ &\quad - \sin\delta_0\Delta i_q - i_{q0}\cos\delta_0\Delta\delta_{PLL} \\ \Delta i_y &= \sin\delta_0\Delta i_d + i_{d0}\cos\delta_0\Delta\delta_{PLL} \\ &\quad + \cos\delta_0\Delta i_q - i_{q0}\sin\delta_0\Delta\delta_{PLL}\end{aligned} \tag{C.8}$$

$$\begin{aligned}\Delta v_x &= Lp\Delta i_{Nx} + R\Delta i_{Nx} - \omega_0 L\Delta i_{Ny} \\ \Delta v_y &= Lp\Delta i_{Ny} + R\Delta i_{Ny} + \omega_0 L\Delta i_{Nx}\end{aligned} \tag{C.9}$$

$$\begin{aligned}\Delta i_x &= \Delta i_{Nx} + \Delta i_{sx} \\ \Delta i_y &= \Delta i_{Ny} + \Delta i_{sy}\end{aligned} \tag{C.10}$$

Similarly, the small-signal model shown in Equation B.14 can also be acquired for this single DG system. The matrices of the descriptor system model are as follows:

$$\mathbf{E} = \begin{bmatrix} \mathbf{E}_1 & \mathbf{E}_2 & \mathbf{E}_3 & \mathbf{E}_4 \\ \mathbf{E}_5 & \mathbf{E}_6 & \mathbf{E}_7 & \mathbf{E}_8 \\ \mathbf{E}_9 & \mathbf{E}_{10} & \mathbf{E}_{11} & \mathbf{E}_{12} \\ \mathbf{E}_{13} & \mathbf{E}_{14} & \mathbf{E}_{15} & \mathbf{E}_{16} \end{bmatrix}_{31\times 31} \tag{C.11}$$

$$\mathbf{E}_1 = \begin{bmatrix} 0 & 0 & 0 & 0 & -L & 0 & 0 & 0 \\ 0 & 0 & 0 & 0 & 0 & -L & 0 & 0 \\ 0 & 0 & 0 & 0 & 0 & 0 & 0 & 0 \\ 0 & 0 & 0 & 0 & 0 & 0 & 0 & 0 \\ 0 & 0 & 0 & 0 & 0 & 0 & 0 & 0 \\ 0 & 0 & 0 & 0 & 0 & 0 & 0 & 0 \\ 0 & 0 & 0 & 0 & 0 & 0 & 0 & 0 \\ 0 & 0 & 0 & 0 & 0 & 0 & 0 & 0 \end{bmatrix} \tag{C.12}$$

$$\mathbf{E}_2 = \begin{bmatrix} 0 & 0 & 0 & 0 & 0 & 0 & 0 & 0 \\ 0 & 0 & 0 & 0 & 0 & 0 & 0 & 0 \\ 0 & 0 & 0 & 0 & 0 & 0 & 0 & 0 \\ 0 & 0 & 0 & 0 & 0 & 0 & 0 & 0 \\ 0 & 0 & -1/\omega_0 & 0 & 0 & 0 & 0 & 0 \\ 0 & 0 & 0 & -1/\omega_0 & 0 & 0 & 0 & 0 \\ 0 & 0 & 0 & 0 & -1/\omega_0 & 0 & 0 & 0 \\ 0 & 0 & 0 & 0 & 0 & -1/\omega_0 & 0 & 0 \end{bmatrix} \tag{C.13}$$

$$\mathbf{E}_3 = [\mathbf{0}]_{8\times 8}, \mathbf{E}_4 = [\mathbf{0}]_{8\times 7}, \mathbf{E}_5 = [\mathbf{0}]_{8\times 8}, \mathbf{E}_7 = [\mathbf{0}]_{8\times 8}, \mathbf{E}_8 = [\mathbf{0}]_{8\times 7} \tag{C.14}$$

$$\mathbf{E}_6 = \begin{bmatrix} 0 & 0 & 0 & 0 & 0 & 0 & 0 & 0 \\ 0 & 0 & 0 & 0 & 0 & 0 & 0 & 0 \\ 0 & 0 & 0 & 0 & 0 & 0 & 0 & 0 \\ 0 & 0 & 0 & 0 & 0 & 0 & 0 & 0 \\ 0 & 0 & 0 & 0 & 0 & 0 & 0 & 0 \\ 0 & 0 & 0 & 0 & 0 & 0 & 1/\omega_0 & 0 \\ 0 & 0 & 0 & 0 & 0 & 0 & 0 & 0 \\ 0 & 0 & 0 & 0 & 0 & 0 & 0 & 0 \end{bmatrix} \tag{C.15}$$

$$\mathbf{E}_9 = [\mathbf{0}]_{8\times 8}, \mathbf{E}_{10} = [\mathbf{0}]_{8\times 8}, \mathbf{E}_{13} = [\mathbf{0}]_{7\times 8}, \mathbf{E}_{14} = [\mathbf{0}]_{7\times 8} \tag{C.16}$$

$$\mathbf{E}_{11} = \begin{bmatrix} 0 & 0 & 0 & 0 & 0 & 0 & 0 & 0 \\ 0 & 0 & 0 & 0 & 0 & 0 & 0 & 0 \\ 0 & 0 & L_s & 0 & 0 & 0 & 0 & 0 \\ 0 & 0 & 0 & L_s & 0 & 0 & 0 & 0 \\ 0 & 0 & k_{pi} & 0 & 1 & 0 & 0 & 0 \\ 0 & 0 & 0 & k_{pi} & 0 & 1 & 0 & 0 \\ 0 & 0 & 0 & 0 & 0 & 0 & 1 & 0 \\ 0 & 0 & 0 & 0 & 0 & 0 & 0 & 1 \end{bmatrix} \tag{C.17}$$

$$\mathbf{E}_{12} = \begin{bmatrix} 0 & 0 & 0 & 0 & 0 & 0 & 0 \\ 0 & 0 & 0 & 0 & 0 & 0 & 0 \\ 0 & 0 & 0 & 0 & 0 & 0 & 0 \\ 0 & 0 & 0 & 0 & 0 & 0 & 0 \\ -k_{pi} & 0 & 0 & 0 & 0 & 0 & 0 \\ 0 & -k_{pi} & 0 & 0 & 0 & 0 & 0 \\ 0 & 0 & k_{pp} & 0 & 0 & 0 & 0 \\ 0 & 0 & 0 & k_{pp} & 0 & 0 & 0 \end{bmatrix} \tag{C.18}$$

$$\mathbf{E}_{15} = \begin{bmatrix} 0 & 0 & 0 & 0 & 0 & 0 & 0 & 0 \\ 0 & -k_{p_{PLL}} & 0 & 0 & 0 & 0 & 0 & 0 \\ 0 & 0 & 0 & 0 & 0 & 0 & 0 & 0 \\ 0 & 0 & 0 & 0 & 0 & 0 & 0 & 0 \\ 0 & 0 & 0 & 0 & 0 & 0 & 0 & 0 \\ 0 & 0 & 0 & 0 & 0 & 0 & 0 & 0 \\ 0 & 0 & 0 & 0 & 0 & 0 & 0 & 0 \end{bmatrix} \tag{C.19}$$

$$\mathbf{E}_{16} = \begin{bmatrix} 0 & 0 & 0 & 0 & 0 & 1 & 0 \\ 0 & 0 & 0 & 0 & 1 & 0 & 0 \\ 0 & 0 & 0 & 0 & 0 & 0 & 0 \\ 0 & 0 & 0 & 0 & 0 & 0 & 0 \\ 0 & 0 & 0 & 0 & 0 & 0 & 0 \\ 0 & 0 & 0 & 0 & 0 & 0 & 0 \\ 0 & 0 & 0 & 0 & 0 & 0 & 0 \end{bmatrix} \tag{C.20}$$

$$\mathbf{A} = \begin{bmatrix} \mathbf{A}_1 & \mathbf{A}_2 & \mathbf{A}_3 & \mathbf{A}_4 \\ \mathbf{a}_5 & \mathbf{A}_6 & \mathbf{A}_7 & \mathbf{A}_8 \\ \mathbf{A}_9 & \mathbf{a}_{10} & \mathbf{A}_{11} & \mathbf{A}_{12} \\ \mathbf{A}_{13} & \mathbf{A}_{14} & \mathbf{A}_{15} & \mathbf{A}_{16} \end{bmatrix}_{31\times 31} \tag{C.21}$$

$$\mathbf{A}_1 = \begin{bmatrix} -1 & 0 & 0 & 0 & R & -X & 0 & 0 \\ 0 & -1 & 0 & 0 & X & R & 0 & 0 \\ 0 & 0 & 1 & 0 & -1 & 0 & -1 & 0 \\ 0 & 0 & 0 & 1 & 0 & -1 & 0 & -1 \\ -1 & 0 & 0 & 0 & 0 & 0 & R_1 & 0 \\ 0 & -1 & 0 & 0 & 0 & 0 & 0 & R_1 \\ 0 & 0 & 0 & 0 & 0 & 0 & 0 & 0 \\ 0 & 0 & 0 & 0 & 0 & 0 & 0 & 0 \end{bmatrix} \tag{C.22}$$

$$\mathbf{A}_2 = \begin{bmatrix} 0 & 0 & 0 & 0 & 0 & 0 & 0 & 0 \\ 0 & 0 & 0 & 0 & 0 & 0 & 0 & 0 \\ 0 & 0 & 0 & 0 & 0 & 0 & 0 & 0 \\ 0 & 0 & 0 & 0 & 0 & 0 & 0 & 0 \\ 0 & 0 & 0 & -1 & 0 & 0 & 0 & 0 \\ 0 & 0 & 1 & 0 & 0 & 0 & 0 & 0 \\ R_2 & 0 & 0 & 0 & 0 & -(\omega_0 - \omega_{r0})/\omega_0 & \psi_{ry0}/\omega_0 & 0 \\ 0 & R_2 & 0 & 0 & (\omega_0 - \omega_{r0})/\omega_0 & 0 & -\psi_{rx0}/\omega_0 & 0 \end{bmatrix} \tag{C.23}$$

$$\mathbf{A}_3 = \left[\mathbf{0}\right]_{8\times 8}, \mathbf{A}_4 = \left[\mathbf{0}\right]_{8\times 7} \tag{C.24}$$

$$\mathbf{A}_5 = \begin{bmatrix} 0 & 0 & 0 & 0 & 0 & 0 & X_m + X_s & 0 \\ 0 & 0 & 0 & 0 & 0 & 0 & 0 & X_m + X_s \\ 0 & 0 & 0 & 0 & 0 & 0 & X_m & 0 \\ 0 & 0 & 0 & 0 & 0 & 0 & 0 & X_m \\ 0 & 0 & 0 & 0 & 0 & 0 & -\psi_{y0} & \psi_{x0} \\ 0 & 0 & 0 & 0 & 0 & 0 & 0 & 0 \\ \cos\delta_0 & \sin\delta_0 & 0 & 0 & 0 & 0 & 0 & 0 \\ -\sin\delta_0 & \cos\delta_0 & 0 & 0 & 0 & 0 & 0 & 0 \end{bmatrix} \tag{C.25}$$

$$\mathbf{A}_6 = \begin{bmatrix} X_m & 0 & -1 & 0 & 0 & 0 & 0 & 0 \\ 0 & X_m & 0 & -1 & 0 & 0 & 0 & 0 \\ X_m + X_r & 0 & 0 & 0 & -1 & 0 & 0 & 0 \\ 0 & X_m + X_r & 0 & 0 & 0 & -1 & 0 & 0 \\ i_{sy0} & -i_{sx0} & 0 & 0 & 0 & 0 & 0 & -1 \\ 0 & 0 & 0 & 0 & 0 & 0 & 0 & 1/(2H) \\ 0 & 0 & 0 & 0 & 0 & 0 & 0 & 0 \\ 0 & 0 & 0 & 0 & 0 & 0 & 0 & 0 \end{bmatrix} \tag{C.26}$$

$$\mathbf{A}_7 = \begin{bmatrix} 0 & 0 & 0 & 0 & 0 & 0 & 0 & 0 \\ 0 & 0 & 0 & 0 & 0 & 0 & 0 & 0 \\ 0 & 0 & 0 & 0 & 0 & 0 & 0 & 0 \\ 0 & 0 & 0 & 0 & 0 & 0 & 0 & 0 \\ 0 & 0 & 0 & 0 & 0 & 0 & 0 & 0 \\ 0 & 0 & 0 & 0 & 0 & 0 & 0 & 0 \\ -1 & 0 & 0 & 0 & 0 & 0 & 0 & 0 \\ 0 & -1 & 0 & 0 & 0 & 0 & 0 & 0 \end{bmatrix} \tag{C.27}$$

$$\mathbf{A}_8 = \begin{bmatrix} 0 & 0 & 0 & 0 & 0 & 0 & 0 \\ 0 & 0 & 0 & 0 & 0 & 0 & 0 \\ 0 & 0 & 0 & 0 & 0 & 0 & 0 \\ 0 & 0 & 0 & 0 & 0 & 0 & 0 \\ 0 & 0 & 0 & 0 & 0 & 0 & 0 \\ 0 & 0 & 0 & 0 & 0 & 0 & 0 \\ 0 & 0 & 0 & 0 & 0 & \cos\delta_0 v_{y0} - \sin\delta_0 v_{x0} & 0 \\ 0 & 0 & 0 & 0 & 0 & -\cos\delta_0 v_{x0} - \sin\delta_0 v_{y0} & 0 \end{bmatrix} \tag{C.28}$$

$$\mathbf{A}_9 = \begin{bmatrix} 0 & 0 & -1 & 0 & 0 & 0 & 0 & 0 \\ 0 & 0 & 0 & -1 & 0 & 0 & 0 & 0 \\ 0 & 0 & 0 & 0 & 0 & 0 & 0 & 0 \\ 0 & 0 & 0 & 0 & 0 & 0 & 0 & 0 \\ 0 & 0 & 0 & 0 & 0 & 0 & 0 & 0 \\ 0 & 0 & 0 & 0 & 0 & 0 & 0 & 0 \\ 0 & 0 & 0 & 0 & 0 & 0 & 0 & 0 \\ 0 & 0 & 0 & 0 & 0 & 0 & 0 & 0 \end{bmatrix} \tag{C.29}$$

$$\mathbf{A}_{10} = [\mathbf{0}]_{8\times 7}, \mathbf{A}_{13} = [\mathbf{0}]_{7\times 8}, \mathbf{A}_{14} = [\mathbf{0}]_{7\times 8} \tag{C.30}$$

$$\mathbf{A}_{11} = \begin{bmatrix} 0 & 0 & \cos\delta_0 & -\sin\delta_0 & 0 & 0 & 0 & 0 \\ 0 & 0 & \sin\delta_0 & \cos\delta_0 & 0 & 0 & 0 & 0 \\ 0 & 0 & 0 & 0 & 1 & 0 & 0 & 0 \\ 0 & 0 & 0 & 0 & 0 & 1 & 0 & 0 \\ 0 & 0 & -k_{ii} & 0 & 0 & 0 & 0 & 0 \\ 0 & 0 & 0 & -k_{ii} & 0 & 0 & 0 & 0 \\ 0 & 0 & 0 & 0 & 0 & 0 & 0 & 0 \\ 0 & 0 & 0 & 0 & 0 & 0 & 0 & 0 \end{bmatrix} \tag{C.31}$$

$$\mathbf{A}_{12} = \begin{bmatrix} 0 & 0 & 0 & 0 & 0 & -\cos\delta_0 i_{q0} - \sin\delta_0 i_{d0} & 0 \\ 0 & 0 & 0 & 0 & 0 & \cos\delta_0 i_{d0} - \sin\delta_0 i_{q0} & 0 \\ 0 & 0 & 0 & 0 & 1 & 0 & 0 \\ 0 & 0 & 0 & 0 & 0 & 1 & 0 \\ k_{ii} & 0 & 0 & 0 & 0 & 0 & 0 \\ 0 & k_{ii} & 0 & 0 & 0 & 0 & 0 \\ 0 & 0 & -k_{ip} & 0 & 0 & 0 & 0 \\ 0 & 0 & 0 & -k_{ip} & 0 & 0 & 0 \end{bmatrix} \tag{C.32}$$

$$\mathbf{A}_{15} = \begin{bmatrix} 0 & 0 & 0 & 0 & 0 & 0 & 0 & 0 \\ 0 & k_{i_{PLL}} & 0 & 0 & 0 & 0 & 0 & 0 \\ i_{d0} & i_{q0} & v_{d0} & v_{q0} & 0 & 0 & 0 & 0 \\ i_{q0} & -i_{d0} & -v_{q0} & v_{d0} & 0 & 0 & 0 & 0 \\ 0 & 0 & 0 & 0 & 0 & 0 & \cos\theta_{f0} & -\sin\theta_{f0} \\ 0 & 0 & 0 & 0 & 0 & 0 & \sin\theta_{f0} & \cos\theta_{f0} \\ 0 & 0 & 0 & 0 & 0 & 0 & 0 & 0 \end{bmatrix} \tag{C.33}$$

$$\mathbf{A}_{16} = \begin{bmatrix} 0 & 0 & 0 & 0 & 1 & 0 & 0 \\ 0 & 0 & 0 & 0 & 0 & 0 & 0 \\ 0 & 0 & -1 & 0 & 0 & 0 & 0 \\ 0 & 0 & 0 & -1 & 0 & 0 & 0 \\ -1 & 0 & 0 & 0 & 0 & 0 & -i_{q0} \\ 0 & -1 & 0 & 0 & 0 & 0 & i_{d0} \\ 0 & 0 & 0 & 0 & \frac{\pi}{2}K_f & 0 & -1 \end{bmatrix} \tag{C.34}$$

B is the 31×3 matrix and all of its elements are zero except for:

$$
\begin{aligned}
B_{(14,3)} &= -1/(2H) \\
B_{(23,1)} &= k_{ip} \\
B_{(24,2)} &= k_{ip}
\end{aligned}
\tag{C.35}
$$

The state variable vector of the new model are

$$
\begin{aligned}
\Delta\mathbf{x} = [&\Delta v_x \Delta v_y \Delta i_x \Delta i_y \Delta i_{Nx} \Delta i_{Ny} \Delta i_{sx} \Delta i_{sy} \Delta i_{rx} \Delta i_{ry} \\
&\Delta\psi_{sx} \Delta\psi_{sy} \Delta\psi_{rx} \Delta\psi_{ry} \Delta\omega_r \Delta T_e \Delta v_d \Delta v_q \Delta i_d \Delta i_q \Delta u_d \Delta u_q \\
&\Delta i_{dref} \Delta i_{qref} \Delta i^*_{dref} \Delta i^*_{qref} \Delta P \Delta Q \Delta\omega_{PLL} \Delta\delta_{PLL} \Delta\theta_f]^T
\end{aligned}
\tag{C.36}
$$

And the input vector is:

$$
\Delta\mathbf{u} = [\Delta P_{ref} \Delta Q_{ref} \Delta T_m]^T \tag{C.37}
$$

The equivalent steady-state circuit of the single DG system with motor load is shown in Figure C.1 where s_0 is the steady-state slip of the motor load:

$$
s_0 = \frac{\omega_0 - \omega_{r0}}{\omega_0} \tag{C.38}
$$

The power flow from the DG to the network and load is:

$$
P_{ref} + jQ_{ref} = (v_{x0} + jv_{y0})(i_{x0} - ji_{y0}) \tag{C.39}
$$

where $i_{x0} + ji_{y0}$ is the steady-state inverter current and

$$
\begin{aligned}
v_{x0} &= V_0 \cos\delta_0 \\
v_{y0} &= V_0 \sin\delta_0
\end{aligned}
\tag{C.40}
$$

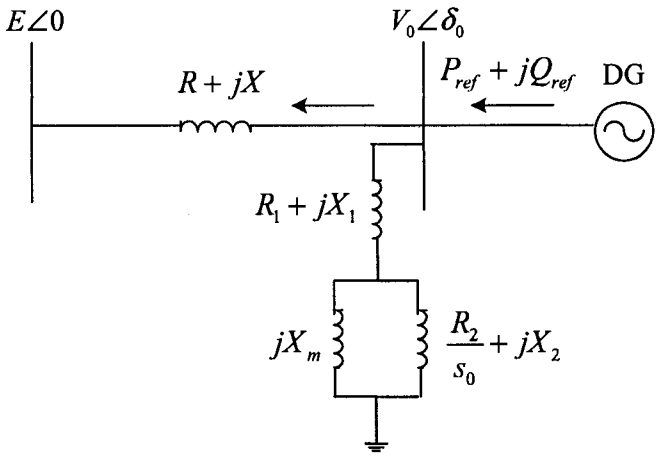

Figure C.1: Equivalent steady-state circuit of the single DG system with motor load

$$\begin{aligned} v_{x0} &= Ri_{Nx0} - Xi_{Ny0} + E \\ v_{y0} &= Ri_{Ny0} + Xi_{Nx0} \end{aligned} \tag{C.41}$$

$$\begin{aligned} i_{x0} &= i_{Nx0} + i_{sx0} \\ i_{y0} &= i_{Ny0} + i_{sy0} \end{aligned} \tag{C.42}$$

The steady-state inverter equations are the same with those in the single DG system with *RLC* load. The interface between the inverter and the network is given below:

$$\begin{bmatrix} v_{d0} \\ v_{q0} \end{bmatrix} = \begin{bmatrix} \cos\delta_0 & \sin\delta_0 \\ -\sin\delta_0 & \cos\delta_0 \end{bmatrix} \begin{bmatrix} v_{x0} \\ v_{y0} \end{bmatrix} \tag{C.43}$$

$$\begin{bmatrix} i_{d0} \\ i_{q0} \end{bmatrix} = \begin{bmatrix} \cos\delta_0 & \sin\delta_0 \\ -\sin\delta_0 & \cos\delta_0 \end{bmatrix} \begin{bmatrix} i_{x0} \\ i_{y0} \end{bmatrix} \tag{C.44}$$

The steady-state calculations for the motor are as follows:

$$
\begin{aligned}
v_{x0} &= R_s i_{sx0} - \psi_{sy0} \\
v_{y0} &= R_s i_{sy0} + \psi_{sx0} \\
0 &= R_r i_{rx0} - s_0 \psi_{ry0} \\
0 &= R_r i_{ry0} + s_0 \psi_{rx0}
\end{aligned}
\tag{C.45}
$$

$$
\begin{aligned}
\psi_{sx0} &= (X_m + X_1) i_{sx0} + X_m i_{rx0} \\
\psi_{sy0} &= (X_m + X_1) i_{sy0} + X_m i_{ry0} \\
\psi_{rx0} &= (X_m + X_2) i_{rx0} + X_m i_{sx0} \\
\psi_{ry0} &= (X_m + X_2) i_{ry0} + X_m i_{sy0}
\end{aligned}
\tag{C.46}
$$

$$
T_{e0} = T_m = \psi_{sx0} i_{sy0} - \psi_{sy0} i_{sx0} \tag{C.47}
$$

Appendix D

Small-Signal Model of Multi-DG System

The small-signal model of multi-DG system is expressed as follows:

$$\begin{aligned} p\Delta\mathbf{u}_d &= \mathbf{k}_{pi}p(\Delta\mathbf{i}^*_{dref} - \Delta\mathbf{i}_d) + \mathbf{k}_{ii}(\Delta\mathbf{i}^*_{dref} - \Delta\mathbf{i}_d) \\ p\Delta\mathbf{u}_q &= \mathbf{k}_{pi}p(\Delta\mathbf{i}^*_{qref} - \Delta\mathbf{i}_q) + \mathbf{k}_{ii}(\Delta\mathbf{i}^*_{qref} - \Delta\mathbf{i}_q) \end{aligned} \tag{D.1}$$

$$\begin{aligned} \Delta\mathbf{u}_d &= \mathbf{L}_s p\Delta\mathbf{i}_d \\ \Delta\mathbf{u}_q &= \mathbf{L}_s p\Delta\mathbf{i}_q \end{aligned} \tag{D.2}$$

$$\begin{aligned} p\Delta\mathbf{i}_{dref} &= -\mathbf{k}_{pp}p\Delta\mathbf{P} - \mathbf{k}_{ip}\Delta\mathbf{P} + \mathbf{k}_{ip}\Delta\mathbf{P}_{ref} \\ p\Delta\mathbf{i}_{qref} &= -\mathbf{k}_{pp}p\Delta\mathbf{Q} - \mathbf{k}_{ip}\Delta\mathbf{Q} + \mathbf{k}_{ip}\Delta\mathbf{Q}_{ref} \end{aligned} \tag{D.3}$$

$$\begin{aligned} \Delta\mathbf{P} &= \mathbf{v}_{d0}\Delta\mathbf{i}_d + \mathbf{i}_{d0}\Delta\mathbf{v}_d + \mathbf{v}_{q0}\Delta\mathbf{i}_q + \mathbf{i}_{q0}\Delta\mathbf{v}_q \\ \Delta\mathbf{Q} &= \mathbf{v}_{d0}\Delta\mathbf{i}_q + \mathbf{i}_{q0}\Delta\mathbf{v}_d - \mathbf{v}_{q0}\Delta\mathbf{i}_d - \mathbf{i}_{d0}\Delta\mathbf{v}_q \end{aligned} \tag{D.4}$$

$$p\Delta\boldsymbol{\delta}_{PLL} = \Delta\boldsymbol{\omega}_{PLL} \tag{D.5}$$

$$p\Delta\boldsymbol{\omega}_{PLL} = \mathbf{k}_{p_{PLL}}p\Delta\mathbf{v}_q + \mathbf{k}_{i_{PLL}}\Delta\mathbf{v}_q \tag{D.6}$$

$$\Delta\boldsymbol{\theta}_f = \frac{\pi}{2}\mathbf{K}_f\Delta\boldsymbol{\omega}_{PLL} \tag{D.7}$$

$$\begin{aligned}\Delta \mathbf{i}^{*}_{dref} &= \cos\boldsymbol{\theta}_{\boldsymbol{f0}}\Delta \mathbf{i}_{dref} - \sin\boldsymbol{\theta}_{\boldsymbol{f0}}\Delta \mathbf{i}_{qref} - \mathbf{i}_{q0}\Delta\boldsymbol{\theta}_{\boldsymbol{f}} \\ \Delta \mathbf{i}^{*}_{qref} &= \sin\boldsymbol{\theta}_{\boldsymbol{f0}}\Delta \mathbf{i}_{dref} + \cos\boldsymbol{\theta}_{\boldsymbol{f0}}\Delta \mathbf{i}_{qref} + \mathbf{i}_{d0}\Delta\boldsymbol{\theta}_{\boldsymbol{f}}\end{aligned} \tag{D.8}$$

where the variables in the model are vectors and each vector is composed of n elements which are related to the variables of the single DG model. For example, the voltage vectors $\Delta\mathbf{u}_d$ and $\Delta\mathbf{u}_q$ have the following definitions:

$$\begin{aligned}\Delta\mathbf{u}_d &= [\Delta u_{d1}, \Delta u_{d2}, ..., \Delta u_{dn}]^T \\ \Delta\mathbf{u}_q &= [\Delta u_{q1}, \Delta u_{q2}, ..., \Delta u_{qn}]^T\end{aligned} \tag{D.9}$$

And the diagonal matrices $\mathbf{v}_{d0}$, $\mathbf{v}_{q0}$, $\mathbf{i}_{d0}$, $\mathbf{i}_{q0}$, $\cos\boldsymbol{\theta}_{\boldsymbol{f0}}$, $\sin\boldsymbol{\theta}_{\boldsymbol{f0}}$, $\mathbf{k}_{pi}$, $\mathbf{k}_{ii}$, $\mathbf{k}_{pp}$, $\mathbf{k}_{ip}$, $\mathbf{k}_{i_{PLL}}$, $\mathbf{k}_{p_{PLL}}$, $\mathbf{L}_s$ and $\mathbf{K}$ have the following definitions: $\mathbf{v}_{d0} = \text{diag}\{v_{d0j}\}$, $\mathbf{v}_{q0} = \text{diag}\{v_{q0j}\}$, $\mathbf{i}_{d0} = \text{diag}\{i_{d0j}\}$, $\mathbf{i}_{q0} = \text{diag}\{i_{q0j}\}$, $\cos\boldsymbol{\theta}_{\boldsymbol{f0}} = \text{diag}\{\cos\theta_{f0j}\}$, $\sin\boldsymbol{\theta}_{\boldsymbol{f0}} = \text{diag}\{\sin\theta_{f0j}\}$, $\mathbf{k}_{pi} = \text{diag}\{k_{pij}\}$, $\mathbf{k}_{ii} = \text{diag}\{k_{iij}\}$, $\mathbf{k}_{pp} = \text{diag}\{k_{ppj}\}$, $\mathbf{k}_{ip} = \text{diag}\{k_{ipj}\}$, $\mathbf{k}_{p_{PLL}} = \text{diag}\{k_{pPLLj}\}$, $\mathbf{k}_{i_{PLL}} = \text{diag}\{k_{iPLLj}\}$, $\mathbf{L}_s = \text{diag}\{L_{sj}\}$ and $\mathbf{K} = \text{diag}\{K_j\}$ with $j = 1, 2, ..., n$.

The small-signal model equations of the network and loads are expressed in the common reference frame (xy frame) and can be written as:

$$\begin{bmatrix}\Delta\mathbf{i}_x \\ \Delta\mathbf{i}_y\end{bmatrix} = \begin{bmatrix}\mathbf{G} & -\mathbf{B} \\ \mathbf{B} & \mathbf{G}\end{bmatrix}\begin{bmatrix}\Delta\mathbf{v}_x \\ \Delta\mathbf{v}_y\end{bmatrix} \tag{D.10}$$

where

$$\begin{aligned}\Delta\mathbf{v}_x &= [\Delta v_{x1}, \Delta v_{x2}, ..., \Delta v_{xn}]^T \\ \Delta\mathbf{v}_y &= [\Delta v_{y1}, \Delta v_{y2}, ..., \Delta v_{yn}]^T \\ \Delta\mathbf{i}_x &= [\Delta i_{x1}, \Delta i_{x2}, ..., \Delta i_{xn}]^T \\ \Delta\mathbf{i}_y &= [\Delta i_{y1}, \Delta i_{y2}, ..., \Delta i_{yn}]^T\end{aligned} \tag{D.11}$$

In the model the DG loads are constant impedance loads and the matrices **G** and **B** are acquired from the network system admittance matrix. In Equation (D.11) the dynamics of the network and the loads are not included in order to simply the multi-DG system model. If the dynamics are considered the network and the loads equations will be represented by linearized differential equations. The impact of the network and the loads dynamics on the accuracy of the small-signal model will be analyzed in the model validation section. The DGs have the connections with the network and the loads at the inverter terminals. The inverter terminal voltages and the inverter output currents are the bridges of the interface. The interface equations transform the voltages and the currents of each individual inverter from its own *dq* reference frame to the network common *xy* reference frame. The transformation is defined in Equation (3.58) and Equation (3.59). The linearization of the interface equations can be written as:

$$\begin{aligned}
\Delta \mathbf{v}_d &= \mathbf{C}_0 \Delta \boldsymbol{v}_x + \mathbf{S}_0 \Delta \boldsymbol{v}_y + (\mathbf{C}_0 \Delta \boldsymbol{v}_{y0} - \mathbf{S}_0 \Delta \boldsymbol{v}_{x0}) \Delta \boldsymbol{\delta}_{PLL0} \\
\Delta \mathbf{v}_q &= -\mathbf{S}_0 \Delta \boldsymbol{v}_x + \mathbf{C}_0 \Delta \boldsymbol{v}_y - (\mathbf{C}_0 \Delta \boldsymbol{v}_{x0} + \mathbf{S}_0 \Delta \boldsymbol{v}_{y0}) \Delta \boldsymbol{\delta}_{PLL0} \\
\Delta \mathbf{i}_x &= \mathbf{C}_0 \Delta \boldsymbol{i}_d - \mathbf{S}_0 \Delta \boldsymbol{i}_q - (\mathbf{C}_0 \Delta \boldsymbol{i}_{q0} + \mathbf{S}_0 \Delta \boldsymbol{i}_{d0}) \Delta \boldsymbol{\delta}_{PLL0} \\
\Delta \mathbf{i}_y &= \mathbf{S}_0 \Delta \boldsymbol{i}_d + \mathbf{C}_0 \Delta \boldsymbol{i}_q + (\mathbf{C}_0 \Delta \boldsymbol{i}_{d0} - \mathbf{S}_0 \Delta \boldsymbol{i}_{q0}) \Delta \boldsymbol{\delta}_{PLL0}
\end{aligned} \tag{D.12}$$

where the diagonal matrices $\mathbf{C}_0$ and $\mathbf{S}_0$ are defined as $\mathbf{C}_0 = \text{diag}\{\cos \delta_{PLL0j}\}$ and $\mathbf{S}_0 = \text{diag}\{\sin \delta_{PLL0j}\}$ with $j = 1, 2, ..., n$.

The DG model equations, the network and the loads equation and the interface equations are connected to get the complete model for a multiple inverter-based DG system, where each one is equipped with the SFS anti-islanding method. With constant DG power reference inputs the descriptor system form of the model is as follows:

$$\mathbf{H}p\Delta\mathbf{x} = \mathbf{A}\Delta\mathbf{x} \tag{D.13}$$

where

$$\Delta\mathbf{x} = [\Delta\boldsymbol{\delta}_{PLL}\Delta\boldsymbol{\omega}_{PLL}\Delta\mathbf{i}_d\Delta\mathbf{i}_q\Delta\mathbf{i}_{dref}\Delta\mathbf{i}_{qref}\Delta\mathbf{u}_d\Delta\mathbf{u}_q\Delta\mathbf{P}\Delta\mathbf{Q} \\ \Delta\boldsymbol{\theta}_f\Delta\mathbf{i}^*_{dref}\Delta\mathbf{i}^*_{qref}\Delta\mathbf{v}_d\Delta\mathbf{v}_q\Delta\mathbf{i}_x\Delta\mathbf{i}_y\Delta\mathbf{v}_x\Delta\mathbf{v}_y]^T \quad \text{(D.14)}$$

Equation (D.13) contains derivative equations as well as algebraic equations. As a result, the matrix $\mathbf{H}$ is singular. Due to the sparsity of the system admittance matrix, the matrices $\mathbf{A}$ and $\mathbf{H}$ are sparse matrices. The classical state-space model of the system can be further derived from Equation (D.13). The state-space model has the following form:

$$p\Delta\widetilde{\mathbf{x}} = \mathbf{M}\Delta\widetilde{\mathbf{x}} \quad \text{(D.15)}$$

where

$$\mathbf{M} = (\mathbf{H}_1 - \mathbf{H}_2\mathbf{A}_4^{-1}\mathbf{A}_3)^{-1}(\mathbf{A}_1 - \mathbf{A}_2\mathbf{A}_4^{-1}\mathbf{A}_3) \quad \text{(D.16)}$$

$$\Delta\widetilde{\mathbf{x}} = [\Delta\boldsymbol{\delta}_{PLL}\Delta\boldsymbol{\omega}_{PLL}\Delta\mathbf{i}_d\Delta\mathbf{i}_q\Delta\mathbf{i}_{dref}\Delta\mathbf{i}_{qref}\Delta\mathbf{u}_d\Delta\mathbf{u}_q]^T \quad \text{(D.17)}$$

$$\mathbf{H} = \begin{bmatrix} \mathbf{H}_1 & \mathbf{H}_2 \\ \mathbf{0} & \mathbf{0} \end{bmatrix} \quad \text{(D.18)}$$

$$\mathbf{A} = \begin{bmatrix} \mathbf{A}_1 & \mathbf{A}_2 \\ \mathbf{A}_3 & \mathbf{A}_4 \end{bmatrix} \quad \text{(D.19)}$$

Appendix E

DG System Data and Parameter Settings

The system data and parameter settings of the studied DG systems are listed in this appendix.

Table E.1: System Data and Parameter Settings for The Single DG System with Parallel *RLC* Load

Parameter	Value	Parameter	Value
V_{base}	$120\sqrt{2}$ (V)	$k_{p_{PLL}}$	50
S_{base}	10000 (W)	$k_{i_{PLL}}$	500
R	0.2 (Ω)	P_{ref}	0.1 ($p.u.$)
X	0.3 (Ω)	Q_{ref}	0 ($p.u.$)
L_s	1 (mH)	K_f	0.01
k_{pp}	0.5	c_{f0}	0.05
k_{ip}	100	R_L	4.32 (Ω)
k_{pi}	0.5	L_L	6.3664 (mH)
k_{ii}	500	C_L	1.1052 (mF)

Table E.2: System Data and Parameter Settings for The Single DG System with Motor Load

Parameter	Value	Parameter	Value
V_{base}	$277\sqrt{2}$ (V)	Q_{ref}	0 $(p.u.)$
S_{base}	10000 (W)	K_f	0.01
R	0.012 (Ω)	c_{f0}	0.02
X	0.1152(Ω)	S_m	50 (HP)
L_s	1 (mH)	R_1	0.09961 (Ω)
k_{pp}	2	X_1	0.3269 (Ω)
k_{ip}	100	R_2	0.05837 (Ω)
k_{pi}	2	X_2	0.3269 (Ω)
k_{ii}	500	X_m	11.4568 (Ω)
$k_{p_{PLL}}$	50	H	0.0711 (s)
$k_{i_{PLL}}$	500	T_m	197.8826 $(N.m)$
P_{ref}	0.2 $(p.u.)$	Pairs of Poles	2

Table E.3: System Data and Parameter Settings for The Canadian Benchmark Distribution System with Multiple DG Units

Parameter	Value	Parameter	Value
S_{base}	10 (MW)	k_{ppj}	2.5
V_{base1}	$120\sqrt{2}/\sqrt{3}$ (kV)	k_{ipj}	100
V_{base2}	$12.5\sqrt{2}/\sqrt{3}$ (kV)	k_{pij}	2.5
V_{base3}	$208\sqrt{2}/\sqrt{3}$ (V)	k_{iij}	500
R_s	0 $(p.u.)$	L_{sj}	1 (mH)
X_s	0.01 $(p.u.)$	$k_{p_{PLLj}}$	50
R_T	0 $(p.u.)$	$k_{i_{PLLj}}$	500
X_T	0.1 $(p.u.)$	K_{fj}	0.01
R_f	0.0029 $(p.u.)$	c_{f0j}	0
X_f	0.0041 $(p.u.)$	P_{refj}	0.1 $(p.u.)$
R_t	0 $(p.u.)$	Q_{refj}	0 $(p.u.)$
X_t	0.2 $(p.u.)$	$(j=1,2,3,4)$	